2019

INVESTIGATION OF LIGHT TRANSPORT AND SCATTERING IN TURBULENT CLOUDS: SIMULATIONS AND LABORATORY MEASUREMENTS

Corey D. Packard
Michigan Technological University, cdpackar@mtu.edu

Recommended Citation
Packard, Corey D., "INVESTIGATION OF LIGHT TRANSPORT AND SCATTERING IN TURBULENT CLOUDS: SIMULATIONS AND LABORATORY MEASUREMENTS", Open Access Dissertation, Michigan Technological University, 2019.
https://doi.org/10.37099/mtu.dc.etdr/959

INVESTIGATION OF LIGHT TRANSPORT AND SCATTERING IN TURBULENT CLOUDS: SIMULATIONS AND LABORATORY MEASUREMENTS

By

Corey D. Packard

A DISSERTATION

Submitted in partial fulfillment of the requirements for the degree of

DOCTOR OF PHILOSOPHY

In Atmospheric Sciences

MICHIGAN TECHNOLOGICAL UNIVERSITY

2019

This dissertation has been approved in partial fulfillment of the requirements for the Degree of DOCTOR OF PHILOSOPHY in Atmospheric Sciences.

Department of Physics

Dissertation Advisor: *Dr. Raymond A. Shaw*

Committee Member: *Dr. Jeremy P. Bos*
Committee Member: *Dr. John Valenzuela*
Committee Member: *Dr. Michael L. Larsen*
Department Chair: *Dr. Ravindra Pandey*

Dedication

To my family…

My wife – Tara

My sons – Elijah, Jadon and Silas

Table of Contents

List of figures

List of tables

Preface

Topics covered in this thesis are derived from the research I have done as a graduate student in the Atmospheric Sciences program (Pi chamber group) in the Department of Physics at Michigan Technological University. In chapter 1, an overview of the topic and some background information relevant to this dissertation is provided. Chapter 2 discusses the measurement of optical blurring in a turbulent laboratory cloud chamber. It is based on an article (Packard et al., 2018) published in the Journal of Applied Remote Sensing. Chapter 3 describes a Monte Carlo Ray Tracing code I created (*mcScatter*) to explore a variety of atmospheric particle fields via scattering simulation. Chapter 4 presents the results of these scattering simulations used to investigate the impact of particle (spatial) clustering on depth-dependent radiative transfer and the role of the radial distribution function. It is based on an article (Packard et al., 2019) published in the Journal of Quantitative Spectroscopy and Radiative Transfer. Chapter 5 is the extension of work presented in Chapter 4, and is based on a manuscript under preparation for submission in a peer-reviewed journal. It uses Large Eddy Simulations to generate laboratory-realistic spatially correlated atmospheric particle fields which are explored with scattering simulations. These numerical simulations suggest a laboratory cloud chamber experiment that could be conducted to measure the presence (and perhaps the severity) of particle clustering. Chapter 6 is the final chapter which briefly summarizes the major findings, discusses some implications and outlines intriguing lines of future scientific inquiry related to the studies presented in this thesis.

For the research presented in the above articles, experiments, theoretical derivation, data analysis, and writing were done by me with the help of Dr. Raymond A. Shaw and co-authors. The Large Eddy Simulations were performed by Mr. Subin Thomas, who will be a co-author of the manuscript in preparation for submission (e.g., chapter 5). We are thankful to all co-authors for their contributions in the listed publications.

Acknowledgements

Dost thou know the balancings of the clouds, the wondrous works of him which is perfect in knowledge? − Job 37:16 (KJV)

…yet you do not know what tomorrow will bring. What is your life? For you are a mist that appears for a little time and then vanishes. − James 4:14 (ESV)

I have set my rainbow in the clouds, and it will be the sign of the covenant between me and the earth. − Genesis 9:13 (NIV)

I would first like to thank my loving wife, Tara, for enduring several years where a substantial portion of my energy and attention was focused on this doctoral journey. Her support during my academic quest was crucial to my success, and she sacrificed much during this time for me – more than I deserved. I also want to thank her for never being impressed by me, which was motivating and encouraged humility.

Next, I would like to thank my three sons, Elijah, Jadon, and Silas for their patience over the last few years. For a significant portion of their childhood they had a very busy father, and I greatly appreciate the understanding they displayed. They are lucky to have such an amazing mother who helped in so many ways when I was occupied with studying.

I would also like to thank my parents, both of whom were teachers, for imparting the value of education and hard work. I grew up with a love for reading and learning, and they are at least partially to blame. They have always encouraged me in my pursuits, and growing up believing that anything is possible is no small gift.

I would like to thank my immeasurably wise advisor, Dr. Raymond Shaw, for taking me on as a part-time student and guiding my academic efforts. This dissertation, the publications on which it is based, the completion of the Atmospheric Science program, and the rewarding accomplishment of fulfilling my lifelong dream to continue learning as long as possible – none of this would have been possible without him. As an advisor, his role model was immensely impactful. His assistance in matters great and small, his friendly and steady demeanor no matter the circumstances, and his demand for excellence balanced with fairness – I hope these traits will become hallmarks of my style as well. From chalkboard drawings of skiers traversing a dense forest to explain the mean-free-path concept, to cheering with (and against) him at our sons' soccer games – he has left an indelible mark on me, and it is one I will always cherish.

I am so very grateful to my committee members Dr. Jeremy Bos, Dr. John Valenzuela, Dr. Michael Larsen, and Dr. Michael Roggemann. Each of them guided me in different stages and aspects of my research. Without their support and willingness to participate in countless research discussions, paper reviews, and teleconferences (during hurricane season!) in spite of their busy teaching and travel schedules, this would not have been possible. I also wish to express appreciation for provocative discussions with Dr. Will Cantrell and Dr. Alex Kostinski – thank you for your contributions and encouragement.

During my time at Michigan Tech, I was fortunate to be surrounded by many bright researchers in the Atmospheric Science Program and Physics department. I'd like to thank Dr. Neel Uday Desai, with whom I spent countless hours studying for the doctoral entrance exams. In spite of our shared stress, there was something enjoyable about all those winter evenings in Fisher, enjoying cookie and tea breaks during our whiteboard intermissions. I miss our time together, minus the exams. I'd also like to thank Dr. Kamal Kant Chandrakar, both for time-saving software for processing particle size distribution data from the cloud chamber and his positive attitude and warm smile during a busy period of life.

To my employer, ThermoAnalytics, I will always appreciate your financial and moral support during this crazy time. Thank you for believing in scholarship, continuing education, and for believing in me.

In regards to chapter 2, I want to thank David Ciochetto for his assistance with initial exploratory measurements in the cloud chamber, Douglas Banyai at ThermoAnalytics, Inc. for his insightful feedback during several productive late-night physics discussions, and Matt Monte (of Monte Consulting) for the loan of photographic supplies and related technical lighting suggestions. Regarding chapters 3 and 4, I would like to thank Benjamin Bandt-Horn, Eric Marttila and James Truax (all from ThermoAnalytics, Inc.) for their tremendously helpful suggestions regarding the practical implementation of current computer graphics methodologies for efficient ray tracing. Much time was saved with their guidance. Additionally, my co-authors and I are grateful to Craig Bohren, Eugene Clothiaux, and Peter Pilewskie for helpful conversations about Monte Carlo versus 2-stream results.

This material is based on research partially sponsored by Air Force Research Laboratory (AFRL) under agreement number FA9453-16-1-0083, as well as National Science Foundation (NSF) grants AGS-1532977, AGS-1823334, and AGS-1754244. The U.S. Government is authorized to reproduce and distribute reprints for Governmental purposes notwithstanding any copyright notation thereon. The views and conclusions contained herein are those of the authors and should not be interpreted as necessarily representing the official policies or endorsements, either expressed or implied, of Air Force Research Laboratory (AFRL) or the U.S. Government.

List of abbreviations

CCN	Cloud Condensation Nuclei
CDF	Cumulative Density Function
DNS	Direct Numerical Simulation
EO	Electro-optic
ETD	Early-Time Diffusion
FOV	Field of View
FSO	Free-Space Optical
HG	Henyey-Greenstein
ISC	Independently Scattering Cloudlet
LES	Large Eddy Simulation
LTD	Late-Time Diffusion
MCRT	Monte Carlo Ray Tracing
MTF	Modulation Transfer Function
PCF	Pair Correlation Function
PDF	Probability Density Function
PSF	Point Spread Function
RDF	Radial Distribution Function
RTE	Radiative Transfer Equation

Abstract

A better understanding of light transport and scattering in turbulent clouds is needed for more accurate remote sensing, improved imaging and signal transmission through atmospheric aerosol and fog, and deeper understanding of cloud optical properties relevant to weather and climate. In this study, we investigate the impact of light scattering in clouds on two problems of atmospheric relevance.

In the first part, we examine deleterious effects of the atmosphere on remotely acquired images including signal attenuation and potential blurring due to forward-scattered light accepted by the imaging system. A prior proposed aerosol scattering model provides a method for calculating the contrast and spatial detail expected when imaging through atmospheres with significant aerosol optical depth. We compare modulation transfer functions obtained directly from images taken through a cloud chamber to those calculated from theory using measured cloud properties. We find that the significance of scattering-induced optical blurring depends sensitively on the properties of both the particles and the imaging system. The theoretical aerosol expression modulation transfer function capture the basic behavior of the system, with deviations likely a result of not accounting for broad particle size distributions.

In the second part, we investigate how clusters and voids in the spatial distributions of particles within a cloud cause light transport to deviate from the exponential extinction law. We explore both perfectly random and correlated scattering media with a Monte Carlo ray tracing program, and find that the degree of non-exponential attenuation can be characterized by the radial distribution function. Our numerical observations regarding direct, diffuse and backward radiative transfer are shown to be consistent with a previous "cloudlet" approach, providing a bridge between the analytical cloudlet model and continuous correlation function approaches. Finally, we numerically explore light propagation through turbulent clouds with polydisperse size distributions calculated by a large eddy simulation of the MTU Pi Chamber. We find that both the mean and standard deviation of direct and diffuse forward flux change when clustering exists, and make suggestions for future laboratory cloud chamber experiments to detect the presence of spatial correlation.

1 Introduction

1.1 A brief overview of our investigations into light scattering due to cloud aerosols

The propagation of electromagnetic radiation through the atmosphere is an important phenomenology to understand comprehensively. We live in an age where remote sensors abound and are fielded for numerous purposes, and their performance is governed by radiative transfer through the absorbing, refracting and scattering medium of the atmosphere. A thorough and detailed understanding of the manner in which radiation traverses a particle-laden medium such as an aerosol-filled cloud enables the prediction of (and potentially improvement of) remote sensing performance. In the chapters that follow, we study the impact of atmospheric clouds on light propagation from several perspectives.

In this work we examine, from several vantage points, how light traverses a strongly forward-scattering medium (i.e., a medium containing particles large compared to the optical wavelength). We look at the small-angle scattering of visible light as it passes through a cloud distribution, and how this scattering increases the optical blurring present in images captured by remote sensors located on the opposite (non-illuminated) side of expansion clouds generated in a laboratory cloud chamber. We use Monte Carlo scattering simulations to explore the impact of particle clustering on direct and diffuse (forward and backward) irradiance at various depths in virtual cloud distributions. We determine the ability of the radial distribution function to describe which parameters of a spatially-correlated particle distribution impact depth-dependent fluxes. Taking this a step further, we then use the Monte Carlo code to explore an experimental setup where the presence or absence of particle clustering could be sensed (and possibly measured). These investigations constitute our multi-faceted look into the phenomenology of light scattering due to cloud aerosols and the impact this scattering has on remote sensing applications.

1.2 Optical blurring due to small-angle forward scattering

An imaging system functions by focusing the radiation that passes through its optical system onto a detector which resolves the scene of interest. In an ideal scenario with perfect optics and a uniform medium between the image source and the imaging system, the ability to record a clear, sharp image is governed by the optical characteristics of the imaging system (e.g., aperture size, pixel dimensions). Deviations from these ideal conditions, referred to as optical aberrations, are often caused by imperfections in the physical components of the optical system due to manufacturing tolerances and other real-world constraints.

Additionally, the presence of a turbulent aerosol-laden atmosphere degrades sensor performance. Deleterious effects of the atmosphere on remotely acquired images includes absorption and scattering of light by aerosol particulates, which not only attenuates the signal but can cause blurring due to forward-scattered light accepted by the imaging system. Whether the subsequent image degradation is likely to be minor or significant, depending on the scenario and application, can only be determined with accurate models of the entire optical system. These detailed optical system models must consider both the remote sensor itself and the atmosphere in which it operates. Attempts have been made by the atmospheric and optical communities to develop these models analytically, to ensure a sound physical foundation, and then test them experimentally to verify their accuracy. Proposed aerosol scattering models, if sound, provide a method for simulating the contrast and spatial detail expected when imaging through atmospheres with significant aerosol optical depth.

In the late 1970s, Lutomirski suggested (Lutomirski, 1978) using a modulation transfer function to model atmospheric degradation of an electro-optical (EO) imaging system, and Ishimaru proposed (Ishimaru, 1997, 1978) a modulation transfer function meant to include the scattering effects of a random medium. This aerosol MTF showed dependency on dominant particle size, among other factors. Soon after, in the 1980s, Kopeika and collaborators demonstrated via atmospheric experiments (Kopeika, 1987, 1985, 1982; Kopeika et al., 1981) that spatial frequency-dependent contrast reduction depends on particle concentration and size parameter. Contemporaneous laboratory experiments, such as those performed by Kuga and Ishimaru (Kuga and Ishimaru, 1985) and also Volnistova and Drofa (Volnistova and Drofa, 1986), resulted in similar findings. Several attempts (Ishimaru, 1978; Lutomirski, 1978; Zardecki et al., 1986, 1984) were made to model this spatial frequency-dependent phenomenon with analytic aerosol modulation transfer functions using the small-angle approximation.

Bissonnette (Bissonnette, 1992) pointed out that these proposed aerosol MTF expressions assume constant radiant intensity; photons reaching the aperture are not depleted by scattering, as the photons scattered away from the imaging sensor are assumed to be exactly replaced by photons scattered toward it. This supposition limits the validity of these proposed expressions. In response, Bissonnette proposed a method for calculating an aerosol MTF valid for size parameters of order one or greater (Bissonnette, 1992) which used a propagation model to approximate the radiative transfer equation and used a diffusion process for flux normal to the optical axis. He found that the cutoff frequency of the aerosol MTF depends strongly on particle radius, shifting toward higher frequencies with increasing size. Bissonnette also found the cutoff frequency to be almost independent of optical depth. Both of these results were found to be in agreement with the principal features of Kuga and Ishimaru's MTF data, and were also favorably compared with Bissonnette's atmospheric experimentation results in fog and rain. Discrepancies were stated to be due to transient and range-dependent variations in measured atmospheric conditions and uncharacterized point spread function (PSF) errors.

In the 1990s, a number of groups continued to explore the aerosol MTF issue. Bruscaglioni et al. (Bruscaglioni et al., 1993) investigated the impact of source-lens separation on the MTF of an optical system operating in a turbid medium via Monte

Carlo numerical calculations. Sadot and Kopeika (D. Sadot and Kopeika, 1993) proposed a “practical” aerosol MTF to account for both the optical bandwidth and field-of-view (FOV) of an imaging sensor. Zege and Kokhanovsky (Zege and Kokhanovsky, 1994) suggested an analytical solution for a scattering medium with large particles, which compared relatively well to published Monte Carlo results.

A flurry of activity followed (Bissonnette, 1994; Kopeika and Sadot, 1995; Dror and Kopeika, 1995; Ben Dor et al., 1997; Kopeika, 1997; Kopeika et al., 1998; Eismann and LeMaster, 2013) including a scientific debate between several publications and comments replying to those articles.

Published as a comment to Sadot and Kopeika (1993), Bissonnette derived order-of-magnitude expressions from the forward-scattering small-angle approximation to show that the scattering MTF is often an insignificant contributor to the overall atmospheric MTF except for special circumstances (Bissonnette, 1994) like precipitation, ice-crystal clouds, or during atmospheric events with large (e.g., tens of micrometers) particles.

In a reply to this comment, Kopeika and Sadot suggest (Kopeika and Sadot, 1995) a misreading of their paper and a faulty perception of scattering phenomena on the part of Bissonnette. They claim that Bissonnette did not fully consider instrumentation effects and that his experimentation equipment was of insufficient sensitivity to draw proper aerosol MTF conclusions.

Dror and Kopeika next published experimental results showing the aerosol MTF as being more dominant than the turbulence MTF (Dror and Kopeika, 1995). Furthermore, their results imply that image-restoration algorithms based on turbulence alone perform more poorly than if aerosol scattering effects are incorporated.

Soon after this, Ben Dor and his collaborators highlighted the open questions in the field of atmospheric blurring effects. In their work (Ben Dor et al., 1997), a physical model is suggested which combines atmospheric properties and aspects of an imaging system like finite-sized detector elements, finite field-of-view of the optics, etc. They successfully compared a PSF predicted by their model to one measured by Bissonnette (1992), and explained that Bissonnette’s experiment was performed with very low levels of atmospheric-scattered radiation and was dominated by scattering inside his imaging system. Regarding the work of Dror and Kopeika (Dror and Kopeika, 1995), Ben Dor et al. suggest that atmospheric-scattered radiation levels during their experiment were five (5) orders of magnitude lower than direct radiation, far below the detection limit of their remote sensing system (Ben Dor et al., 1997). The authors conclude that only in extreme conditions (e.g., dense fog, rain, or sandstorms) would blurring be due to atmospheric scattering, and only then with an imaging system with a very wide instantaneous field-of-view.

Kopeika published a new overview of the aerosol MTF (Kopeika, 1997) which included practical instrumentation effects and suggested that high resolution imaging systems are less impacted by aerosol scattering. Soon after, he and some collaborators published a comment on the Ben Dor et al. 1997 paper which had complained about the omission of raw experimental data in the 1995 Dror and Kopeika paper. To combat this, Kopeika and his co-authors included their raw experimental data in a new article (Kopeika et al., 1998) and defended the linear system assumptions they used to justify their use of Fourier transforms. They also included numerous additional references presenting experimental results (including satellite applications) consistent with their conclusions, in contradiction to the Ben Dor et al. work. They lean on what they term a "wealth of literature" and "everyday reality" (such as the solar aureole) to bolster their position, calling for a system approach which incorporates aerosol and turbulence blur.

Eismann and LeMaster suggested that aerosol scattering is an evident but subtle contributing effect (Eismann and LeMaster, 2013) whose MTF is quite different from aperture diffraction and turbulence. They indicate an issue with other works which obtain an aerosol MTF by dividing a scene-derived composite MTF by the product of models for other MTF constituents to isolate a residual aerosol MTF. They posit two problems with this approach. First, they suggest that errors in the non-aerosol MTF models contaminate the aerosol MTF estimate. Secondly, they question the independence of turbulence and scattering phenomena, which would be required the MTF-division approach to be sound.

More recently, in 2014 Hanafy et al. (Hanafy et al., 2014) explored the effects of scattering and absorption due to haze and fog on the point spread function of an imaging system. The detailed model proposed in that work included the effects of diffraction at the pupil of the imaging system and modeled the point spread function of the direct and scattered radiation as additive in the image plane, as did Ishimaru (Ishimaru, 1997) and others. Modulation transfer functions were computed numerically for a variety of theoretical haze and fog models (Shettle and Fenn, 1979). In a subsequent work, Hanafy et al. (Hanafy et al., 2015) degraded images of a spoke target with their aerosol point spread function (and noise) and then attempted to recover image contrast and clarity by inverting the effect with a Wiener filter. Their work attempted to demonstrate the theoretical performance improvements that can be achieved when detailed knowledge of the atmospheric degradation acting on remotely sensors is understood.

One aim of our work is to (further) explore the additive blurring caused by forward-scattered light accepted by an imaging system operating in an environment containing aerosol particles with a broad size distribution, such as would be expected in many atmospheric clouds. An aerosol modulation transfer function (MTF) is developed analytically from a published aerosol point spread function, providing an avenue for using measured atmospheric conditions to predict optical blurring. Aerosol modulation transfer functions are computed from knife-edge imagery taken of a binary target through laboratory-generated expansion clouds, and conditions measured during this experimentation (e.g., cloud droplet number density and size distribution) are used as inputs to the analytic aerosol MTF. This provides a way to compare the predicted and experimentally-measured aerosol MTFs and explore the closure between modulation transfer functions obtained from directly-measured images and MTFs calculated from theory using measured cloud properties.

The key results of this closure experiment are two-fold. First, the theoretical expression for the aerosol MTF is likely overly simplistic and does not account for broad particle size distributions. Second, the significance of optical blurring from light scattering by aerosol particles is found to depend sensitively on the properties of both the particles and the imaging system.

1.3 Numerical light scattering in monodisperse Matérn spatially-correlated particle fields

Radiative transfer through particle-laden media such as clouds can be impacted by variations in spatial distributions of the particles. This has a multitude of applications ranging from predictions of optical properties of a cloudy atmosphere to biological and energy-generation systems (Davis and Marshak, 2004; Larsen and Vasques, 2011; Zoller et al., 2018). Due to ubiquitous turbulence in the atmosphere, mixing, gravitational settling, and inertial clustering lead to cloud particles becoming spatially-concentrated in some regions. These particle concentrations are referred to as clusters, and the less-concentrated regions they create elsewhere are called voids. Clusters are consistent with positive spatial correlations; the strength and size of clusters or voids can be characterized through the use of a pair correlation function (PCF) or radial distribution function (RDF).

In the vicinity of clusters, the shadowing (obstructing) particles prevent radiation from illuminating the shadowed particles, reducing the absorptive impact of these shadowed particles. In the void regions, more direct radiation traverses the medium than would otherwise occur with homogenous spatial particle distribution (Marshak and Davis, 2005). The net effect of these voids and clusters is thus an increase in the direct radiative transfer through such a medium. Consequently, in the absorptive regime, deviations from Beer-Lambert attenuation should theoretically occur when particle clustering is present.

In the scattering regime, where absorption is essentially non-existent, radiation is either transmitted directly (no collision with particles in the medium) or diffusely (once a particle is encountered, the direction of propagation changes but the photon continues to traverse the medium). Most publications addressing the impact of particle clustering have focused on a purely absorptive regime, but in this work we consider how clustering impacts radiative transfer in forward-scattering media.

Davis et al. and Shaw (Davis et al., 1999; Shaw, 2003) reported atmospheric measurements of cloudy and clear air pockets on spatial scales ranging from km to mm, and as these experimental results became widely known, several publications addressed the causes and impact of this spatial variability. Such spatial correlations between particles within a turbulent cloud can be created by several mechanisms, including inertial clustering (Reade and Collins, 2000) and turbulent mixing (Warhaft, 2000). This spatial correlation has been shown (Frankel et al., 2017; Kostinski, 2001; Larsen and Clark, 2014) to increase the probability of direct transmission through a dilute random medium, as the attenuation of incoherent radiation with depth is often sub-exponential due to a widening of the photon extinction probability distribution. Conversely, in cases where negative spatial correlations exist, super-exponential extinction (Shaw et al., 2002a) is expected.

Consequently, a second aim of our work was to explore via simulation the interactions between light and cloud distributions and investigate the impact of spatial correlation on direct and diffuse radiative transfer (forward and backward) in a scattering medium. This would help determine if deviations from commonly accepted radiative transfer predictions are expected and suggest an experimental setup most likely to detect such a phenomenon.

To explore this problem virtually, we created a Monte Carlo Ray Tracing (MCRT) photon scattering program capable of generating both uniformly random (uncorrelated) spatial distributions as well as spatially-correlated distributions using a Matérn algorithm. The Matérn algorithm is mathematically tractable and has a known closed-form radial distribution function which makes it ideal for rigorous parametric study (Larsen et al., 2014). In such a computer simulation, some of the physical constraints of an actual cloud chamber (such as physical size, maximum optical depth, particle clustering, instrumentation type and location) can be removed or relaxed to determine what would be observed if such an experiment were performed.

Virtual particles are placed in a volume at specified locations, and numerous rays are cast into the scattering medium (Shaw et al., 2002a; Larsen and Clark, 2014; Frankel et al., 2016; Banko et al., 2019). Each ray is traced until it either exits the cloud on the other side unscattered (e.g., direct radiation) or its path intersects a particle. New propagation directions are calculated via random draws from the chosen scattering phase function, and the modified rays continue on until they exit or are scattered again. Periodic boundary conditions were used to create a semi-infinite scattering medium. Direct, diffuse forward and backward irradiances are calculated to determine the optical depth-dependent radiative transfer in the turbid medium. The results of our MCRT program were compared to two-stream flux theory for validation purposes. We also performed studies to determine how many rays need to be cast through each cloud realization to fully characterize the fluxes, as well as how many cloud realizations need to be explored to calculate statistically meaningful average fluxes.

We performed parametric studies to measure the impact of particle size, number of clusters, mean number of particles per cluster and cluster radius. Using the depth-dependent flux results of our scattering simulations, we described the impact of particle clustering on direct, diffuse and backward radiative transfer and detailed the significance of various particle distribution parameters. One question we sought to answer was whether the radial distribution function (RDF) is sufficient to capture the essential physics at play in a medium containing scattering (as opposed to absorbing) particles.

Previous work (Shaw et al., 2002a; Larsen and Clark, 2014; Frankel et al., 2017) suggests that deviations from the expected exponential extinction may depend on parameters in the radial distribution function which describes the statistics of particle clustering. In this work we describe the impact of particle clustering on direct, diffuse and backward radiative transfer and detail the significance of various particle distribution parameters.

The Monte Carlo method (Sobol’ et al., 1974) has often been applied to investigate radiative transfer problems where closed form solutions are challenging or impossible. Monte Carlo simulations have been used to explore atmospheric radiation (Marchuk et al., 1980), engineering radiative transfer (Modest, 1993), and lightning within a cloud (Thomson and Krider, 1982), among others. Efficient radiance calculation via Monte Carlo methods has been discussed previously (Marshak and Davis, 2005) and a detailed description of its application to inhomogeneous media has been presented (Cole, 2005). A clear discussion can be found in Bohren and Clothiaux (2011) but numerous relevant publications can be found on the subject (Plass and Kattawar, 1968; Danielson et al., 1969; Collins et al., 1972).

In a spatially-uncorrelated medium, Monte Carlo scattering simulations are often constructed without assigning physical locations to particles (Marshak and Davis, 2005). In these simulations, the distances that rays travel before redirection are obtained via random draws from an analytic (usually exponential) free-path cumulative density function (CDF) based on the optical depth of the homogeneous medium. Modifications to propagation directions are obtained via random draws from an appropriate scattering phase function (e.g., Henyey-Greenstein or Mie) describing the angular distribution of light intensity scattered by a particle for a given wavelength. This process of computing distance traveled prior to scattering, choosing a scattering angle and re-computing distance traveled is repeated over and over until all rays cast into the medium exit (based on specified “wall” boundary conditions).

Previously, Petty described a method for renormalizing the single scatter and extinction properties of an inhomogeneous cloud volume into values corresponding to a radiatively-equivalent homogeneous medium (Petty, 2002). His method, dubbed the Independently Scattering Cloudlet (ISC) model, treats macroscopic “cloudlets” (a localized dense region of clustered scattering particles) as discrete scatterers which are analogous to individual cloud droplets with modified properties. This idealized geometric approach provides a way to utilize existing radiative transfer methods (e.g., plane parallel codes) in the case of spherically-congregating particle fields.

Frankel et al. proposed a closure model (Frankel et al., 2017), based on the particle RDF, to capture the impact of turbulence-induced particle clustering on direct radiative transmission. Validation was performed by combining ray-tracing and turbulent direct numerical simulation (DNS). The intention of this work, assuming knowledge of local particle and flow statistics, was to correct traditional extinction coefficients which assume homogenous media.

These studies motivated us to compare MCRT results from spatially correlated particle fields to the aforementioned complementary approaches of Petty and Frankel. Our study yielded multiple key results. First, while particle clustering was seen to increase direct transmission (which is consistent with prior publications), diffuse forward radiance was often reduced by an offsetting amount. Second, the peak correlation value and shape of the RDF for our particle fields were both seen to be significant. Our MCRT results showed reasonable agreement with Petty's cloudlet model (Petty, 2002), suggesting a connection between radiative transfer calculations based on continuous correlation functions (Frankel et al., 2017) and those based on cloudlet models (Petty, 2002).

1.4 Predicting experimental measurements of light scattering in realistic polydisperse laboratory atmospheric clouds

As mentioned in the previous section, radiation transfers differently through a spatially correlated medium than through a homogeneous medium due to void and clusters; photons propagate further in less thick regions and experience stronger extinction in more dense regions (Marshak and Davis, 2005). In a prior study (Packard et al., 2019), various directional components of radiative transfer through homogeneous and clustered monodisperse particle distributions were explored with MCRT scattering simulations. While direct transmission was found to increase in the presence of spatial correlation, diffuse forward transmission was seen to be reduced by a similar amount (nearly offsetting the increase in direct transmission).

This result motivated an exploration of experimental designs which might be conducted to measure the presence of particle clustering in a laboratory cloud chamber such as the Pi Cloud Chamber (Chang et al., 2016). The previous study focused on monodisperse distributions with somewhat extreme Matérn clustering; small, dense collections of single-sized droplets were used to evaluate the role of radial distribution functions in predicting radiative transfer. The logical extension of this was to consider polydisperse distributions of discrete particles within a realistic atmospheric cloud, to gauge the extent of deviation from spatially homogeneous theory in more typical atmospheric conditions.

The possibility of verifying numerical findings suggested investigating radiative transfer in an instrumented laboratory system such as the Pi Cloud Chamber. Our aim was to first use computer simulation as a surrogate laboratory to predict future experimental results in the Pi Chamber and develop a method for sensing particle clustering. A Large Eddy Simulation (LES) code was used to generate particle clouds with properties (such as optical thickness, particle size distribution function and spatial correlation) realistic for a laboratory-generated mixing cloud. Polydisperse LES-exported particle distributions were explored with our MCRT scattering code, and comparisons were made between particle fields with LES-positioned droplet locations and uniformly random distributions (which lacked spatial correlation). As before, directional radiative transfer components (e.g., direct, diffuse forward, backward and total forward flux) were compared to determine the impact of realistic spatial correlation in a laboratory setting.

A number of published laboratory investigations related to light propagating through turbulent media exist. Several decades ago, Kuga and Ishimaru studied image transmission through random distributions of polystyrene microspheres suspended in water (Kuga and Ishimaru, 1985), comparing experimental results with radiative transfer equations using the small-angle approximation. Soon after they followed this publication with another article (Kuga and Ishimaru, 1986) which built upon the previous one, adding the ability to model a layered medium with different refractive indices. Their improved model showed better agreement with their previous experimental results.

In another laboratory study, Yuan et al. conducted light propagation experiments in a turbulent water tank, where temperature gradients were used to simulate the entrainment zone at the top of a convective boundary layer (Yuan et al., 2014). By heating the tank bottom, measuring transient temperature profiles and imaging profiles of laser light from various vantage points, turbulence parameters were calculated. These obtained parameters were used to numerically simulate light propagation in a turbulent field and successfully reproduce the observed light fluctuations (induced by temperature-dependent refractive index, not particle scattering). More recently, Pawar and Arakeri used brine and fresh water to create an unstable density difference, allowing them to study laser angle of arrival variations in a buoyancy-driven turbulent medium (Pawar and Arakeri, 2016).

Rodriguez-feo's recent master's thesis focuses on non-exponential light extinction in a turbulent cloud chamber (Rodriguez-feo Bermudez, 2019). In that work, numerical simulations are used with chamber-measured particle size distributions to predict extinction rate and optical depth assuming a lack of spatial correlation; these results are compared to direct measurements of light extinction through the turbulent laboratory cloud chamber. A beam splitter and two photo-diodes (one near the laser source and one on the opposite end of the cloud-filled chamber) are used to compare light intensities on each side of the turbulent cloud and compute extinction. Significant deviations from exponential extinction are observed, especially during larger temperature gradients.

Of primary interest to our work was the effect that local variations in particle number density and optical thickness have on the mean direct and diffuse flux (which shows the average impact of spatial correlation) and the standard deviation that might be measured through a fluctuating mixing cloud. The key result of our study is that, in the presence of spatial correlation, differences exist in both mean flux and standard deviation about the mean. This suggests that an experiment in a laboratory cloud chamber such as the Pi Chamber could be designed to detect the presence of spatial correlation, since direct and diffuse forward flux appear to be impacted to a measurable extent. This finding, based on polydisperse particle size distributions functions achievable in the Pi Chamber, suggests the possibility of fruitful laboratory experimentation in the future.

2 Measuring the detector-observed impact of optical blurring due to aerosols in a laboratory cloud chamber

This chapter details a comparison of modulation transfer function (MTF) predictions made from measured Pi chamber cloud properties and MTF measurements calculated from laboratory cloud chamber-capture knife edge imagery. This work was published in full form in the Journal of Applied Remote Sensing.[1] [2]

2.1 Abstract

Deleterious effects of the atmosphere on remotely acquired images includes absorption and scattering of light by aerosol particulates, which not only attenuates the signal but can potentially cause blurring due to forward-scattered light accepted by the imaging system. Proposed aerosol scattering models (e.g., Ishimaru) provide a method for simulating the contrast and spatial detail expected when imaging through atmospheres with significant aerosol optical depth. This work explores closure between modulation transfer functions (MTFs) obtained from directly measured images and MTFs calculated from theory using measured cloud properties. The closure experiments are performed in a laboratory cloud chamber in which cloud droplet number density and size distribution are directly measured. Images of a binary knife-edge target were taken with an optical detector on the other side of a water cloud generated through reduction of pressure in the humidified chamber. The key results of this closure experiment are: the theoretical expression for the aerosol MTF is likely overly simplistic and does not account for broad particle size distributions. The significance of optical blurring from light scattering by aerosol particles depends sensitively on the properties of both the particles and the imaging system.

2.2 Introduction

The resolution of optical imaging systems is influenced not only by system parameters, such as lens and detector properties, but also by the atmosphere along the target-to-sensor slant path. Specifically, the presence of turbulence (Roggemann and Welsh, 1996; Ishimaru, 1997; Holst, 2008; Wyngaard, 2010a) or aerosol particles (Dror and Kopeika, 1995; Ishimaru, 1997; Kopeika and Arbel, 1999) can degrade image contrast and resolution. This paper addresses the influence of aerosol and cloud particles on the blurring of optical images by making a comparison between theoretical expressions

---

[1] Corey D. Packard, Raymond A. Shaw, Will H. Cantrell, Greg M. Kinney, Michael C. Roggemann, and John R. Valenzuela "Measuring the detector-observed impact of optical blurring due to aerosols in a laboratory cloud chamber," Journal of Applied Remote Sensing 12(4), 042404 (5 July 2018). https://doi.org/10.1117/1.JRS.12.042404

[2] © 2018 Society of Photo-Optical Instrumentation Engineers (SPIE). Used with permission.

accounting for aerosol blurring for realistic optical sensor parameters, and direct measurements of blurring due to controlled cloud conditions in a laboratory cloud chamber. This work builds on a proposed closure experiment previously published by Packard et al. (Packard et al., 2016) in the 2016 Proceedings of SPIE; portions of that conference paper have been included in this article for clarity and completeness.

Generally speaking, particles present in the atmosphere can absorb and scatter incident radiation; this combination of absorption and scattering, whereby propagating energy is attenuated and image contrast is subsequently reduced, is referred to as atmospheric extinction. In the case of extinction via scattering, outgoing radiation is distributed over a large range of angles. Near the Rayleigh limit where particles are small compared to the optical wavelength ($a \ll \lambda$), the pattern of scattered light is almost isotropic (Salby, 2012). This results in the frequent occurrence of a large angle between the direction of incident and outgoing radiation, often placing the scattered energy outside an imaging sensor's field of view. This reduces the percentage of incident energy that arrives within the pupil plane and is available for imaging purposes. The severity of these energy extinction components depends on optical wavelength, particle size and abundance, scattering and absorption cross sections and efficiency factors, and refractive index. This extinction (attenuation) typically leads to image contrast reduction, as some energy radiated from the scene never arrives at the imaging sensor but additional energy scattered from elsewhere does reach the detector. For particles of the same order as or larger than the wavelength, Mie theory (Salby, 2012) shows that the fractional power scattered in the forward direction increases nearly monotonically with particle size. Thus, the light scattered (predominantly) forward by large aerosols and cloud particles is redirected slightly but often still lies within a sensor's field of view and is therefore important to consider. This minor redirection is sometimes referred to as "small angle" scattering, and the impact this phenomenon has on imagery is sometimes referred to as the adjacency effect (Dror and Kopeika, 1995; Kopeika and Arbel, 1999) since incident photons are imaged by pixels adjacent to those by which they would have been detected in the absence of scattering. This slight shift in photon arrival angles results in image blurring, often explained in optical terms by a modified point spread function (PSF). Even idealized optical systems are unable to perfectly focus incident energy from a point source back to an infinitely small point; this results in focused energy from a point source being measured with some finite size (or spread) at the image plane (Hecht, 2002; Goodman, 2005). Deviations in photon arrival angle due to small-angle aerosol-driven forward scattering would warp a plane wave from a distant point source, thus rendering the focused "point" something other than that described by standard diffraction-limited PSFs.

The attenuation of energy due to scattering and absorption by atmospheric aerosols is thought to be well understood, though there appears to be some dispute over research findings and the level of significance of this phenomenon (Bissonnette, 1992; McDonald et al., 1992; Bruscaglioni et al., 1993; D. Sadot and Kopeika, 1993; Dan Sadot and Kopeika, 1993; Dror and Kopeika, 1995; Kopeika and Sadot, 1995; Ben Dor et al., 1997; Kopeika, 1997; Kopeika et al., 1998; Eismann and LeMaster, 2013). Validating existing theoretical models (Deirmendjian, 1969; Lutomirski, 1978; Kuga and Ishimaru, 1985; Kopeika, 1987) for image quality depends on accurate characterization of both incident light and particle size distribution function. Most comparison between theory and experiment has been performed over long pathlengths in the open atmosphere, and particle size distributions are not well characterized over the full propagation path. The necessary assumptions of statistical homogeneity in space and statistical stationarity in time are always in question, and are often cited when discrepancies are observed.

Our research seeks to more rigorously control and characterize atmospheric conditions by generating spatially-uniform cloud conditions in a laboratory cloud chamber, such that the impact on optical blurring resulting from realistic aerosol and cloud particle size distributions − instead of previous monodisperse experiments (Kuga and Ishimaru, 1985; Donelli et al., 1991) − can be determined. By implementing a one-way path (with photons traversing only from target to sensor) with no background sources, conclusions can be drawn without interference from airlight, path radiance or other conflating sources of energy. This measurement setting provides a unique tool for closure experiments. By creating and characterizing a realistic aerosol-laden atmosphere, the impacts of aerosol scattering can be both measured directly (via imaging) and predicted indirectly (using measured boundary conditions as input to theoretical expressions for optical depth and aerosol MTF).

This work will propose a theoretical spatial frequency-domain modulation transfer function (MTF) based on a point spread function (PSF) which incorporates aerosol scattering and aperture diffraction effects. A controlled laboratory experiment, where clouds are generated inside a turbulent cloud chamber, is described. Measured droplet size distributions are presented, and theoretical results using aerosol-driven PSF and MTF expressions are explored with these measured atmospheric inputs. Examples of imagery measured through a chamber-generated expansion cloud are included, and a methodology for computing an aerosol MTF from chamber-measured imagery and comparing it to atmospheric theory is described. Experimentally-obtained aerosol MTFs are presented and compared to theoretical predictions, and the impact of optical imaging system parameters and experimental design considerations are discussed. Specifically, the significant dependence of observed aerosol scattering on sensor specifications such as dynamic range, aperture diameter and focal length are detailed. The key result of this work is the development and verification of a validation strategy where aerosol-induced effects are experimentally obtained and compared to theoretical predictions using measured boundary conditions (droplet size distribution, etc.). In summary, this paper proposes and details the results from a closure experiment for measuring an aerosol MTF and comparing it to theoretical predictions predicated on measured impact variables.

2.3 Aerosol Scattering Theory

This section will detail the theoretical underpinnings of an aerosol scattering prediction model (both PSF and MTF). Relevant atmospheric physical relationships will be described, and a description of the aerosol scattering impact (specifically due to clouds and fog) will be given.

2.3.1 Theoretical Approach for Predicting the Impact of Aerosol Scattering

Mie theory, when applied to scattering by atmospheric aerosols, can be used to predict the wavelength- and size-dependent impact of particles on scattering and absorption of incident energy. The resultant extinction cross section, σ_{ext}, is the sum of scattering and absorption cross sections (Bohren and Clothiaux, 2011). This extinction parameter has units of area and can be expressed (van de Hulst, 1981; Ishimaru, 1997; Bohren and Huffman, 2004) as the multiplicative combination of physical cross sectional area (of a particle) and dimensionless extinction efficiency, Q_{ext} (relative to geometric cross section). This extinction cross section represents the fractional area of the incident beam removed *in toto* via scattering and absorption. In the visible spectrum, fog and cloud droplets (assuming a complex refractive index for liquid water, $m_{H2O} = 1.333 + i10^{-8}$) have efficiency factors of $Q_{ext} \approx Q_{sca} \approx 2$, and $Q_{abs} \approx 0$ (Salby, 2012). The physical cross sectional area and efficiency factors are thus combined to calculate extinction, scattering and absorption coefficients (σ_{ext}, σ_{sca} and σ_{abs} respectively).

Mie scattering theory and other atmospheric physics relationships are dependent on particle radius, which is important because actual atmospheric cloud droplet size distributions are not monodisperse. Therefore the distribution $n(a)$ must be accounted for, where $n(a)da$ is defined as the number density of droplets between a and $a+da$, i.e., the integral over the distribution, from radius of zero to infinity, results in the total droplet number density. Physical predictions are often based on idealized aerosol or cloud droplet size distributions; in the case of fog, parametric models employing a modified Gamma distribution are common (Deirmendjian, 1969; Shettle and Fenn, 1979; Shirkey and Tofsted, 2006). Atmospheric extinction, scattering and absorption coefficients [m^{-1}] are functions of the respective cross sections and particle distribution functions and must be integrated over the range of droplet radii. For example, the total extinction coefficient (Grainger, 2012) is performed with the expression $k_{ext}(\lambda) = \int_0^\infty \sigma_{ext}(\lambda, a)\, n(a)\, \mathrm{d}a$. The additive relationship between the integrated extinction coefficients can be expressed (Ben Dor et al., 1997) as $k_{ext}(\lambda) = k_{sca}(\lambda) + k_{abs}(\lambda)$. Atmospheric optical depth (Liou, 2002) is given as

$$\tau(\lambda) = \int k_{ext}(\lambda, z)\, \mathrm{d}z \tag{1}$$

and together these expressions shown the relationship between particle size distribution function $n(a)$, scattering cross section, scattering coefficient and optical depth. Single scattering albedo is defined (Grainger, 2012) as

$$\omega_o^t(\lambda) = \frac{k_{sca}(\lambda)}{k_{ext}(\lambda)}\ . \tag{2}$$

Together, these relationships can be used to predict the atmospheric extinction and scattering.

Now the combined effect of aerosol scattering and absorption with an optical system are considered. The total PSF for a remote sensor imaging through a scattering medium (Bissonnette, 1992; Ishimaru, 1997; Ben Dor et al., 1997; Hanafy et al., 2015) is given as

$$\mathrm{PSF}_t(r) = \mathrm{PSF}_{dir}(r) + \mathrm{PSF}_{sca}(r) \tag{3}$$

and can be considered an additive combination of direct and indirect (scattered) point spread functions. Expressions for these two separate point spread functions of an optical system impacted by aerosol scattering have been given (Ishimaru, 1997) as

$$\mathrm{PSF}_{dir}(r) = exp(-\tau)\left(\frac{D}{2r}\right)^2 J_1^2\left(\frac{kDr}{2f}\right) \tag{4}$$

and

$$\mathrm{PSF}_{sca}(r) = \left(\frac{1.64a_{mode}D}{\lambda f\sqrt{Rk_{sca}}}\right)^2 exp\left[-\tau\,(1-\omega_o^t) - \left(\frac{3.28a_{mode}r}{\lambda f\sqrt{Rk_{sca}}}\right)^2\right]. \tag{5}$$

In these expressions *D* is aperture diameter, *f* is focal length, *k* is optical wavenumber and *r* is physical separation on the image plane from the optical axis. The term J_1 in equation (4) refers to a first-order Bessel function of the first kind. In the second expression given in equation (5), *R* is propagation range and a_{mode} is aerosol modal radius.

For an incoherent imaging system, the symbol $\mathcal{H}$ represents the spatial frequency domain version of the system transfer function and is referred to as the optical transfer function (OTF). If the total point spread function of an incoherent imaging system is denoted $|h|^2$, then the OTF can be written (Goodman, 2005) as

$$\mathcal{H}(\xi,\eta) = \frac{\mathcal{F}\{|h|^2\}}{\int_{-\infty}^{\infty}\int_{-\infty}^{\infty}|h(x,y)|^2\,\mathrm{d}x\,\mathrm{d}y}. \tag{6}$$

The magnitude of the OTF is called the modulation transfer function, MTF (Goodman, 2005; Holst, 2008), expressed as

$$MTF(\xi,\eta) = |\mathcal{H}(\xi,\eta)|\,. \tag{7}$$

Because integration is linear and superposition applies, the aerosol MTF can be written as

$$\mathrm{MTF}_t(u,v) = \left|\frac{\iint_{-\infty}^{\infty}\mathrm{PSF}_{dir}(x,y)\,e^{-j2\pi(xu+yv)}\mathrm{d}x\,\mathrm{d}y + \iint_{-\infty}^{\infty}\mathrm{PSF}_{sca}(x,y)\,e^{-j2\pi(xu+yv)}\mathrm{d}x\,\mathrm{d}y}{\iint_{-\infty}^{\infty}\mathrm{PSF}_{dir}(x,y)\,\mathrm{d}x\,\mathrm{d}y + \iint_{-\infty}^{\infty}\mathrm{PSF}_{sca}(x,y)\,\mathrm{d}x\,\mathrm{d}y}\right|. \tag{8}$$

Since both of the PSF components are circularly symmetric, we can use the Fourier-Bessel (Hankel) transform instead and write the aerosol MTF as

$$\mathrm{MTF}_t(u,v) = \left| \frac{\mathcal{F}_r\{\mathrm{PSF}_{dir}(r)\} + \mathcal{F}_r\{\mathrm{PSF}_{sca}(r)\}}{\iint_{-\infty}^{\infty} \mathrm{PSF}_{dir}(r)\, r\, \mathrm{d}r\, \mathrm{d}\theta + \iint_{-\infty}^{\infty} \mathrm{PSF}_{sca}(r)\, r\, \mathrm{d}r\, \mathrm{d}\theta} \right|. \qquad (9)$$

The resulting closed-form aerosol MTF, where ρ represents spatial frequency, is based on the Ishimaru PSFs and is given (Ishimaru, 1997) as

$$\mathrm{MTF}_t(\rho) = \left| \frac{e^{-\tau_{atm}} \frac{2}{\pi} \left[\cos^{-1}\left(\frac{\rho\lambda f}{D}\right) - \left(\frac{\rho\lambda f}{D}\right) \sqrt{1 - \left(\frac{\rho\lambda f}{D}\right)^2} \right] + exp\left\{ -\left(\frac{\pi\rho\lambda f \sqrt{R k_{sca}}}{3.28 a_{mode}} \right)^2 \right\} e^{-\tau_{atm}(1-\omega_o^t)}}{e^{-\tau_{atm}} + e^{-\tau_{atm}(1-\omega_o^t)}} \right|. \qquad (10)$$

2.3.2 Evaluating the Aerosol PSF and MTF using Theoretical Fog Models

The MTF expression just obtained attempts to combine both the effects of light scattering by particles and diffraction by the optical-system aperture. Its behavior can be understood by considering idealized parametric fog models (Shettle and Fenn, 1979). We recognize the direct component of the aerosol PSF, given in equation (4), as an atmospherically-attenuated Airy disk; the unattenuated version of this expression is the PSF due to aperture diffraction (Goodman, 2005; Hecht, 2002). Thus the PSF, when plotted as a function of radial distance from the optical axis, should be dominated by a Bessel function resulting from aperture diffraction. This can be seen in panel (a) of Figure 2.1, which shows the direct component of the aerosol PSF for three fog models. These plots assume a propagation distance of 150 m, an optical wavelength of 550 nm, and an imaging system with a 10 cm focal length and 2 cm aperture diameter. The parametric fog models (Shettle and Fenn, 1979) used for demonstration in Figure 2.1 have modal droplet radii of 2 µm and 4 µm for radiation fog ("moderate" and "heavy", respectively). The heavy advection fog model has a modal droplet radius of 10 µm.

The scattered component, shown in panel (b) of Figure 2.1, is at a much lower intensity but is spread over a much greater distance from the optical axis. The combination of these direct and scattered components, referred to as the total PSF, is shown (normalized) in panel (c) of Figure 2.1.

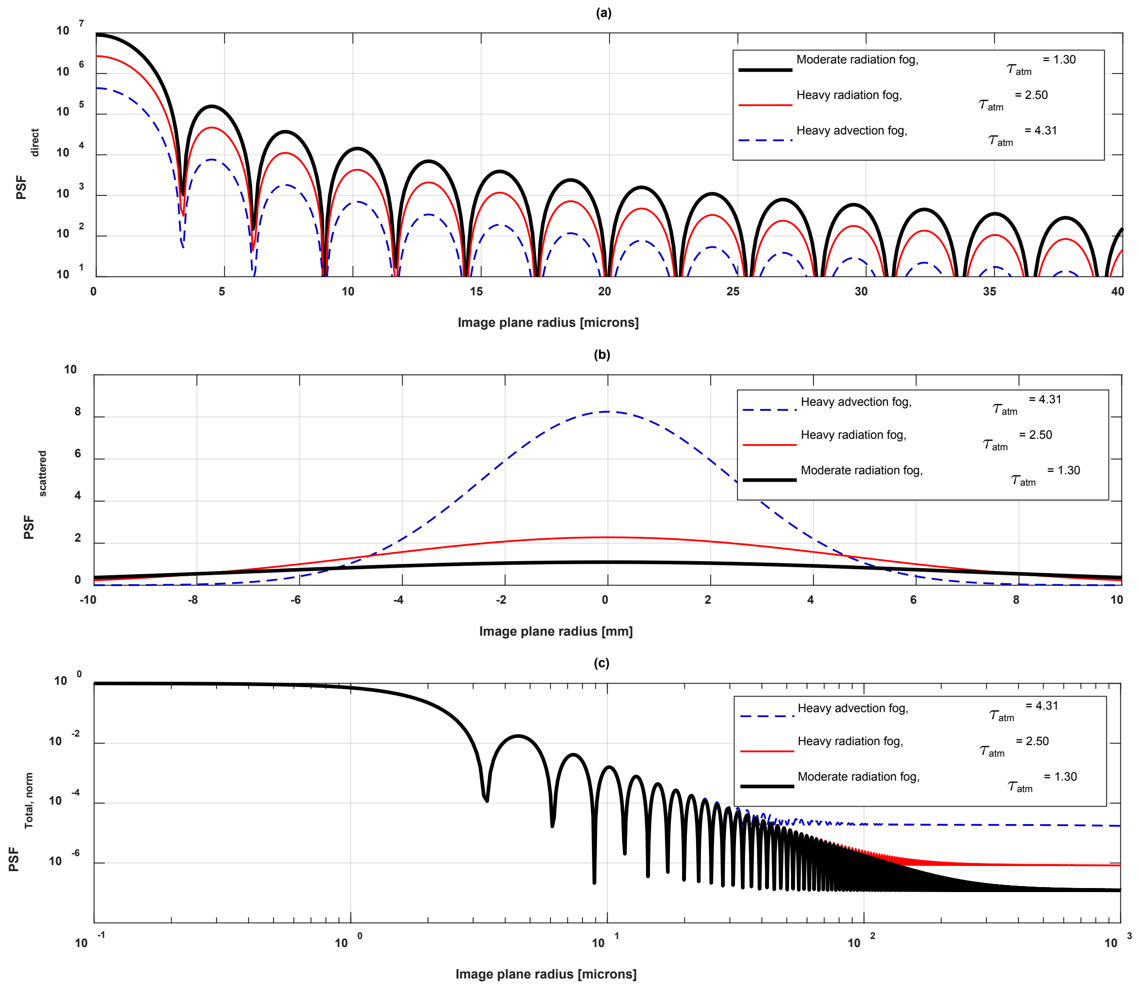

Figure 2.1. Aerosol point spread functions evaluated for 150m propagation using atmospheric parameters from various theoretical fog models. (a) Upper panel shows attenuated direct component, and (b) center panel is the aerosol-scattered component. (c) Lower plot shows (normalized) total point spread function. These PSF predictions assume λ=550nm, focal length = 10cm, aperture diameter = 2cm.

Since the total PSF is taken as additive, and due to the superposition property of linear systems, it follows that the aerosol MTF can be written as a summation of these two components. It also follows that one of those components should be related to aperture diffraction, and we recognize the first term in the numerator of equation (10) as an optical depth-scaled version of the diffraction-limited MTF for a circular aperture (Goodman, 2005), given here for reference as

$$\mathcal{H}(\rho) = \frac{2}{\pi}\left\{\cos^{-1}\left(\frac{\rho\lambda f}{D}\right) - \left(\frac{\rho\lambda f}{D}\right)\sqrt{1-\left(\frac{\rho\lambda f}{D}\right)^2}\right\}. \qquad (11)$$

Plots of the aerosol MTF given in equation (10) are shown in Figure 2.2 where panels (a), (b) and (c) illustrate the total, direct and scattered components (respectively).

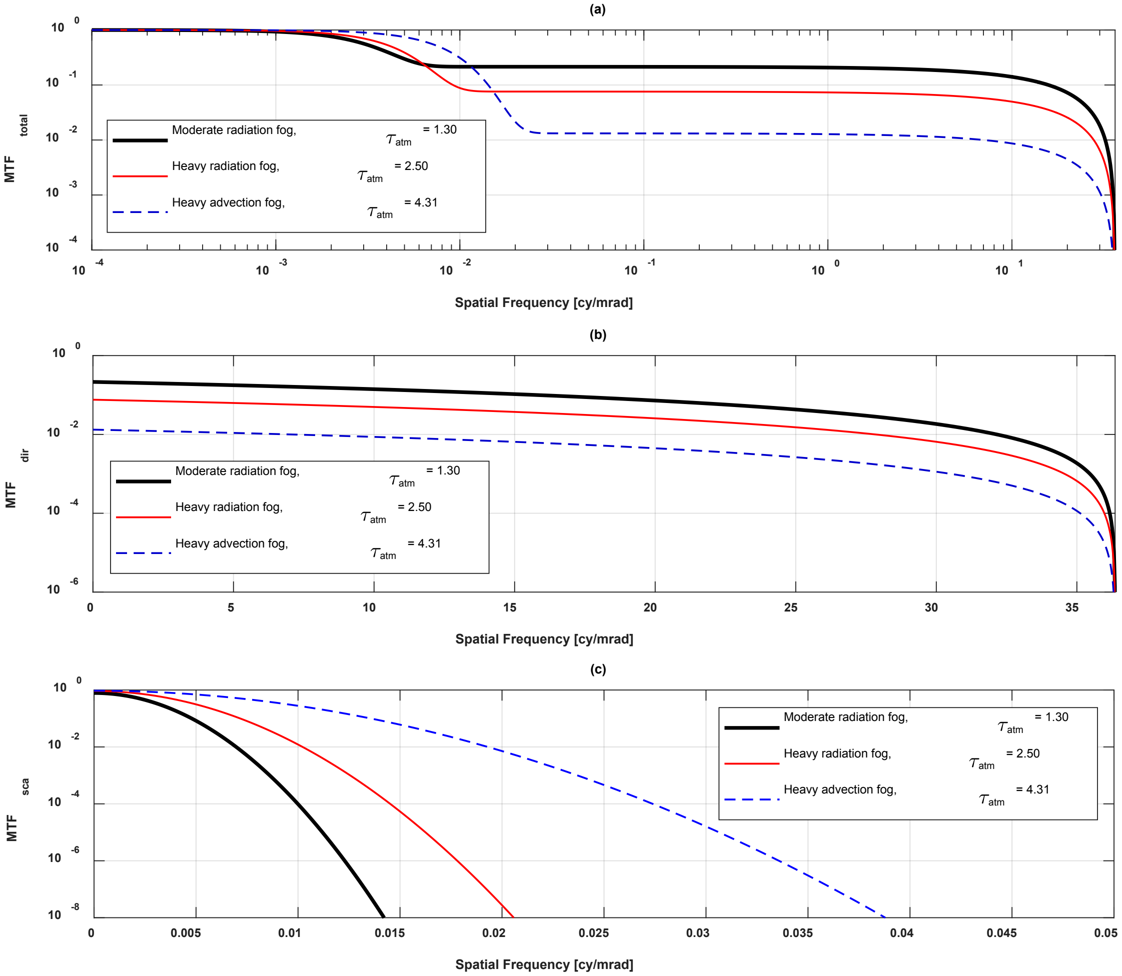

Figure 2.2. Aerosol modulation transfer function for 150m propagation using several theoretical fog models. (a) Upper panel shows the total MTF, (b) center panel is the direct component and panel (c) shows the aerosol-scattered component. These MTF predictions assume λ=550nm, focal length = 10cm, aperture diameter = 2cm.

The relationship between the aperture PSF and the first term in the aerosol MTF numerator is evident in panel (b) of Figure 2.2, which shows a plot of the direct component of the aerosol MTF. The familiar shape of an aperture MTF is apparent, though the presence of a scaling factor reduces its contribution at all spatial frequencies. Recall that the diffraction-limited optical cutoff frequency for incoherent imaging, in cycles per milliradian (mrad), is

$$\rho_{oco} = \frac{D}{\lambda} \tag{12}$$

For an imaging system with central wavelength λ=550 nm and D = 2 cm, the expected optical cutoff frequency of 36.4 cy/mrad is evident in panels (a) and (b) of Figure 2.2. Panel (c) emphasizes the fact that the scattered component of the MTF is predicted to contribute most significantly at very low spatial frequencies.

2.4 Experimental Methodology

This section will detail the experimental methodology employed to study the blurring effects of light scattering by cloud/fog aerosol. The laboratory technique begins with the generation of an expansion cloud using the cloud chamber at Michigan Technological University (MTU). The cloud microphysical properties present in the chamber are measured, allowing for predictive simulation of aerosol effects. Imagery of a binary knife-edge test pattern is captured, with the aerosol cloud between the pattern and the detector. MTF curves are then computed from this measured imagery. This experimental method provides an avenue for comparison between MTF curves obtained directly from a blurred image, and predictions made using theoretical expressions that incorporate measured particle size distributions existing during image capture.

2.4.1 Cloud Chamber

Experimental verification of aerosol effects are performed using MTU's turbulent cloud chamber (known as the "Pi Chamber", depicted in Figure 2.3; see Chang et al. (Chang et al., 2016) for a more detailed description of its capabilities). This controllable and well-characterized laboratory atmosphere is capable of pressures below 100 hPa and temperatures from -55 to +55 °C. Additionally, humidity and aerosol concentrations are controllable. The injection of aerosol particles is controlled with a constant output atomizer (e.g., from a water solution of 0.1 g/L concentration of NaCl). These experimental conditions can be combined to form and sustain clouds, both mixing and expansion clouds, in an instrumented laboratory setting for measuring the impact of clouds on radiation propagation.

Phase Doppler interferometry (PDI) is used for characterizing the particle size distribution present in the cloud chamber after aerosol particles are injected and cloud droplet growth has occurred under controlled, supersaturated conditions. Past experiments (Chang et al., 2016; Chandrakar et al., 2016, 2017; Desai et al., 2017) have demonstrated the ability to create cloud droplets ranging from 10-50 μm. Turbulence can also be generated by Rayleigh-Benard convection, driven by a negative vertical temperature gradient. Past turbulence measurements have shown RMS velocity fluctuations of ~10 cm/s and kinetic energy dissipation rates of 1 mW/kg. These two effects can be used to study the optical blurring, driven by aerosol scattering and atmospheric turbulence (if desired), which occurs as a consequence of the chamber's realistic cloud droplet size distribution and turbulent nature.

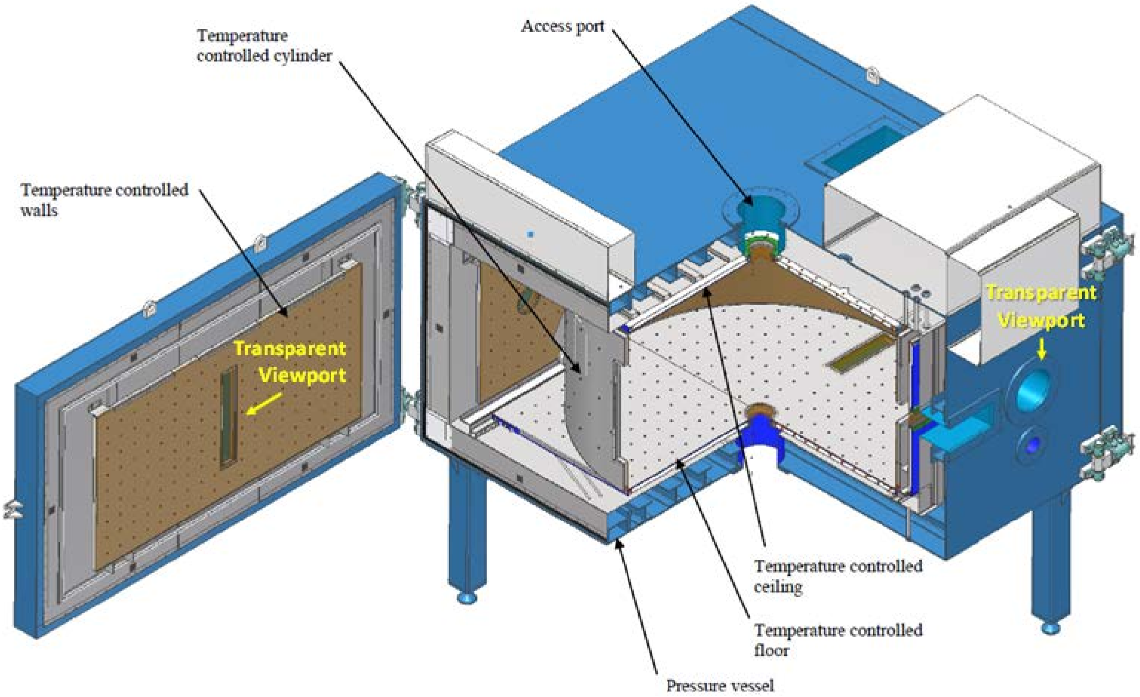

Figure 2.3. A cutaway schematic of the cloud chamber at Michigan Technological University, with one door open and the (removable) cylindrical thermal panel in place. The horizontal propagation path through this atmospheric chamber is approximately 2m. Figure from Chang et al. (Chang et al., 2016) ©American Meteorological Society. Used with permission.

To create an expansion cloud, the pressure in the chamber is reduced, resulting in a reduction in the air temperature, and a resulting increase in the relative humidity. This eventually generates supersaturated conditions so that water vapor condenses on sub-micrometer aerosol particles (cloud condensation nuclei) and result in a cloud. Air pressure is reduced from standard atmospheric pressure to approximately half that (~500 hPa) over the course of several minutes. The number concentration of cloud droplets formed during expansion is measured with PDI. The resulting expansion clouds tend to be more optically dense than mixing clouds. Additionally, expansion clouds typically lack strong turbulence and persist for a lifetime on the order of several minutes.

A mixing cloud can be generated by creating a negative temperature gradient between the bottom and top surfaces of the cloud chamber interior. Warm, saturated air rising from the bottom surface mixes with the cold, saturated air originating at the top surface at constant pressure. The method for creating the resulting cloud is analogous to walking outside and exhaling on a cold day. Again, NaCl particles are often used to produce an aerosol-laden air stream which can be diluted with as much (or little) particle free air as required to reach the desired number concentration. The resulting mixing cloud can persist for many hours, providing an avenue for studies which require large periods of sampling time. These strong temperature gradient conditions allow cloud droplets to grow to 40 or 50 µm in diameter. The temperature gradient creates Rayleigh-Bénard convection, which in turn generates turbulence in the chamber. Temperature fluctuation measurements suggest a single major convection cell fills the chamber interior; this has been verified via computational fluid dynamics (CFD) simulation. Previous investigations into the steady, convective-turbulent cloud conditions present during these mixing clouds show the expected inertial subrange with -5/3 Kolmogorov scaling.

Laser sheet imaging was performed to illuminate cloud droplet distributions in the chamber and photograph the resulting cloud structure. Examples are shown in Figure 2.4, illustrating the turbulent droplet structure in two planes (left image) as well as an expansion cloud distribution (right).

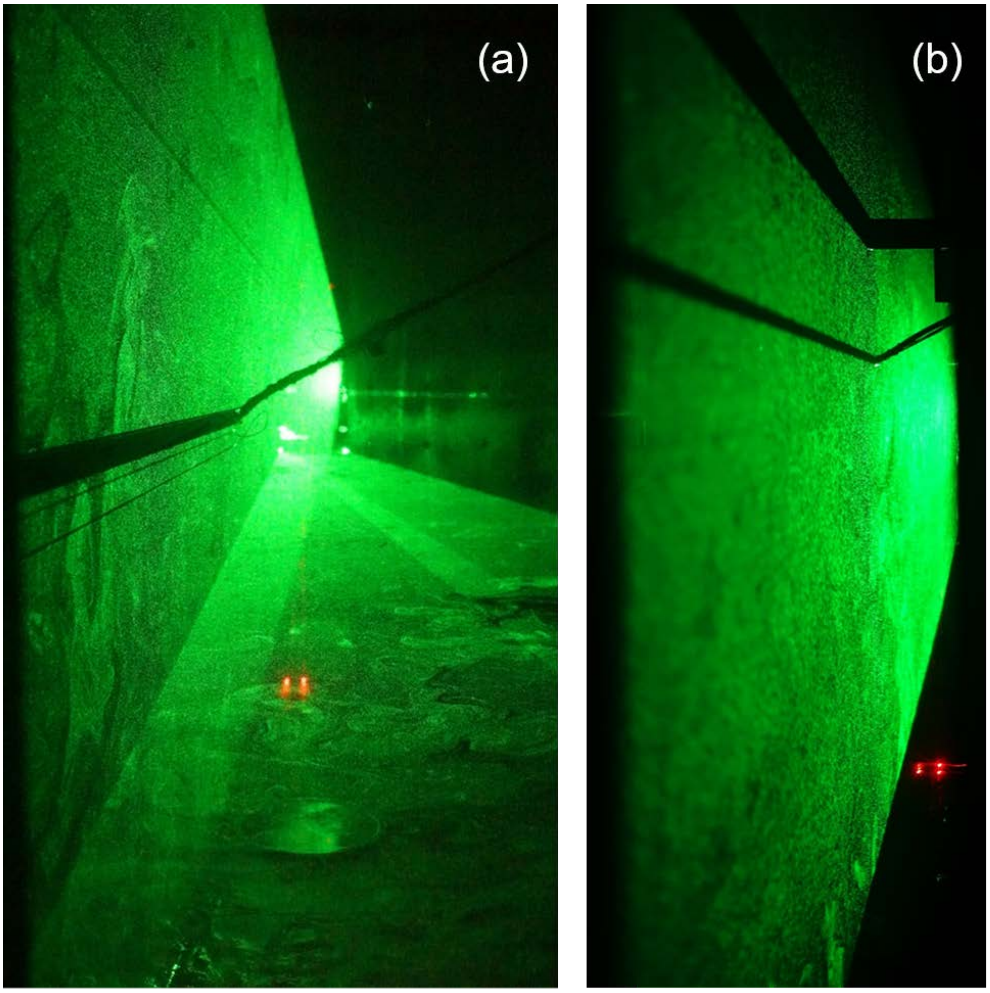

Figure 2.4. (a) Imagery showing the chamber-generated turbulent cloud droplet structure in two planes using both vertical and horizontal laser sheets (λ=532nm). "Swirls" in the laser-illuminated cloud plane demonstrate the presence of turbulence. (b) Photograph showing vertical slice of an expansion cloud droplet distribution, again using a vertical laser sheet for aerosol illumination. Turbulence is nearly absent in expansion clouds, but optical depth is higher. Photo credit: Audrey Barnett.

2.4.2 Experimental Setup

By capturing images using light that has propagated through a 2m x 2m x 1m turbulent cloud chamber, the extinction and scattering effects of the atmosphere can be studied in a controlled environment. Spatial (PSF) and spatial frequency (MTF) analysis can be performed on images taken through various optical viewports and these experiment-based responses can be compared to existing predictive theoretical models.

In the experiments examined in this paper a series of expansion clouds (as well as a mixing cloud) was created within the cloud chamber. A monochromatic visible-light camera with a detector resolution of 1384x1032 and a pixel size of 6.45 µm (the FLIR GS3-U3-15S5M-C, formerly from Point Grey Research), was selected to image through the chamber. This optical system was outfitted with a 75mm focal length f/22 manual varifocal lens and used to image a black-and-white knife edge target, half of which was constructed from aluminum sheet stock painted ultra-flat (diffuse) black to prohibit light transmission and avoid specular reflections. The other half employed a semi-transparent material to diffuse the light transmitted from an LED-backlit illumination source placed behind the binary target.

The knife edge target was affixed to the exterior of one viewing porthole, and the camera was placed against the exterior of the opposite porthole, creating a 2 meter propagation path through the chamber. Black cloth was draped behind the camera and all unused optical chamber viewports to eliminate stray light and create a one-way light measurement path. This setup ensured that the photons measured by the monochromatic camera had only passed from the target to the camera through the cloud chamber, with minimal stray light contaminating the imagery. This was done to closely mimic the one-way propagation considered by Hanafy et al. where scattered airlight from other sources was not considered (Hanafy et al., 2015, 2014).

An illustration of this experimental setup is shown in Figure 2.5 (left), along with example images taken in the presence and absence (aerosol and control, respectively) of an expansion cloud. Control images were taken while the cloud chamber was not operating (i.e., room temperature, standard pressure, no aerosols).

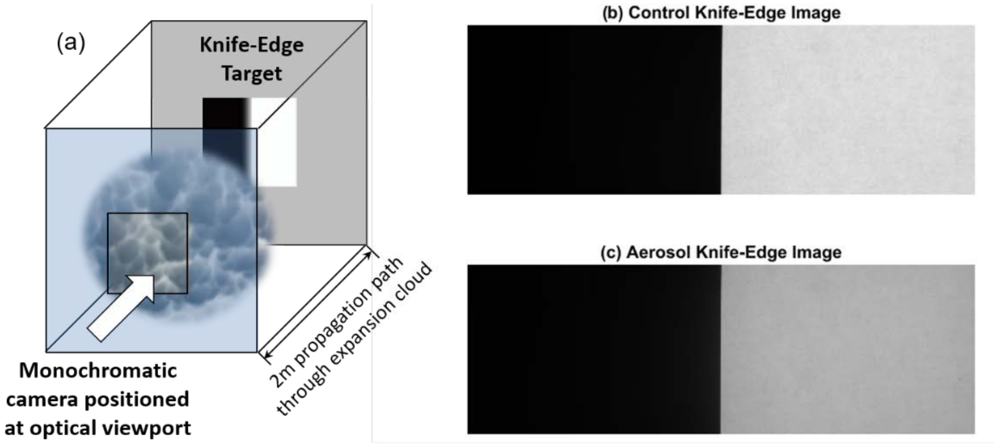

Figure 2.5. (a) Illustration of experimental setup with monochromatic camera, positioned outside cloud chamber near an optical viewport, focused through the expansion cloud on binary knife-edge target located just outside opposite viewport. (b) Representative example of measured control image. (c) Example of knife-edge image taken through expansion cloud, demonstrating attenuation due to aerosol scattering in the visible band.

2.4.3 Experimental MTF Calculation Method

The need for precise MTF measurements requires employing a procedure such as the edge spread method (Wyatt, 1991; Reichenbach et al., 1991; Dror and Kopeika, 1995; Tzannes and Mooney, 1995; Holst, 1998; Boreman, 2001; Nugent et al., 2010), where a target with a sharp black-white transition is imaged and a near-continuous MTF is calculated. According to Boreman, an *edge spread function* (ESF) can be defined as the convolution of the system PSF with a step function (Boreman, 2001).

$$ESF(x) = PSF(x, y) * step(x) \tag{13}$$

This inevitably results in a broadened black/white transition, since the PSF of an imaging system is always broader than a delta function. Consequently, the originally-sharp black/white transition is blurred into a gradient with a finite slope. A *line spread function* (LSF) can be described as the spatial derivative (in the direction of change) of the edge spread function.

$$LSF(x) = \frac{d}{dx} ESF(x) \tag{14}$$

Both the ESF (directly) and LSF (indirectly via spatial gradient) can be obtained from the measured image. Boreman shows that the system MTF is the Fourier transform of the LSF (Boreman, 2001), meaning that the aerosol MTF can be calculated from the LSF obtained via imaging a black/white step function target:

$$MTF(\rho) = \mathcal{F}\{LSF(x)\} \tag{15}$$

This system-level MTF includes effects from the atmosphere, lens and detector. Although not considered in this study, turbulence effects can also be measured simultaneously from this same edge imagery, another benefit of this method (Dror and Kopeika, 1995).

2.4.4 Imaging System Considerations

Since the aerosol MTF was to be contrasted with the aperture diffraction MTF from which it was developed, the lens used for the chamber imaging studies was chosen to allow adequate MTF sampling with the available detector pixel spacing. Since a digitized edge spread function (and indirectly a line spread function) would be used to compute an aerosol MTF, the detector cutoff frequency must be greater than the optical cutoff frequency to avoid aliasing. The cutoff frequency of the detector is determined by half the inverse of the pixel size, and the optical cutoff frequency is determined by the wavelength, aperture diameter and focal length. Consequently, the smallest pixel footprint available yields the largest detector cutoff frequency. Once a detector with a pixel pitch of 6.45 μm and a corresponding detector cutoff frequency of 11.6 cy/mrad was selected, an appropriate choice of lens had to be made to avoid aliasing in the spatial frequency domain. Ideally, a detector cutoff frequency double that of the lens would completely eliminate this unwanted aliasing, but such a lens was not available for this study. The f/22 aperture setting on our lens was selected, resulting in an optical cutoff frequency of 6.2 cy/mrad. Choosing a large f/# allowed us to approach an absence of aliasing, but this also minimized the aperture size and limited the largest scattering angle that could enter the imaging system.

2.5 Results of Closure Experiment

In this section the results of the cloud chamber imaging experiment are presented. Measurements of the aerosol size distribution are shown, as are LSF and MTF curves calculated from control and through-aerosol measured imagery. Theoretical predictions of the aerosol MTF are calculated from measured aerosol particle size distribution calculations, and comparisons to experimentally-measured MTF curves are discussed.

2.5.1 Measurement of Cloud Aerosol Size Distributions

The MTU cloud chamber was used to generate expansion clouds as well as mixing clouds, and of the two, the mixing cloud was observed to have the smallest optical depth. Since maximum aerosol influence is desired, expansion clouds were the focus of subsequent experimentation. We note that expansion clouds have very little turbulence, and thereby avoid additional optical blurring from non-aerosol sources. Phase-Doppler measurements of cloud particles were recorded and, for comparison to idealized distributions often used in optical propagation calculations, measured size distributions were compared to four theoretical fog models (Shettle and Fenn, 1979). Figure 2.6 shows measured cloud droplet size distributions for a representative expansion cloud and mixing cloud (for the sake of comparison), along with the parametric fog models. These measured distributions illustrate that the cloud chamber can be tuned to produce clouds of varying droplet number density and modal size. Note that number concentration measurements of droplets with a radius below approximately 3 μm are not reliable due to system noise at small particle sizes, so the leading tail of measured cloud distributions is not reliable. Usually the points are discarded, but we show them for completeness. However, the larger aerosol sizes dominate the scattering effects so the small droplet measurement uncertainty is of small consequence. To prove this, Mie theory calculations were performed for the expansion cloud distribution, both as measured and without the first few (dubious) small-radius data points. The results were nearly identical; the exclusion of the smaller droplets reduced the scattering coefficient k_{sca} and optical depth τ by only 0.5%.

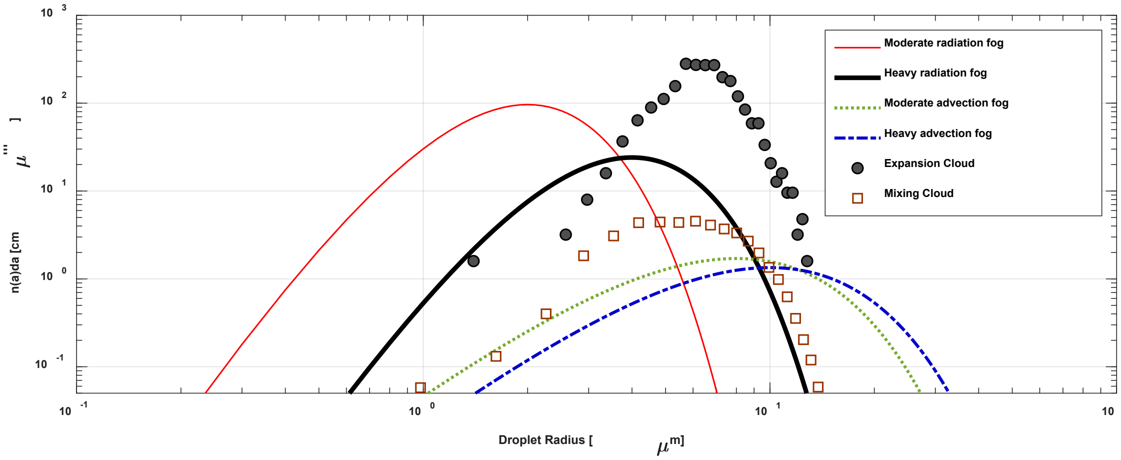

Figure 2.6. Measured expansion cloud and mixing cloud droplet size distributions shown along with four theoretical fog model distributions. Note that the range of measured droplet radii is comparable to theoretical models, but measured number concentrations in the expansion cloud are significantly higher (peak of 450 $\text{cm}^{-3}\mu\text{m}^{-1}$ vs 25 $\text{cm}^{-3}\mu\text{m}^{-1}$ for heavy radiation fog model). This results in a much larger optical depth, τ over the short propagation distance of the chamber. Mixing cloud data supplied by Kamal Chandrakar (MTU).

Using Mie theory (Ishimaru, 1997; Bohren and Huffman, 2004) the scattering cross section $\sigma_{sca}(\lambda,r)$ can be computed as a function of particle radius, r for the central wavelength of 550 nm in the visible spectrum. Combining these radius-dependent scattering cross sections (which scale as the radius squared, emphasizing larger droplets) with the measured droplet distribution functions yields scattering coefficients k_{sca} for each expansion cloud. The known 2 meter propagation distance across the chamber is then used to convert scattering coefficients into optical depths, τ. Optical properties calculated from the measured expansion clouds are listed in Table 2-1.

Table 2-1. Optical Properties Calculated from Measured Aerosol Particle Size Distributions

	Size Distribution Parameters				
Cloud Measurement	a_{mode} **[µm]**	a_{mean} **[µm]**	a_{eff} **[µm]**	k_{sca} **[km^{-1}]**	τ
Expansion Cloud #2	7.8	7.9	8.8	513	1.03
Expansion Cloud #3	6.2	7.4	8.4	393	0.79
Expansion Cloud #4	5.7	6.7	7.4	291	0.58

Note that in Table 2-1, three separate droplet radius values are listed. The first, a_{mode}, refers to the most numerous particle radius (or dominant radius) as found by the Phase Doppler histograms. This parameter is present in the aerosol PSF and MTF expressions described earlier. The measured expansion cloud particle distribution shown in Figure 2.6 is slightly less smooth than that of the mixing cloud. This is a consequence of the shorter duration (lifetime) of expansion clouds, which can prevent their measured size distributions from stabilizing into perfectly smooth histograms. Additionally, the expansion cloud distributions exhibited a small plateau (flat region) near their peak, suggesting a few consecutive radius values with similar number density. Due to the uncertainty in the dominant particle radii calculated from the expansion clouds and the importance of this parameter, additional droplet radii values were calculated. These included the mean droplet radius (a_{mean}) and effective droplet radius (a_{eff}), whose values are also listed in Table 2-1. These are two variations of radii-weighted averages often used to more completely describe measured droplet distributions (Miles et al., 2000). Assuming a droplet size distribution is characterized via histogram with a specified number of bins (N_{bins}), uniform bin width (Δa) and total droplet observations (N_t), the mean droplet radius (a_{mean}) is given by the expression

$$a_{mean} = \frac{1}{N_t} \sum_{i=1}^{N_{bins}} a_i \, n_{obs}(a_i) \, \Delta a \tag{16}$$

The effective droplet radius (a_{eff}) is similarly calculated from a droplet size distribution as

$$a_{eff} = \frac{\sum_{i=1}^{N_{bins}} a_i^3 \, n_{obs}(a_i)}{\sum_{i=1}^{N_{bins}} a_i^2 \, n_{obs}(a_i)} \tag{17}$$

Both of these methods produced values greater than the simple histogram maximum, due to the positive skewness of the measured size distributions.

2.5.2 Calculating the Control Modulation Transfer Function

To ensure the accuracy of the knife edge MTF calculation method, control images (lacking the presence of cloud aerosols) were captured through the empty cloud chamber. The LSF was computed as the horizontal spatial gradient of the edge response across the sharp black-white transition, as in equation (14). Next, a Fast Fourier Transform (FFT) operation was performed on the LSF to compute the control MTF. This imaging system MTF incorporates both aperture diffraction and detector pixel footprint artifacts, but the f/22 lens setting was chosen to ensure a diffraction-limited scenario. The measured MTF was expected to be dominated by the aperture diffraction shape suggested by equation (11), and it was, but another effect was evident as well. The measured control MTF rolled off at a lower spatial frequency than the ideal, theoretical diffraction-limited equation predicts. An investigation into this revealed the issue to be the limited dynamic range of the camera detector.

During this control MTF investigation, an ideal theoretical diffraction-limited MTF was applied to a pristine, digital knife edge pattern with the same resolution as the actual monochromatic imager. The edge response was taken from the resulting blurred knife edge, and a horizontal gradient was applied digitally to calculate a floating point LSF. This ideal digital LSF was normalized to a peak of 1, then quantized to 12, 13 and 14 bits. Subsequently, a zero-padded FFT operation was performed on both the floating point and quantized LSFs to compute a family of MTF curves. This was done for two reasons: to ensure that the FFT of the floating point LSF would reproduce an ideal diffraction-limited MTF, and to determine the impact of quantization on measured MTFs. The result of this investigation is shown in Figure 2.7.

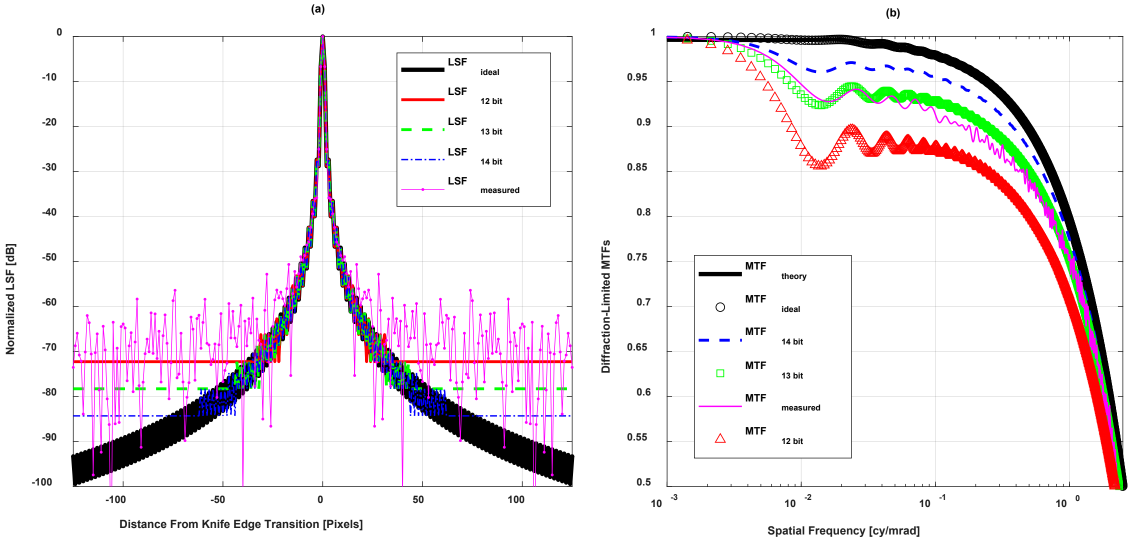

Figure 2.7. (a) Diffraction-limited LSF comparison between ideal (floating point) and quantized to simulate various finite bit-depth detectors. (b) Family of MTF curves computed from the diffraction-limited LSFs shown in (a).

Panel (a) of Figure 2.7 shows the various LSF curves, with the dynamic range plateaus of each quantized curve evident. The maximum dynamic range of an analog-to-digital converter (ADC) with Q bits is less than $20\log_{10}(2^Q)$ decibels because of its noise floor (Seeber, 1998). The optical sensor used to measure the knife edge uses a 14-bit ADC with a reported dynamic range between 68 and 70 dB depending on imaging mode, but its 16-bit images were shown to have only 2^{12} unique integer values. The dynamic range limit of the detector can be seen when the measured LSF is compared to the simulated quantized LSFs.

Panel (b) shows the MTF curves computed via FFT from the LSF curves, and two observations are noted here. First, the floating point LSF does in fact return a diffraction-limited MTF almost indistinguishable from the original, theoretical control MTF. This demonstrates the ability to apply an ideal MTF and then re-calculate it from imagery using the line spread function method. Second, the 13-bit quantization almost exactly reproduces the measured control MTF, which is interesting given the apparent 12-bit nature of the images digitized by a 14-bit ADC. The relevance of this quantization for optical blurring due to aerosols will be considered in the next section.

2.5.3 Aerosol Point Spread Function Analysis

Prior to calculating experimental aerosol MTF curves and comparing them to theoretical predictions made from measured boundary conditions, we begin with an analysis of the expected aerosol PSF after detector quantization. As described in equation (3), the aerosol PSF is a combination of direct and indirect (scattered) light. The wavelength-dependent aerosol parameters necessary for predicting its shape, which include optical depth, scattering coefficient, modal particle radius and (total) single scattering albedo are calculated from the Phase-Doppler particle size distribution measurements. The imaging system parameters (i.e., aperture diameter and focal length) are also important inputs as they can significantly impact the distribution of light on the detector. Additionally, as was shown in Figure 2.7, the quantization and dynamic range limitations of the detector must be incorporated.

To demonstrate this, we calculate the expected PSF of the imaging system in the presence of expansion cloud droplets in the cloud chamber for a 2-meter propagation path. A dominant particle radius of 8 μm is selected as representative of the droplet distributions described in Table 2-1, and an optical depth of 0.75 is chosen as an intermediate thickness of the measured expansion clouds. Both the direct (unscattered) and indirect (scattered) components of the PSF are computed and shown in panels (a) and (b) of Figure 2.8, respectively. Next they are summed and normalized; the results of this operation are shown in panel (c) along with a dashed line indicating the dynamic range threshold of a simulated 13-bit detector.

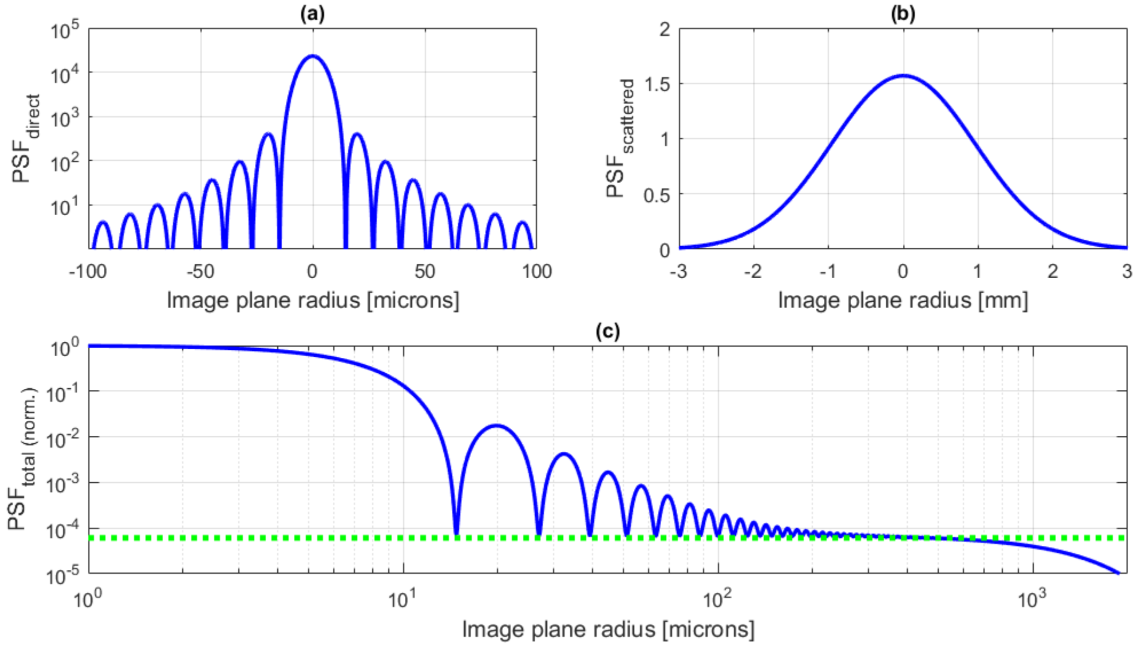

Figure 2.8. (a) Direct, unscattered component of PSF whose shape is the familiar diffraction-limited Bessel function. (b) Indirect, scattered component of PSF which takes the form of a decaying exponential. (c) Normalized combination of direct and scattered components for a dominant droplet radius of 8μm and optical depth of 0.75, with the equivalent of a 13-bit ADC noise floor shown for reference.

2.5.4 Predicted Aerosol Modulation Transfer Function

With an aerosol PSF measured for a representative expansion cloud, predictions for the expected shape of the aerosol MTF can be made. Using the analytic MTF expression given in equation (10), which was developed from Ishimaru's published aerosol PSF (Ishimaru, 1997), a theoretical spatial frequency response can be computed for expansion cloud conditions. This is done with two separate methods, the first of which is a direct calculation using the analytical aerosol MTF expression.

The second method obtains aerosol MTF responses from a 2D Fourier Transform of the sampled aerosol PSFs. Care was taken to ensure that this operation yields the ideal theoretical MTF when the unquantized PSF is used instead of the detector ADC-limited version. Once the accuracy of this method was established, both the ideally-sampled and quantized aerosol PSFs were converted to the spatial frequency domain via FFT operations. These two total MTF responses (ideal and quantized), which include both aerosol and imaging system effects, are compared in Figure 2.9. We note the strong influence that the dynamic range limitations of the detector is expected to have on measured MTF curves.

Panel (a) of Figure 2.9 shows the attenuated, direct component of the MTF which falls off as the optical cutoff frequency is approached and differs from the diffraction-limited case only because of the chamber's non-zero optical depth. Panel (b) shows the predicted scattering component; the aerosol-driven exponential decay occurs at very low spatial frequencies and is sensitive to the dominant radius of the aerosol distribution. Panel (c) of Figure 2.9 compares the two predicted (total) MTF curves, the ideal (solid line) and the quantized (dotted line).

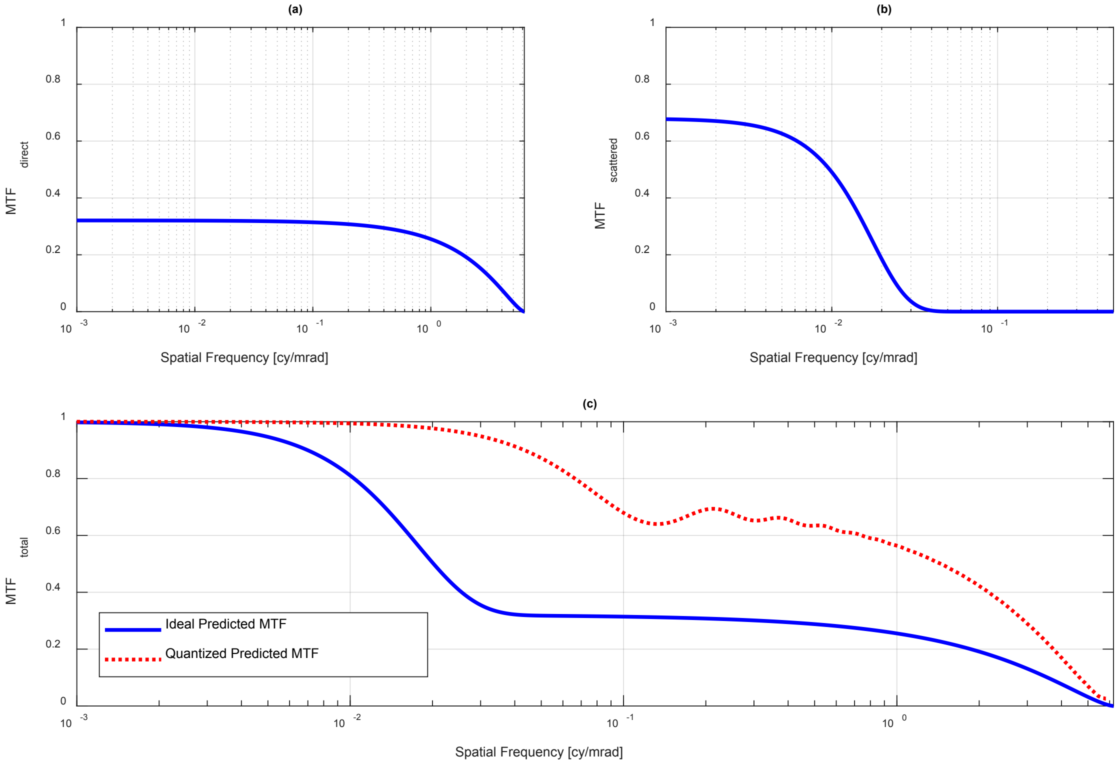

Figure 2.9. (a) Direct component of the aerosol MTF, which is an attenuated version of the diffraction-limited $\cos^{-1}$ function. (b) Indirect, scattered component of the aerosol MTF. (c) Ideal and 13-bit quantized versions of the total aerosol MTF for a dominant droplet radius of 8μm and optical depth of 0.75.

To investigate the sensitivity of the resultant MTF shape to the bit-depth of a detector, several dynamic ranges were used to quantize the aerosol PSF before conversion to the spatial frequency domain. In addition to the previously shown 13-bit quantization, 12-bit and 16-bit were computed and compared to the ideal (unquantized) MTF expected based on scattering theory. This aerosol MTF comparison is shown in Figure 2.10. It was noted that with a 16-bit detector, the expected theoretical MTF shape is almost completely recovered. Conversely, the impact of a 12-bit quantization was to modify the aerosol MTF until it closely resembled an aperture diffraction-limited response with almost no aerosol effects evident.

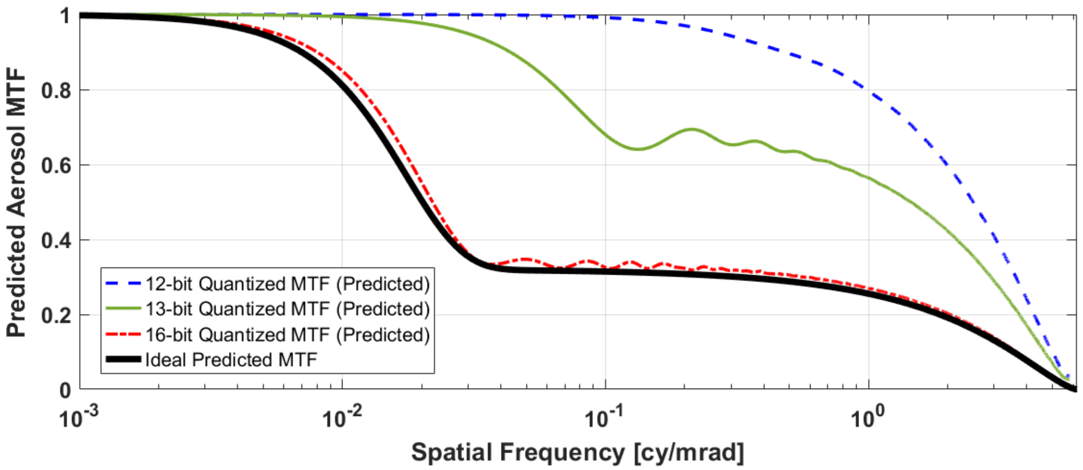

Figure 2.10. Ideal aerosol MTF, predicted from theory, is compared to several dynamic range-limited simulations of various bit-depth detectors.

The sensitivity of the (quantized) aerosol MTF response to the primary parameters used to describe the droplet distribution, namely dominant radius and optical depth, was also explored. This was done by first holding the dominant droplet radius constant and varying the optical depth, with no concern for the underlying changes in the particle distribution that would be necessary to make this combination of values physically occur. Next, a constant optical depth was assumed and various values of dominant droplet radius were used as inputs to the theoretical expressions. The results of this parametric sensitivity study are shown in Figure 2.11.

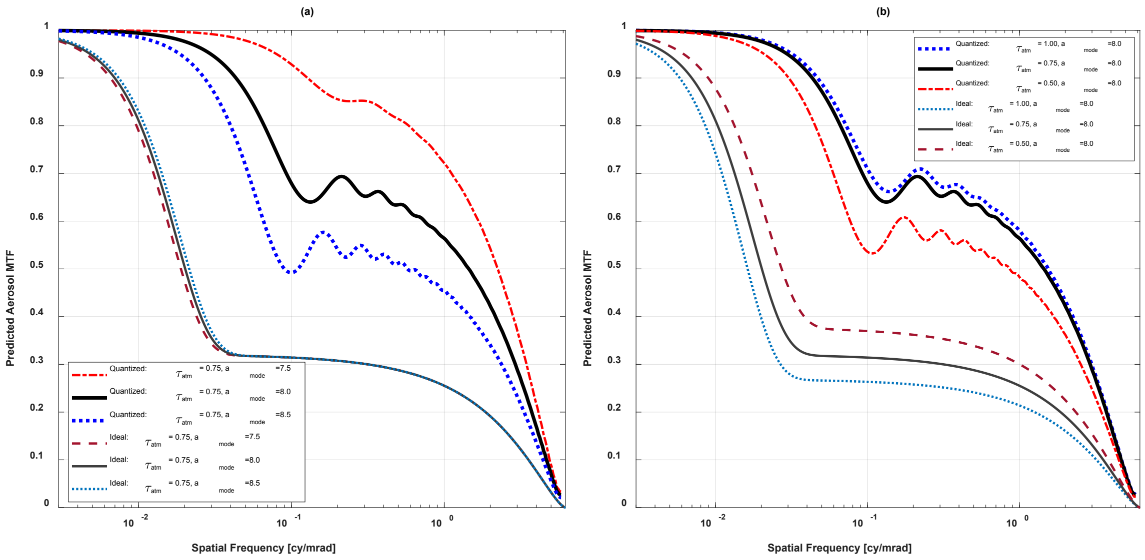

Figure 2.11. (a) Impact of varying dominant droplet radius on [quantized] aerosol MTF, assuming constant optical depth. (b) Variations in [quantized] aerosol MTF due to various optical depths, assuming the same dominant droplet radius.

In the case of varying primary droplet radius, shown in panel (a) of Figure 2.11, the ideal responses show little change but the quantized curves are significantly impacted. Additionally, the order of the curves is reversed after dynamic range limitations are imposed. When the optical depth is varied as shown in panel (b), the order of the curves is again reversed, and both the ideal and quantized MTF responses are affected by changes in optical depth τ.

2.5.5 Measured Aerosol Modulation Transfer Function

System-level aerosol MTF curves were calculated from imagery captured through expansion clouds created in the MTU cloud chamber. The process to obtain this measured aerosol MTF was the same as described in Section 2.5.2, where an LSF was computed by differentiating the horizontal ESF. Since the black side of the knife-edge was less noisy, that portion was used to create a symmetric LSF about its maximum. A normalized version of this symmetric LSF measured during Expansion Cloud #3 is shown in panel (a) of Figure 2.12. The measured aerosol MTF is obtained by performing an FFT operation on the measured LSF. The resulting MTF, shown in panel (b) of Figure 2.12, incorporates all imaging system effects including those beyond ideal aperture diffraction and detector limitations. Additionally, the measured MTF responses for Expansion Cloud #2 and #4 are shown for comparison in panel (b); the three measured LSF curves were similar enough that only Expansion Cloud #3 was shown in panel (a) for the sake of clarity.

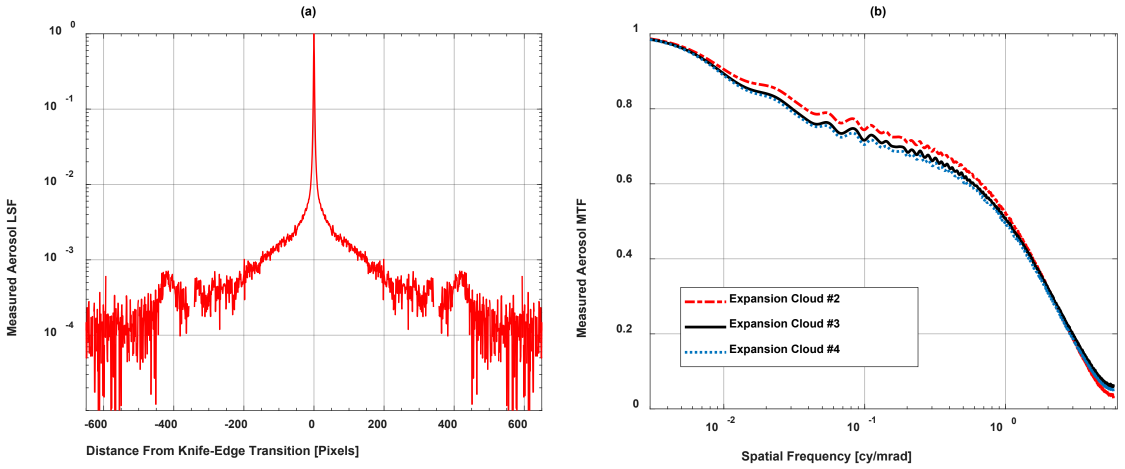

Figure 2.12. (a) Normalized line spread function measured during Expansion Cloud #3 on March 17, 2017 through the MTU cloud chamber. (b) Measured aerosol MTFs obtained from imagery captured through expansion clouds.

With a measured aerosol MTF calculated from imagery captured through the cloud chamber in the presence of an expansion cloud, a comparison can be made to the predictions made in Section 2.5.4. Figure 2.13 combines the theoretical (quantized) aerosol MTFs from panel (a) of Figure 2.11 together with the measured aerosol MTF (Expansion Cloud #3 from Figure 2.12) on the same spatial frequency axis.

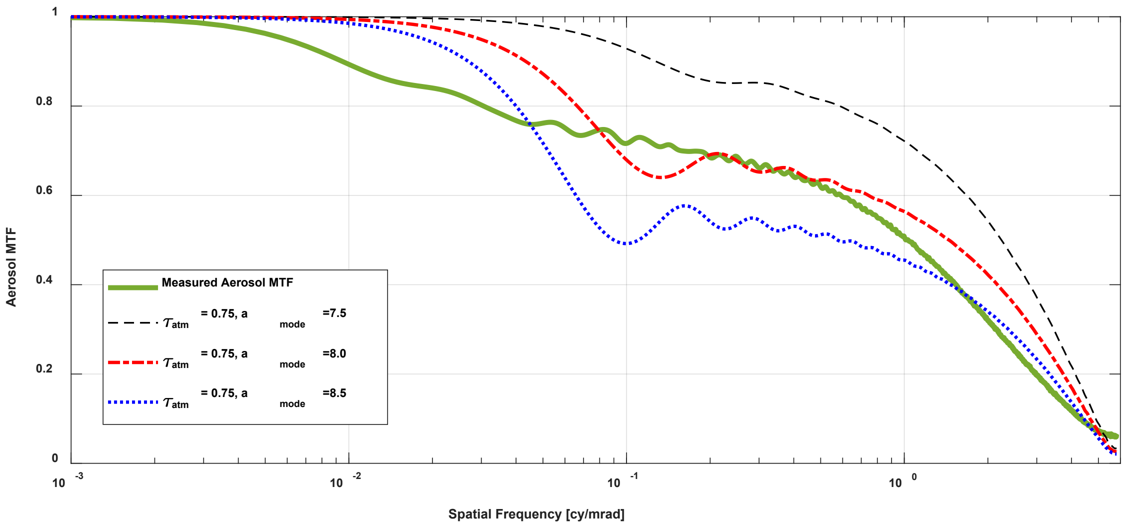

Figure 2.13. Measured and predicted aerosol MTFs shown together for comparison.

Given the sensitivity of the quantized theoretical expressions to the selected dominant droplet radius and uncertainty in the measured particle mode, the 8µm-radius prediction matches the measured aerosol MTF quite well. The 7.5µm and 8.5µm bit-depth limited, analytically-predicted curves bound the chamber measurement for spatial frequencies greater than $3x10^{-2}$ cycles per milliradian (see Figure 2.13). Due to the detector resolution, pixel pitch and the focal length of the optics, spatial frequencies below this value cannot be accurately measured due to the width of such a cycle. In the spatial frequency range that can be reliably measured by the cloud chamber imaging system, the predicted aerosol MTF compares reasonably well to the measured response once the optical sensor limitations and droplet radius (listed in Table 2-1) are considered. The more gradual decrease in MTF with increasing spatial frequency in the measurements relative to the theory seems likely to be a result of the width of the droplet size distribution. The theoretical curves correspond to a modal radius value, whereas the actual cloud has a broad range of droplet sizes.

2.6 Summary and Discussion

Aerosol scattering is thought to contribute to the blurring and contrast reduction found in measured optical images. Here we showed that a theoretical modulation transfer function can be computed which includes atmospheric attenuation, small-angle aerosol scattering (i.e., near-forward scattering of light by particles large compared to the wavelength) and diffraction effects. This aerosol MTF, assuming an aperture diffraction-limited case, is composed of two primary components. The first is a pedestal created by an attenuated version of the diffraction MTF whose peak magnitude depends on optical depth. As optical depth increases, the pedestal or base of the aerosol MTF (upon which the scattered component is essentially added) is lowered. The second aerosol MTF component is a decaying exponential located at small spatial frequencies, created by scattered light spread over a portion of the image plane. The spatial frequency at which this indirect light ceases to contribute in a significant way is sensitive to aerosol modal radius. As the dominant droplet size increases, the spatial frequency extent of the decaying exponential increases. These two components comprise the total MTF, which includes both aerosol and imaging system artifacts.

The significance of blurring due to aerosol scattering is not agreed upon in the literature, and several conflicting theoretical models for predicting the impact of small-angle scattering exist. Various PSF models which incorporate aerosol scattering have been proposed, based either on theoretical solutions or analysis of measured data. Additionally, several authors have proposed spatial frequency domain descriptions of blurring due to small-angle aerosol scattering. This apparent controversy appears to focus on the severity of the phenomenon and shortcomings of aerosol experiments (Bissonnette, 1992; McDonald et al., 1992; Bruscaglioni et al., 1993; D. Sadot and Kopeika, 1993; Dan Sadot and Kopeika, 1993; Dror and Kopeika, 1995; Kopeika and Sadot, 1995; Ben Dor et al., 1997; Kopeika, 1997; Kopeika et al., 1998; Eismann and LeMaster, 2013). There are relatively few published measurements of the impact of aerosol scattering, and they tend to focus on specific aspects of the full problem. Most significantly, detailed comparisons between theory and measurements are challenging because characterization of conditions in the atmosphere is challenging, and uncertain assumptions must be made regarding spatial and temporal uniformity (i.e., statistical homogeneity or stationarity).

After detailing theoretical PSF and MTF expressions to predict the impact of aerosol scattering on measured imagery, we proposed and showed the results from a closure experiment using the MTU cloud chamber. Our methodology involved capturing knife-edge imagery through a controlled expansion cloud while also directly measuring its particle size distribution. Experimental aerosol MTFs were obtained from these images and compared to theoretical predictions made using measured atmospheric conditions calculated from particle size distribution histograms. Predicted MTF responses for both the control and aerosol scenarios were made with and without finite bit-depth detector limitations, and the impact of quantization and noise floor was illustrated. These predicted aerosol MTF curves, created with atmospheric properties based on measured expansion cloud distributions, were compared to MTF responses measured in the cloud chamber.

According to analysis of MTF measurements performed in numerous laboratories (Williams and Becklund, 2010), measuring a modulation transfer function to within 5% of a theoretically-predicted curve demonstrates sufficient accuracy. The measured control MTF response (prior to quantization), obtained with a manual focus procedure, was within 7% of the diffraction-limited MTF that would be expected under ideal conditions including perfect focus, absence of lens aberrations, uniform knife-edge illumination, etc. After quantization was applied to incorporate finite bit-depth detector limitations, the theoretical control MTFs closely resembled the measured control MTF. The theoretical control MTF with simulated 13-bit quantization was an almost exact match when compared to the measured control MTF.

The (ideal) predicted aerosol MTFs showed only a slight sensitivity to small variations in dominant droplet radius, with moderate MTF response changes due to various optical depths. However, bit-depth quantizations of the ideal aerosol MTFs displayed high sensitivity to changes in droplet radius. In contrast, the ideal and quantized aerosol MTFs responded similarly to changes in optical depth. Our investigation revealed that the MTF response modifications depended on how far from the centroid of the PSF the dynamic range cutoff occurred and how much PSF energy was contained in the portion below the detector noise floor. Other things being equal, moving the noise floor cutoff closer to the PSF center increased the difference between the ideal and quantized MTF. Loss of all but the Bessel function near the PSF centroid means the resulting MTF is essentially the diffraction-limited control case, which is sensible given that the indirect (scattered) light is spread over the image plane (not well focused). Removing this scattered contribution diminishes the discrepancy between aerosol and control MTF. This means that with the expansion cloud conditions present in the chamber, aerosol scattering is an evident but subtle contributing effect (Eismann and LeMaster, 2013) that is significantly impacted by the optical imaging system used to measure it. In an atmospheric context, the significance of aerosol-induced blurring would depend not only on the details of the aerosols and propagation path length but also on the hardware configuration of the imaging system, especially the dynamic range of its detector.

The (quantized) predicted MTFs matched the measured aerosol curves reasonably well, disagreeing by less than 10% for a single combination of droplet radius and optical depth. Due to the sensitivity to the droplet radius selected for the predicted curves, and the uncertainty of the exact dominant droplet radius for each of the three expansion clouds, this amount of prediction error is encouraging. Theoretical aerosol MTFs computed from a small range of droplet radii based on values in Table 2-1 easily bound the measured MTFs everywhere but below $3\text{x}10^{-2}$ cycles per milliradian, which is approximately the limit of reliable information from the detector footprint used for image capture. The authors believe that the theoretical expressions, which utilize a single, modal particle radius, are likely most accurate for nearly-monodisperse particle distributions. For strongly polydisperse distributions such as our expansion clouds, which were measured to have a broad distribution of droplet radii with similarly-dominant number densities, the choice of a single radius is apparently insufficient when sensitivity to this value is considered. This further explains why the various measured aerosol MTFs were similar; the particle distributions of the generated expansion clouds largely overlapped and often had several strongly-contributing adjacent radius bins.

Overall, the concept of closure between MTFs obtained from directly-measured images and MTFs calculated from theory using measured cloud properties in a laboratory setting, has been demonstrated to be achievable and quantitatively successful. The comparison led to several findings: the theoretical expression for MTF is likely overly simplistic and does not account for broad particle size distributions; the relevance of optical blurring from light scattering by aerosol particles depends sensitively on the properties of both the particles and the imaging system; regarding the latter, the digital dynamic range was found to be especially relevant, having the ability to reveal or mask aerosol blurring effects for realistic bit levels.

In future experiments we intend to explore a wider range of cloud conditions, especially at larger values of optical depth, and for a broader range of particle sizes. Further, the thermal convection capability of the cloud chamber will enable exploration of the influence of turbulence, simultaneously with particles, thereby testing the common assumption of independence and additivity. On the instrumentation side, we aim to explore the influence of camera digital dynamic range. A higher bit depth detector would lead to a lower noise floor, and a larger detector cutoff frequency would allow the imaging aperture to be enlarged without additional aliasing. This would potentially allow a wider range of scattering angles to impact the aerosol measurements.

3 Monte Carlo Scattering Simulation: *mcScatter*

A Monte Carlo scattering simulation was created in Matlab (a MathWorks product), for the purpose of performing experimental interactions between light and cloud distributions *virtually*. In a computer simulation, some of the physical constraints of an actual cloud chamber (such as physical size, maximum optical depth, particle clustering, instrumentation type and location) can be removed to determine what would happen if such an experiment were performed. The following sections in this chapter detail the construction of this scattering simulation, referred to as 'mcScatter'. The various user inputs, modes of operation and result outputs are described.

3.1 Overview of the *mcScatter* Graphical User Interface (GUI)

A graphical user interface (GUI) was created for the *mcScatter* simulation. The application's GUI allows users to provide a variety of inputs, including:

- size of the virtual volume
- number density, size (radius) and spatial distribution of the particles
- initial photon ray positioning method and scattering phase functions
- volume "wall" boundary conditions and subvolume resolution
- optical wavelength, refractive index of air and scattering media

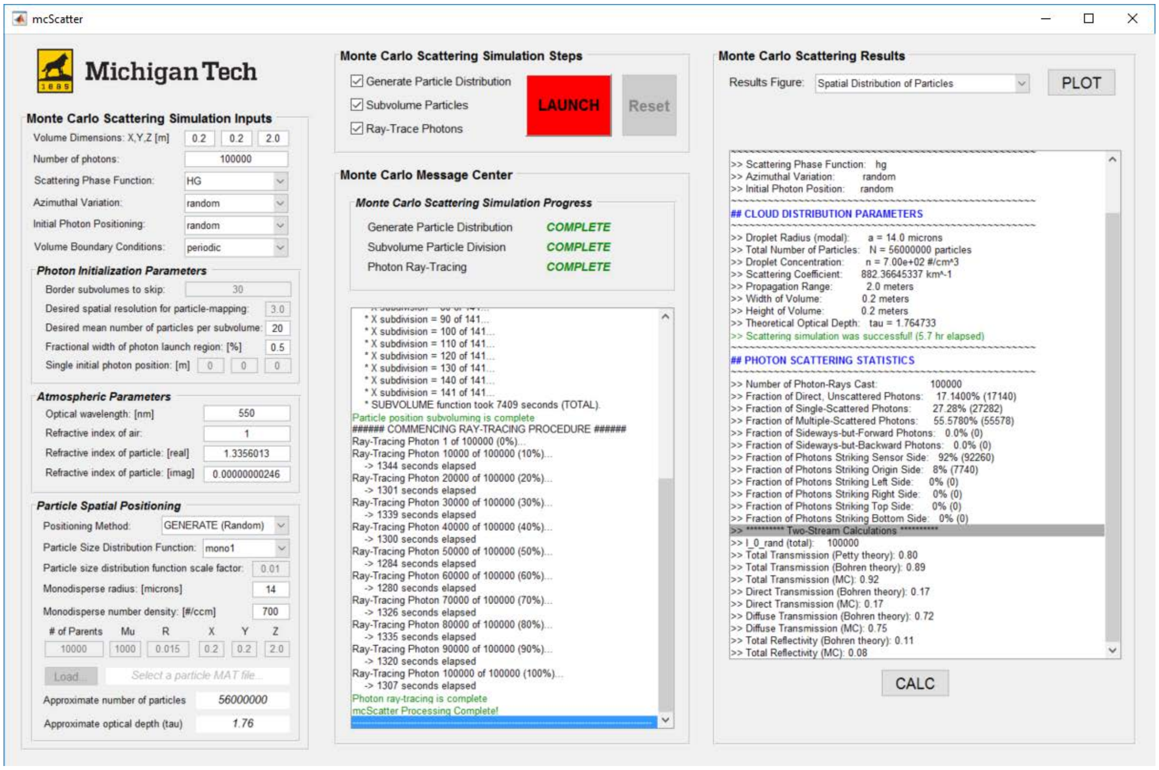

Monte Carlo Scattering Simulation Inputs

Volume Dimensions: X,Y,Z [m] 0.2 0.2 2.0
Number of photons: 100000
Scattering Phase Function: HG
Azimuthal Variation: random
Initial Photon Positioning: random
Volume Boundary Conditions: periodic

Photon Initialization Parameters

Border subvolumes to skip: 30
Desired spatial resolution for particle-mapping: 3.0
Desired mean number of particles per subvolume: 20
Fractional width of photon launch region: [%] 0.5
Single initial photon position: [m] 0 0 0

Atmospheric Parameters

Optical wavelength: [nm] 550
Refractive index of air: 1
Refractive index of particle: [real] 1.3356013
Refractive index of particle: [imag] 0.00000000246

Particle Spatial Positioning

Positioning Method: GENERATE (Random)
Particle Size Distribution Function: mono1
Particle size distribution function scale factor: 0.01
Monodisperse radius: [microns] 14
Monodisperse number density: [#/ccm] 700

# of Parents	Mu	R	X	Y	Z
10000	1000	0.015	0.2	0.2	2.0

Select a particle MAT file...
Approximate number of particles *56000000*
Approximate optical depth (tau) *1.76*

Monte Carlo Scattering Simulation Steps

☑ Generate Particle Distribution
☑ Subvolume Particles
☑ Ray-Trace Photons

Monte Carlo Message Center

Monte Carlo Scattering Simulation Progress

Generate Particle Distribution *COMPLETE*
Subvolume Particle Division *COMPLETE*
Photon Ray-Tracing *COMPLETE*

```
   * X subdivision = 90 of 141...
   * X subdivision = 100 of 141...
   * X subdivision = 110 of 141...
   * X subdivision = 120 of 141...
   * X subdivision = 130 of 141...
   * X subdivision = 140 of 141...
   * X subdivision = 141 of 141...
   * SUBVOLUME function took 7409 seconds (TOTAL).
Particle position subvoluming is complete
###### COMMENCING RAY-TRACING PROCEDURE ######
Ray-Tracing Photon 1 of 100000 (0%)...
Ray-Tracing Photon 10000 of 100000 (10%)...
   -> 1344 seconds elapsed
Ray-Tracing Photon 20000 of 100000 (20%)...
   -> 1301 seconds elapsed
Ray-Tracing Photon 30000 of 100000 (30%)...
   -> 1339 seconds elapsed
Ray-Tracing Photon 40000 of 100000 (40%)...
   -> 1300 seconds elapsed
Ray-Tracing Photon 50000 of 100000 (50%)...
   -> 1284 seconds elapsed
Ray-Tracing Photon 60000 of 100000 (60%)...
   -> 1280 seconds elapsed
Ray-Tracing Photon 70000 of 100000 (70%)...
   -> 1326 seconds elapsed
Ray-Tracing Photon 80000 of 100000 (80%)...
   -> 1335 seconds elapsed
Ray-Tracing Photon 90000 of 100000 (90%)...
   -> 1320 seconds elapsed
Ray-Tracing Photon 100000 of 100000 (100%)...
   -> 1307 seconds elapsed
Photon ray-tracing is complete
mcScatter Processing Complete!
```

Monte Carlo Scattering Results

Results Figure: Spatial Distribution of Particles

```
>> Scattering Phase Function:   hg
>> Azimuthal Variation:         random
>> Initial Photon Position:     random
~~~~~~~~~~~~~~~~~~~~~~~~~~~~~~~~~~~~~~~~~~~~~~~~~~~~~~~~~~~~~~~
## CLOUD DISTRIBUTION PARAMETERS
~~~~~~~~~~~~~~~~~~~~~~~~~~~~~~~~~~~~~~~~~~~~~~~~~~~~~~~~~~~~~~~
>> Droplet Radius (modal):      a = 14.0 microns
>> Total Number of Particles:   N = 56000000 particles
>> Droplet Concentration:       n = 7.00e+02 #/cm^3
>> Scattering Coefficient:      882.36645337 km^-1
>> Propagation Range:           2.0 meters
>> Width of Volume:             0.2 meters
>> Height of Volume:            0.2 meters
>> Theoretical Optical Depth:   tau = 1.764733
>> Scattering simulation was successful! (5.7 hr elapsed)
~~~~~~~~~~~~~~~~~~~~~~~~~~~~~~~~~~~~~~~~~~~~~~~~~~~~~~~~~~~~~~~
## PHOTON SCATTERING STATISTICS
~~~~~~~~~~~~~~~~~~~~~~~~~~~~~~~~~~~~~~~~~~~~~~~~~~~~~~~~~~~~~~~
>> Number of Photon-Rays Cast:                  100000
>> Fraction of Direct, Unscattered Photons:     17.1400% (17140)
>> Fraction of Single-Scattered Photons:        27.28% (27282)
>> Fraction of Multiple-Scattered Photons:      55.5780% (55578)
>> Fraction of Sideways-but-Forward Photons:    0.0% (0)
>> Fraction of Sideways-but-Backward Photons:   0.0% (0)
>> Fraction of Photons Striking Sensor Side:    92% (92260)
>> Fraction of Photons Striking Origin Side:    8% (7740)
>> Fraction of Photons Striking Left Side:      0% (0)
>> Fraction of Photons Striking Right Side:     0% (0)
>> Fraction of Photons Striking Top Side:       0% (0)
>> Fraction of Photons Striking Bottom Side:    0% (0)
>> ********** Two-Stream Calculations **********
>> I_0_rand (total):    100000
>> Total Transmission (Petty theory): 0.80
>> Total Transmission (Bohren theory): 0.89
>> Total Transmission (MC): 0.92
>> Direct Transmission (Bohren theory): 0.17
>> Direct Transmission (MC): 0.17
>> Diffuse Transmission (Bohren theory): 0.72
>> Diffuse Transmission (MC): 0.75
>> Total Reflectivity (Bohren theory): 0.11
>> Total Reflectivity (MC): 0.08
```

Figure 3.1. Screenshot of 'mcScatter' application GUI

The *mcScatter* GUI allows users to define the scattering simulation inputs, control the methods used to initialize and propagate rays through the particle distribution, view statistics calculated from the simulation output and visualize relevant results. The following subsections will detail the algorithmic design of the scattering simulation.

3.2 Particle generation

3.2.1 Uniform randomly-distributed particle locations

The simplest 'cloud' that can be generated by the scattering simulation is a random monodisperse distribution. The user selects the desired number density and particle radius, and the required number of particles are inserted at uniformly-random locations within the user-specified spatial limits of the particle volume. A representative example of a monodisperse particle distribution, with approximately 1000 particles for illustration, is shown in Figure 3.2.

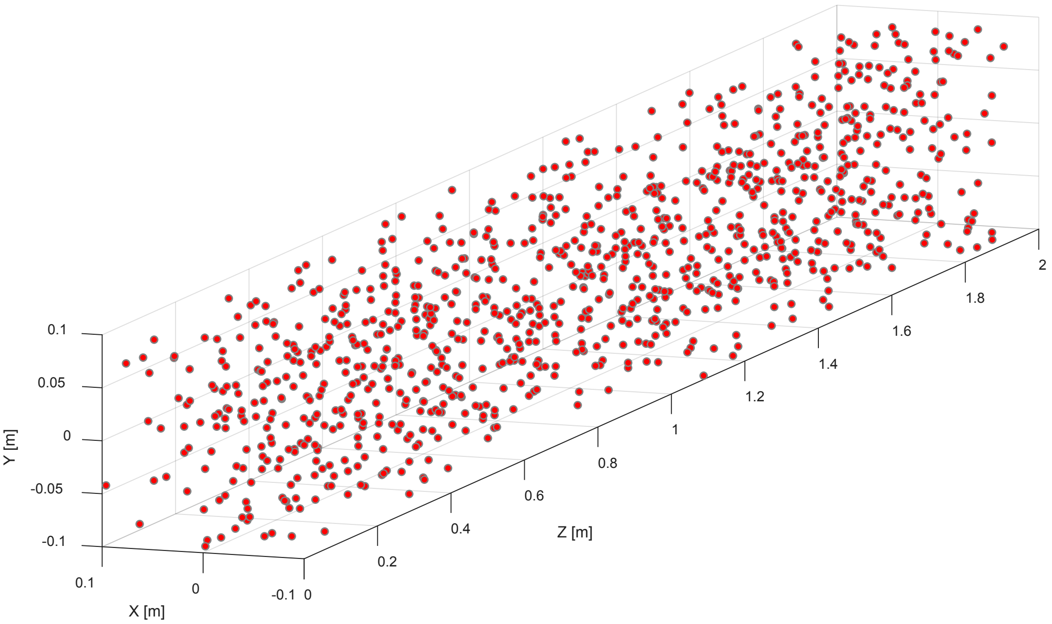

Figure 3.2. Representative example of uniformly-random monodisperse particle distribution.

For a more realistic 'cloud', a polydisperse particle distribution can be generated. A pre-programmed particle size distribution function (based on a smoothed version of a MTU cloud chamber-generated expansion cloud) is selected and scaled up or down. This scaling factor allows a realistic composition of different particle radii while varying the total number of particles (to change optical depth). As with the simple monodisperse distribution, the polydisperse particles are placed randomly throughout the volume. The pre-programmed polydisperse particle size distribution function ('cloud1') is plotted in Figure 3.3 and an example of the resultant particle distribution is shown in Figure 3.4.

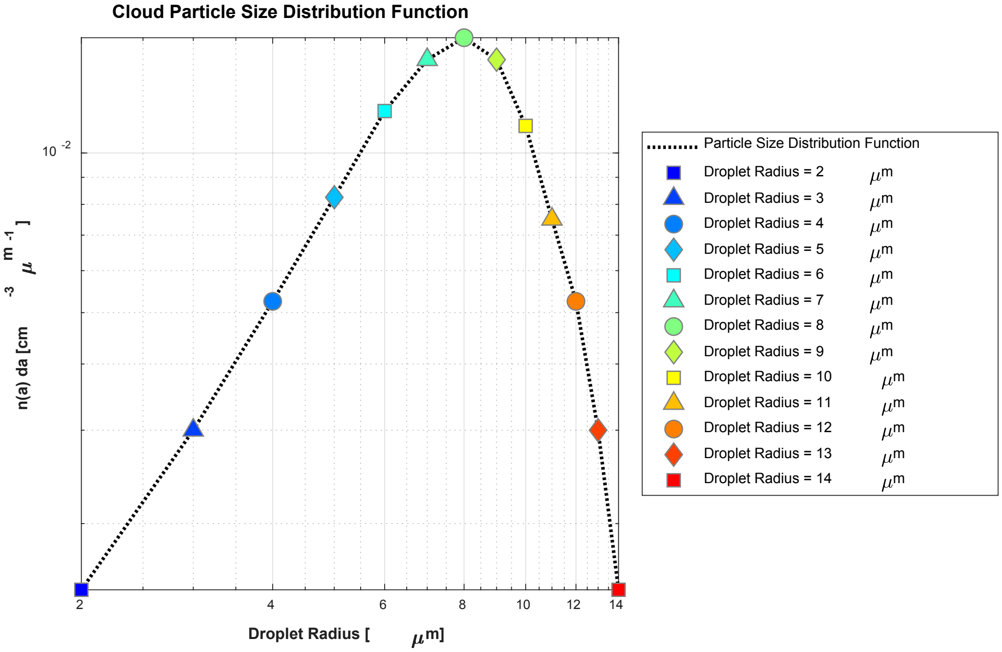

Figure 3.3. Particle size distribution function used for polydisperse media, referred to as "cloud1".

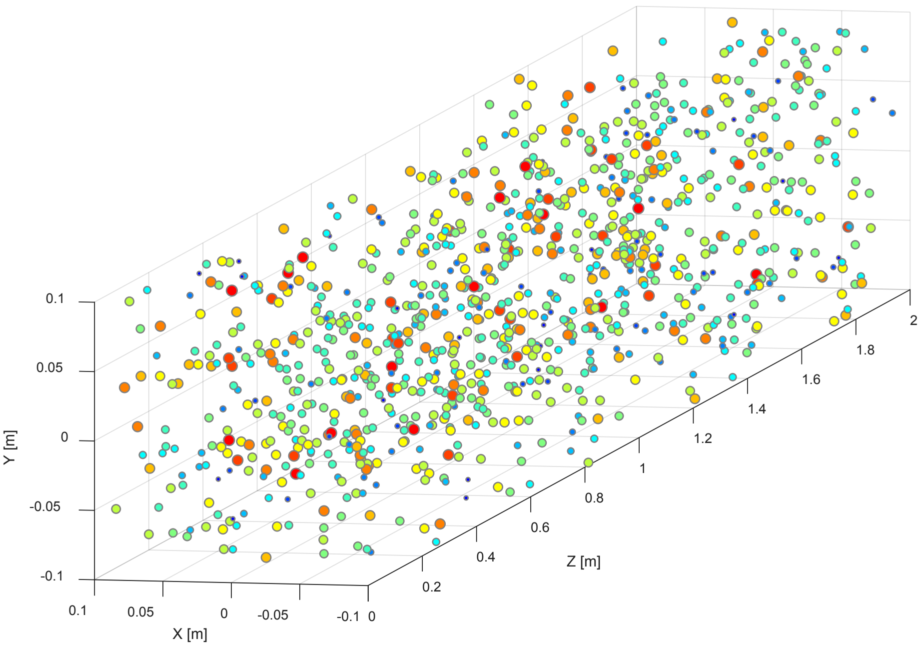

Figure 3.4. Representative example of a spatially-random polydisperse particle distribution, referred to as "cloud1".

Note that the symbol colors in Figure 3.3 correspond to various particle sizes; these same symbol colors are used in Figure 3.4 (along with symbol size) to indicate particle size.

3.2.2 Matérn spatial particle distributions

The scattering simulation can also generate non-uniform particle locations. In this mode, a Matérn-based algorithm places the desired number of (monodisperse) particles heterogeneously throughout the volume in clusters, or groups, of particles (see Figure 3.5). The user can specify the approximate number of clusters, average number of particles in each cluster, and the density or spread of the groups relative to the overall volume. This final input parameter controls how closely spaced the particles in each cluster are versus how much space separates one group from another. This allows the user to investigate the impact of particle clustering on light propagation through virtual cloud distributions.

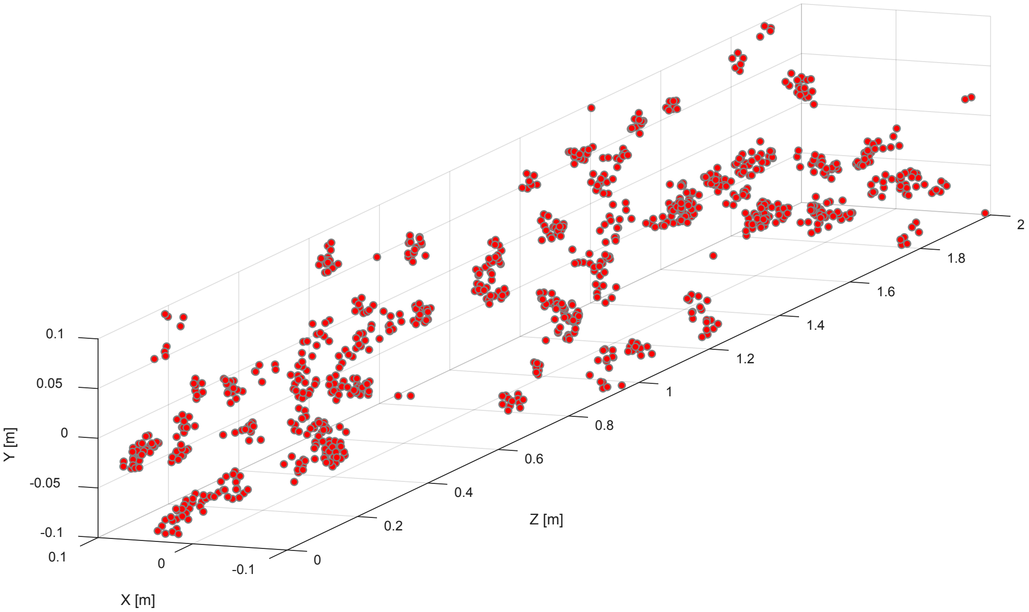

Figure 3.5. Representative example of Matérn-generated monodisperse particle distribution, where aerosols are clustered instead of randomly spaced throughout the volume.

3.3 Subvoluming particles in the scattering media

3.3.1 Binning particles into subvolumes

By its very nature, *mcScatter* simulates a scattering medium by ray-tracing photon paths through a volume containing numerous particles at specified (stationary) spatial locations. Intersections between these photon rays and particles create scattering events, and because mathematical tests are used to determine if ray-particle collisions occur, computational efficiency is important for minimizing simulation runtimes. Assuming a 0.08 m^2 volume, a cloud with a total optical depth (τ) of 1 would require 3.2×10^7 14µm-radius particles. Testing each ray against 32 million particles to see if one or more aerosols lie on the ray path would be an arduous task.

To ease this mathematical burden, a pre-processing step is performed where the cloud volume is divided into "subvolumes". Each subvolume will necessarily contain only a small portion of the total number of particles. As a photon ray travels through the volume, the subvolumes it intersects are checked one at a time for particle scattering events, and only the particles in each individual subvolumes are considered (Pharr and Humphreys, 2004). By increasing the number of subvolumes, the average number of particles in each subvolume can be reduced to a manageable amount (perhaps 20).

During the particle-binning process, illustrated in Figure 3.6, the scattering volume is divided into an equal number of subvolumes (Step 1, left). Next, particle centroids are used to determine the subset of particles assigned to each subvolume. Because a particle could have its centroid in one subvolume but its radius could extend it into an adjacent subvolume, 100µm margins are used to include particles centered in the immediate vicinity of each subvolume (Step 2, center). These margins, which consider particles that may be partially contained in a subvolume, mean that some particles are counted in more than one subvolume (Step 3, right). This ensures that scattering events are not missed.

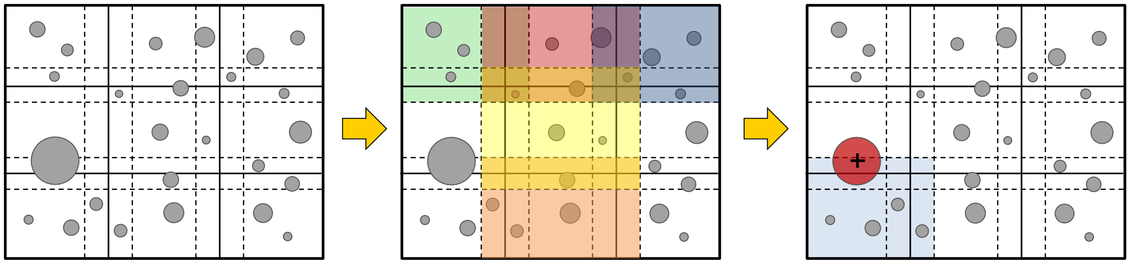

1. Divide particle distribution into "subvolumes" with margins

2. Apply boundaries to determine which particles belong to each subvolume

3. Multi-counted particles ensure collisions are not missed

Figure 3.6. Diagram showing how particles in the volume are grouped into subvolumes. Dashed lines indicate "margins" that allow some subvolumes to overlap, categorizing some boundary-crossing particles into multiple subvolumes to ensure collisions are not missed.

For example, consider a ray passing parallel but very near to a subvolume wall towards a particle which straddles two subvolumes. In this scenario, the ray may strike the edge of the particle even though its centroid is located in another subvolume. If only the centroid was used to determine which subvolume it belongs to, the collision would be missed. Employing subvolume margins (larger than the particle radius) ensures that such a multi-counted particle, which belongs to more than one subvolume (as the red particle in the rightmost diagram of Figure 3.6 indicates), is properly handled by ray-particle intersection testing.

3.3.2 Creating a depth-independent 2D particle map: "littleJohn"

The particle-binning process, which determines which particles are contained within each subvolume, is a pre-processing step that makes subsequent ray-tracing calculations more efficient by reducing the number of particles that each ray segment must be tested against. However, for some photon positioning modes (discussed in section 3.4.1) an additional pre-processing step is necessary. This added procedure creates a set of two-dimensional particle maps in the X-Y plane, independent of depth, which together indicate the location of all particles in the scattering medium. These binary particle masks are used to inform the (*x, y*) origin positions of photon rays to increase the probability of scattering events, which reduces the number of direct rays that simply pass through the volume unscattered. Additionally, the number of filled cells in each binary particle mask (one mask for each X-Y subvolume) is used to determine how many rays to launch into that subvolume. This provides an avenue for *importance sampling*, where the most populated regions of the scattering medium are interrogated more often. The creation of these binary particle masks involves a process sometimes referred to as splatting, where the circular footprint of each spherical particle is accumulated in a matrix. This splatting process is depicted in Figure 3.7.

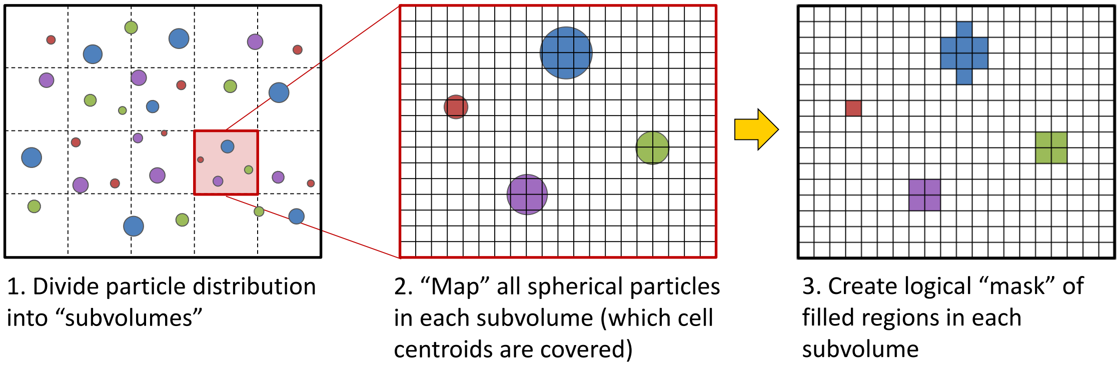

Figure 3.7. Diagram of the process for resolving the spherical particles in an X-Y subvolume into a mask of filled and unfilled cells.

The leftmost diagram shows an example of a polydisperse particle distribution, where diversity in aerosol radius is indicated by color. The thick outer border represents the X-Y extent of the overall medium, and the dashed lines indicate the X-Y boundaries between subvolumes. It is important to note here that each subvolume has a finite Z-extent, where Z is depth into the cloud (into the page, and thus not shown in this 2D depiction). Since the particle maps are depth-independent, the Z boundaries between subvolumes are essentially ignored during this procedure. It is as if an observer with no depth perception looks into the scattering medium normal to the X-Y plane and discretizes the positions of all particles.

The center diagram of Figure 3.7 enlarges an X-Y subvolume from the leftmost pictorial, and indicates how 3µm-wide cells are used to discretize particle positions. The black gridlines in this diagram show these cell boundaries; the centroid of each cell is computed and the equation of a circle is used to determine which cell centroids are "covered" by a particle in the X-Y subvolume based on its radius. Regardless of depth into the cloud, this process is repeated for all particles in a given X-Y subvolume until all 3µm (nominal and user-defined) cells are determined to be filled or empty. The result of this process, for the single X-Y subvolume exemplified in Figure 3.7, is shown in the rightmost illustration. The colors are meant to clarify the correspondence between the original spherical particles and the rectangular filled cells that represent them in the binary splat maps.

Taking this example further, suppose that there are 120 subvolumes in both the X and Y dimensions (120 x 120). Given a sufficient number of particles in the volume, a binary mask showing which subvolumes contain at least one particle might resemble that shown on the left in Figure 3.8 (assuming a 25% border is used for blanking around the perimeter). If the number of filled cells in each of the center 60 x 60 X-Y subvolumes was counted, a numerical map could be generated to display their relative population density. This is shown on the right in Figure 3.8, where the rainbow colors indicate deviation from the average number of particles in a subvolume. This indication of relative particle population for each subvolume is used by the 'littleJohn' method to cast more rays into the subvolumes which have more filled cells, to achieve uniform illumination.

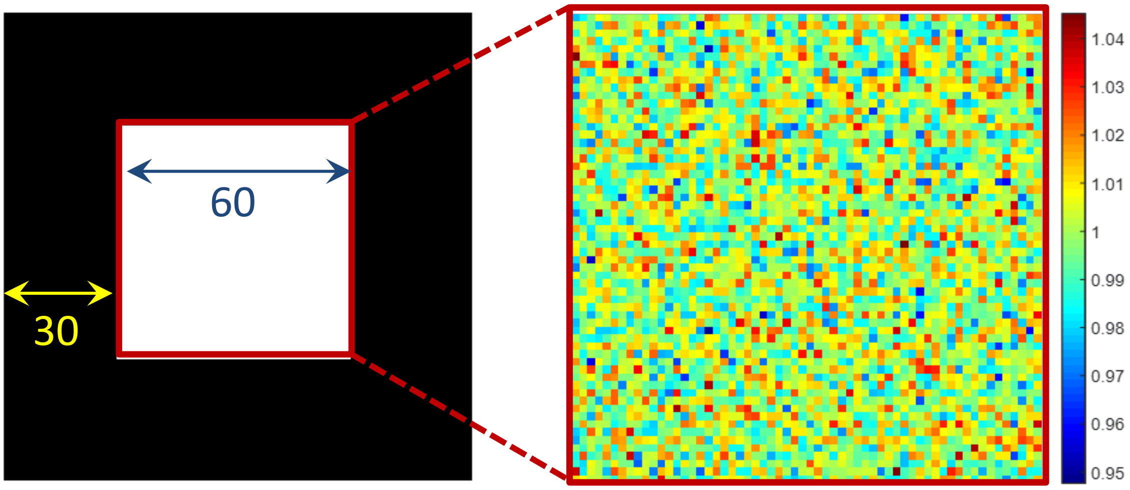

Figure 3.8. [Left] Example of a binary mask showing which subvolumes contain at least one particle; note that a border of subvolumes around the perimeter of the mask is voided to avoid rays being cast near the "chamber" walls. [Right] Map showing the number of filled cells in each subvolume, colored by variance from the average subvolume particle density.

An enlarged binary particle mask from a single X-Y subvolume (which would correspond to a single colored square pixel in the rightmost image of Figure 3.8) is shown in Figure 3.9. Yellow pixels indicate filled cells where a particle (at some unknown depth into the cloud) is present; blue pixels indicate empty cells. Illumination cast towards blue pixels would likely exit the cloud without scattering, contributing to the direct flux component.

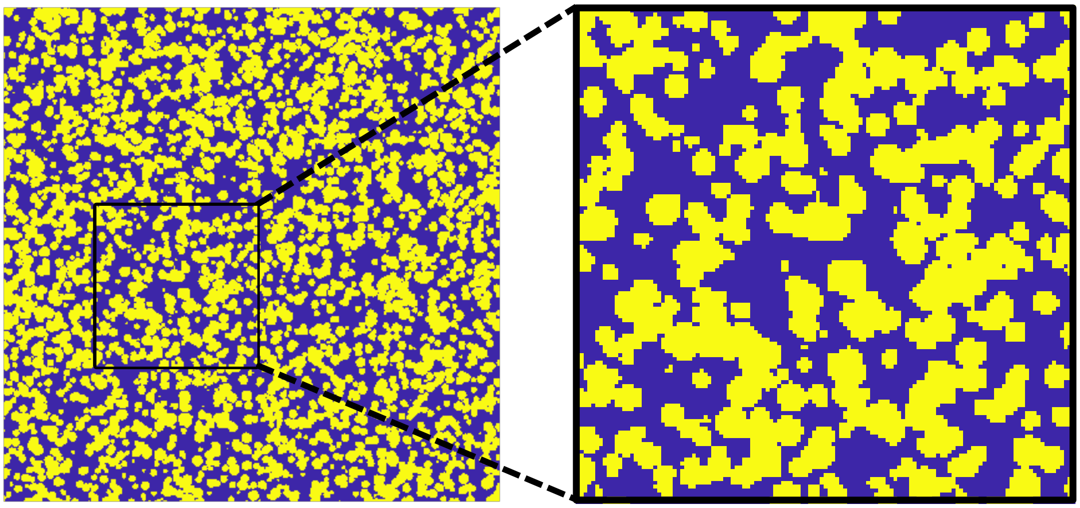

Figure 3.9. [Left] Example of a single particle-resolved subvolume taken from the center of the map shown in Figure 3.8; yellow cells indicate the presence of a particle (at any depth), and blue indicates the lack of particles where direct illumination would exit the cloud. [Right] Enlarged region of a single subvolume to illustrate particle resolution using 3µm cells to discretize a subvolume.

3.4 Ray Tracing Photon Paths

3.4.1 Initial Photon Positions

The (x, y, z) starting point(s) of the photon-rays cast by the scattering simulation can be initialized in four unique ways including 'single', 'robinHood', 'littleJohn' and 'random'. Each method starts all photon-rays in the X-Y plane where z is 0 (essentially, on the *origin* face of the cubic volume). Consequently, each ray has an initial position of $(x, y, 0)$ where the user's choice of ray positioning method determines how x and y are selected.

The '**single**' method initializes all rays to a starting location of $(0, 0, 0)$. This mode is the simplest but least useful for scientific study, intended only for debugging purposes. Whichever particle the first ray strikes is struck by all rays; if the first ray misses all particles, no collisions will occur.

The '**robinHood**' method aims each ray at a different particle in the distribution, in descending order from largest particle to smallest. For ray n and the corresponding particle n, this would result in a ray starting point of $(x_n, y_n, 0)$ if the intended particle centroid was (x_n, y_n, z_n). This mode is extremely useful for ensuring that each ray strikes a particle, both for debugging purposes as well as efficiency in the case of very thin clouds (see Figure 3.10). With sparse particle distributions where most randomly-placed rays would miss the relatively few particles, aiming directly at their centroids saves time when collisions are desired; 'robinHood' never misses.

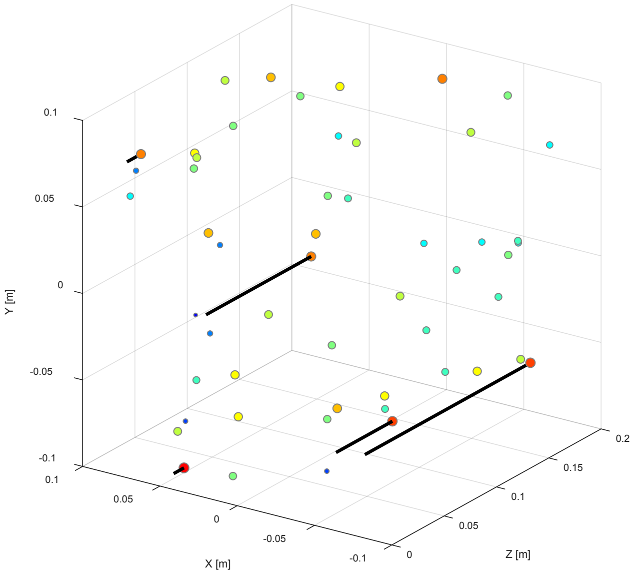

Figure 3.10. Representative example depicting five (5) photon rays cast into a volume using the 'robinHood' initial position method. Less than 50 particles were placed in the volume, yet each ray intersected one of the sparsely-placed spheres.

By first calculating the X-Y coverage of the volume by the particles in the distribution (regardless of depth), the percentage of rays that would have passed directly through the volume can be incorporated statistically in a post-processing step. This allows a relatively small number of rays to collide with sparsely-placed particles while accounting for the photons that were not cast because they would not have been aligned with a particle and hence would never have scattered. However, this forcing of rays (only) towards particle centers can also be a detriment; in a natural, physical (non-virtual) experiment, light would interact freely with any portion of a particle encountered. By aiming all rays exactly at particle centroids (and not particle edges), volumetric sampling artifacts may occur with this photon casting method. Also, spatial depth of particles in the chamber is not a factor when determining initial X-Y ray locations. This means that particles "shadowed" by a particle between it and the illumination source may not be intersected even if selected, as the ray intended for it may strike the closer occluding particle (depending on relative particle sizes and centroid separations).

The '**littleJohn**' method can be thought of as a compromise between the 'random' and 'robinHood' modes, where ray starting points are randomly generated but statistically informed by the spatial location of particles in the volume. Essentially an importance sampling technique, the 'littleJohn' positioning mode relies on the statistical particle density map (shown at right in Figure 3.8) and the binary particle cell maps (illustrated in Figure 3.9). The number of rays sent into each subvolume depends on the particle surface area contained in that region, and the random location of rays headed into that subvolume are positioned inside filled cells. An overview of this process is illustrated in Figure 3.11.

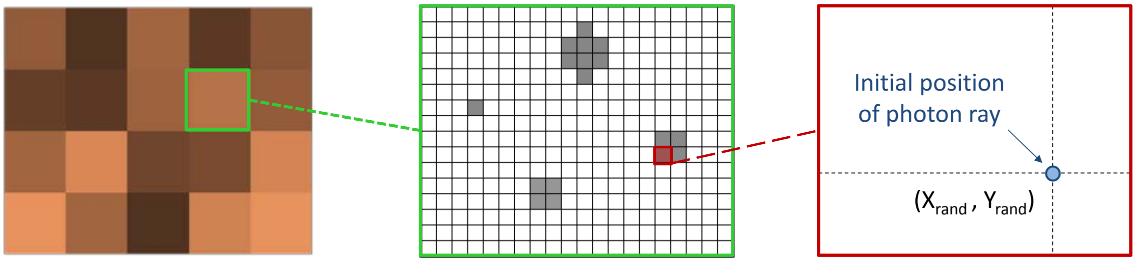

1. Select a *random* subvolume (without replacement)

2. Select a filled cell at random (with replacement) **N** times *based on filled area of subvolume*

3. Choose a random (X,Y) location within the filled cell

Figure 3.11. Process used by the ‘littleJohn’ ray positioning method. A random subvolume is selected, and the relative number of filled cells it contains is used to calculate the number of rays cast into that subvolume. Each of these rays is cast, in a random X-Y location, inside a random chosen filled cell.

Rays are cast into each subvolume containing at least one particle, though the order of X-Y subvolume interrogation is chosen at random without replacement (Figure 3.11, left). Additionally, and critically, the number of rays cast into each subvolume is weighted by the number of filled cells in that subvolume (refer to Figure 3.8, right). This serves the purpose of uniform illumination; to maintain a constant flux on a larger particle (greater surface area), more rays must be cast in its direction. Imagine two cloud aerosols, one the size of a beach ball and other with a radius of 8μm. Casting a single ray towards each would underemphasize the impact of the larger particle, and would violate the uniform illumination concept. Consequently, more rays are needed for subvolumes with more particle surface area to achieve a constant flux (e.g., W/m^2).

Once the particle surface area-weighted number of rays has been calculated, and the subvolume has been selected at random (without replacement to avoid duplication and over-illumination), the actual (x, y) positions of the rays are chosen. This is done by choosing a filled cell from the subvolume’s particle map at random but with replacement (as shown in the center image of Figure 3.11). The actual (x, y) position inside this filled cell is chosen randomly, as indicated by the right-most image in Figure 3.11. This increases the impact of importance sampling in this method, as rays are cast towards the micro-regions most likely to contain particles. However, it should be noted that since the cells are rectangular, they may contain a spherical particle which covers the cell centroid but does not fill the entire cell. Due to the randomly-selected (x, y) location in the cell, rays may occasionally be sent in a direction that will not induce scattering. These accidentally-direct rays are removed from reported statistics; afterwards, the correct amount of direct illumination is added based on the combined filled area of all binary particle maps. This accounts for all rays which would have been cast towards empty space in the distribution but were not to save computations to which the answer was already known. As a result, compared to the 'robinHood' mode, the 'littleJohn' method is less accurate (and thus less efficient, as some rays accidentally pass through directly without scattering) but statistically "stronger" as it mitigates the volumetric sampling artifacts of the 'robinHood' method with increased randomness.

The '**random**' initialization method starts all photon-rays at uniformly-random locations in the X-Y plane defined by the origin face. Sampling artifacts are reduced or eliminated with this approach, and when a sufficiently large number of particles are present in the distribution, rays cast towards empty space (where no particles will be encountered) are minimized. By tracing a sufficiently large number of rays through the particle distribution, a faithful representation of uniform illumination can be achieved. For thick clouds, the 'random' mode is the most computationally efficient way to produce accurate results. For all the analysis presented in this dissertation, the (x, y, z) starting points of the rays cast by the scattering simulations were initialized with the 'random' mode.

Currently, all four of these methods employ an initial scattering angle of zero (straight from the origin face toward the opposite face of the cubic volume). This starting polar angle is currently hardcoded to a value of 0 but could be exposed for user specification.

3.4.2 Particle-Ray Intersection Testing

The occurrence of a scattering event is determined by the geometrical relationship between rays cast through the volume and the spherical particles (including their scattering efficiency) it contains. The scattering medium is divided into numerous subvolumes, as previously described, leaving a manageable number of particles (perhaps 20) in each subvolume. This increases the efficiency of the scattering simulation, as ray-particle intersection testing is expedited when only a few (e.g., 20) particles must be checked against the ray segment instead of all the particles (e.g., 32 x 10^6) in the volume. With this in mind, the basic process involves the following steps:

1. Determine which particles are contained in the subvolume of interest
2. Loop over all particles in the subvolume
3. Test each particle, independently, to see if there is a collision between the particle and the ray in question
4. For the subset of particles intersected by the ray, calculate which of these ray-scattering particles is closest to the ray origin (point of first collision)
5. Record ray-particle collision point, to be used as the next ray origin (after a new scattering angle has been chosen to set the direction of the next ray segment)

Fundamentally, this process is relatively straightforward. However, beyond lots of meticulous bookkeeping, a mathematically-efficient method for ray-particle intersection testing is needed. The *mcScatter* simulation is based on an analytic solution to algebraic equations for the implicit shapes of both rays and spheres. While a concise mathematical treatment has been published elsewhere (Matsuda et al., 2012), a more graphical and detailed explanation is included here to aid those who wish to implement a similar routine.

All the points that lie on a ray segment can be described by a set of equations, with an equation for each dimension. Similarly, all the points that lie on the surface of a sphere can be described by a single quadratic expression. For a 3D ray passing near a spherical particle, a set of four equations with four unknowns can be written, and the solution (or lack thereof) determines if a scattering collision has occurred. Figure 3.12 illustrates the ray-particle intersection geometry, drawn both in 3D (at right) and viewed in only two dimensions for clarity (left).

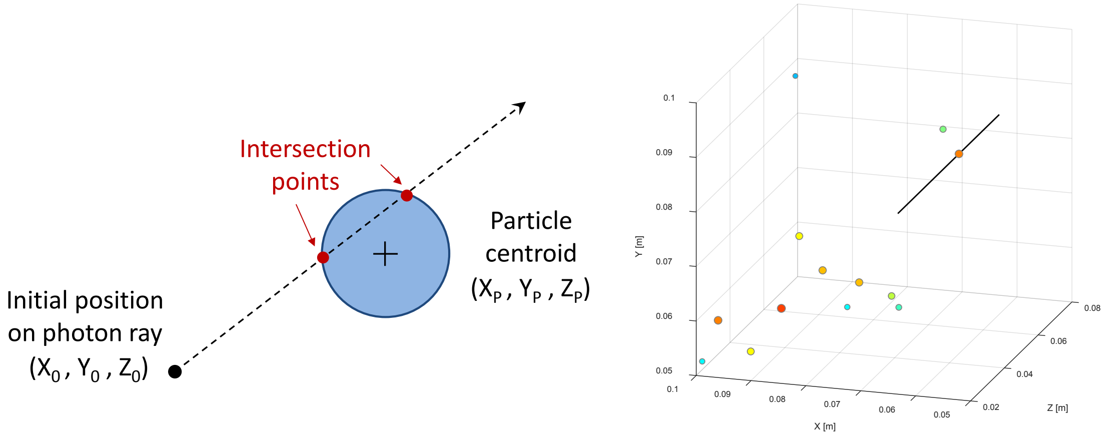

Figure 3.12. Illustration of ray-sphere intersection test (left). Depiction of a ray passing through a particle in the volumetric distribution (right).

Assuming the spherical particle under test is centered at (X_P, Y_P, Z_P) with a radius of R_P and scattering efficiency Q_{sca}, the set of (x, y, z) points on its 3D surface can be described with the expression

$$(x - X_P)^2 + (y - Y_P)^2 + (z - Z_P)^2 - (Q_{sca} \cdot R_P^2) = 0 \tag{18}$$

Since the centroid and radius of the sphere are known, this single quadratic equation has three unknowns which together describe the (x, y, z) surface of the sphere. The three-dimensional ray under examination can be expressed by a set of three equations, one for each dimension, namely

$$\begin{gathered} x = X_0 + t \cdot dX \\ y = Y_0 + t \cdot dY \\ z = Z_0 + t \cdot dZ \end{gathered} \tag{19}$$

In this system of ray equations, (X_0, Y_0, Z_0) represents the ray origin, (dX, dY, dZ) are the normalized ray directions, and (x, y, z) is the endpoint of the ray assuming its scalar length is t. A positive value of t describes points that lie *forward* on the ray in the direction of its travel, while negative values of t describe the ray segment behind the ray origin (*backward*). The ray-based definitions of (x, y, z) from Equation (19) can be substituted into the quadratic sphere surface described by Equation (18), leaving a single equation with a single unknown (i.e., *t*), as shown in Equation (20).

$$(X_0 + t \cdot dX - X_P)^2 + (Y_0 + t \cdot dY - Y_P)^2 + (Z_0 + t \cdot dZ - Z_P)^2 - (Q_{sca} \cdot R_P^2) = 0 \quad (20)$$

The task that remains is to determine if a valid (i.e., both real and positive) value(s) of *t* exists. Solving Equation (20) for *t* yields the expression

$$t = \frac{-b \pm \sqrt{b^2 - 4ac}}{2a} \quad (21)$$

if we define *a*, *b* and *c* as follows:

$$\begin{gathered} a = (dX^2 + dY^2 + dZ^2) \\ b = 2 \cdot [(X_0 - X_P) \cdot dX + (Y_0 - Y_P) \cdot dY + (Z_0 - Z_P) \cdot dZ] \\ c = (X_0 - X_P)^2 + (Y_0 - Y_P)^2 + (Z_0 - Z_P)^2 - \left(Q_{sca} \cdot R_P^2\right) \end{gathered} \quad (22)$$

Several important distinctions can be made by examining the discriminant (b^2 - $4ac$).

- If the discriminant is *negative*, the roots are imaginary and thus there is no valid intersection.
- If the discriminant is *exactly zero*, yielding a single real positive root, then a single collision will occur (ray is tangent to spherical particle, touching its surface at a single point).
- If the discriminant is *positive* and $t > 0$, then the presence of two real positive roots implies a double collision. When a ray-particle collision occurs, a double collision is most likely as the ray enters the sphere at one location and exits at another. This scenario is depicted in the left-most diagram in Figure 3.12.

When a ray intersects a particle, the collision point is recorded as the particle centroid (and not the point on the sphere's surface); the subsequent ray segment begins from this centroid. This method simplifies bookkeeping but also assumes that any possible tendency to scatter light more frequently to the collision side (rather than equal probability from the particle center) can be safely neglected. Consecutive collisions with the same particle are not allowed. An illustration of a typical simulation result is shown in Figure 3.13, with just a subset of rays depicted for clarity.

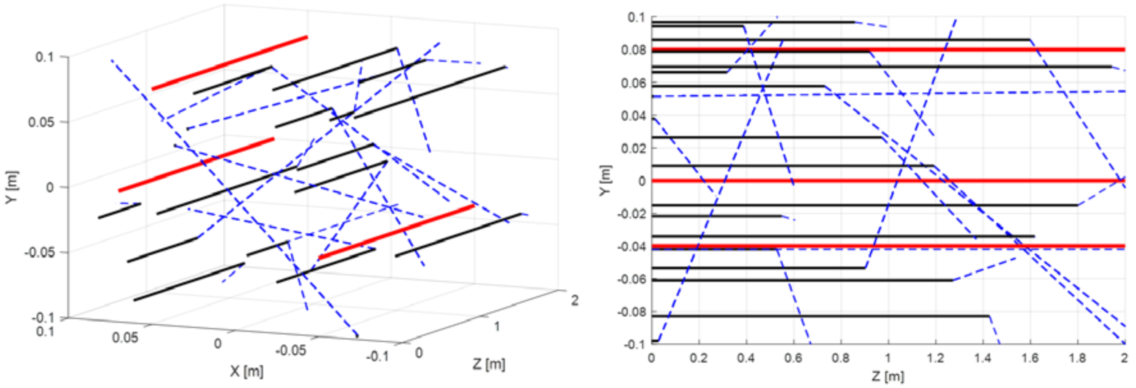

Figure 3.13. Illustration of photon propagation paths recorded by a Monte Carlo scattering simulation; an orthographic 3D view is shown (left) along with a 2D side view (right). In the side view in the right-hand panel, rays originate at Z = 0 m and traverse through the virtual cloud towards Z = 2 m. Collimated rays (shown with solid black lines) are cast into the particle-laden medium, and scattering events redirect these now-diffuse rays (depicted with dashed blue lines). Direct rays that pass all the way through the medium without becoming diffuse are shown with thick red lines.

3.4.3 Phase functions

The scattering phase function describes the angular distribution of light intensity scattered by a particle for a given wavelength. This particle-induced redirection of radiation from the original propagation direction is not always isotropic. In the case of cloud droplets and visible light, the resultant size parameter yields a scattering pattern that is forward-dominant. One of the most accurate ways to calculate the scattering phase function is through Mie theory, where particles are considered dielectric spheres and the Pointing vector (expressed as electric and magnetic field expansion series) is integrated.

However, it is often convenient to have an analytic formula that approximates the actual scattering phase function shape. The Henyey-Greenstein phase function, essentially a probability density function (PDF), is a common surrogate for the actual phase function (Henyey and Greenstein, 1941). Its analytic form allows it to be integrated to calculate a closed-form cumulative density function (CDF). Its parametric nature allows it to be employed rather simply, with sufficient accurate for many applications.

The *mcScatter* software makes both Mie and HG (Henyey-Greenstein) phase functions available for scattering simulations, as the GUI provides users with the choice between them. In the case of the HG phase function, which relies solely on the asymmetry parameter (g), the probability density function $p(\cos\theta)_{HG}$ can be written as

$$p(\cos\theta)_{HG} = \frac{\frac{1}{2}(1-g^2)}{(1+g^2-2g\cos\theta)^{3/2}} \tag{23}$$

However, since Monte Carlo simulations require a cumulative density function from which to randomly draw, the PDF must be integrated over all possible scattering angles (0° to 180°). Analytically, after solving for $\cos\theta$, this results in the expression

$$\cos\theta = \frac{1}{2g}\left[1 + g^2 - \left(\frac{1 - g^2}{1 + g \cdot (2 \cdot rand - 1)}\right)^2\right] \tag{24}$$

where *rand* refers to a uniform random number in the range [0-1]. During the scattering simulation, each time a new scattering angle is required, a random number is drawn and substituted into Equation (24) to generate a $\Delta\theta$ to add to the current polar angle of the ray.

Histograms of the recorded Δθ (polar scattering angles drawn from the HG distribution) can be computed and compared to the closed-form analytic expressions to ensure a trustworthy implementation. Figure 3.14 shows such a comparison, with cumulative density functions on the left subplot and probability density functions on the right. Mie theory is used to compute an accurate asymmetry parameter, *g*; this is shown in the PDF subplot legend for comparison with the experimentally-obtained ensemble average, $g = \langle\cos\theta\rangle$. The target asymmetry parameter (*g*) used to plot the red-dashed analytic curves matches the experimentally-obtained $g = \langle\cos\theta\rangle$ ensemble average shown in the legend. The number of random draws (scattering events) necessary to closely match the analytic distributions for a given asymmetry parameter was determined to be 100,000 or more.

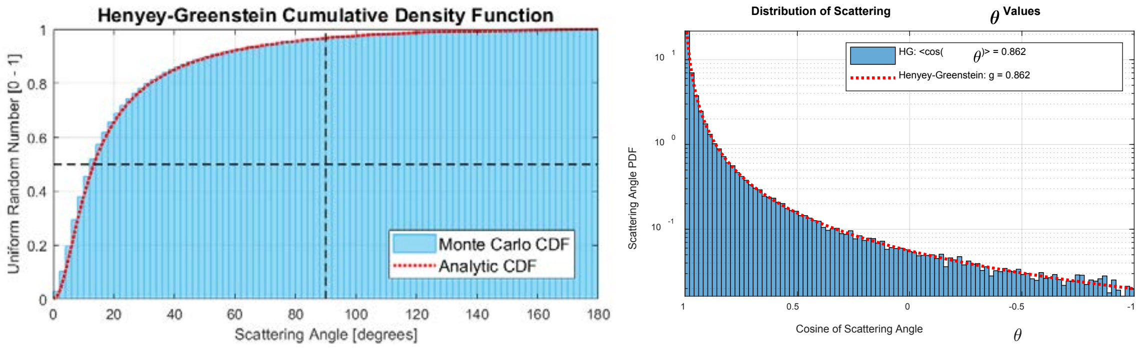

Figure 3.14. Cumulative density functions (left) and probability density function (right) computed from Monte Carlo statistics, compared to the Henyey-Greenstein analytic expressions (red dashed lines).

Simulations can utilize Mie scattering phase functions instead of the commonly-employed HG alternative. Figure 3.15 shows a representative example of a Mie scattering phase function calculated by *mcScatter* for an optical wavelength of 550nm, particle radius of 8µm and a (complex) refractive index of 1.3356 + *j*2.36 x 10^{-9} for the scattering medium (water). The Mie phase function used by mcScatter is shown along with that from a well-regarded software package called *MiePlot* (philiplaven.com). The two phase functions, shown on a logarithmic scale due to the dominant forward-scattering peak near zero degrees, match almost exactly.

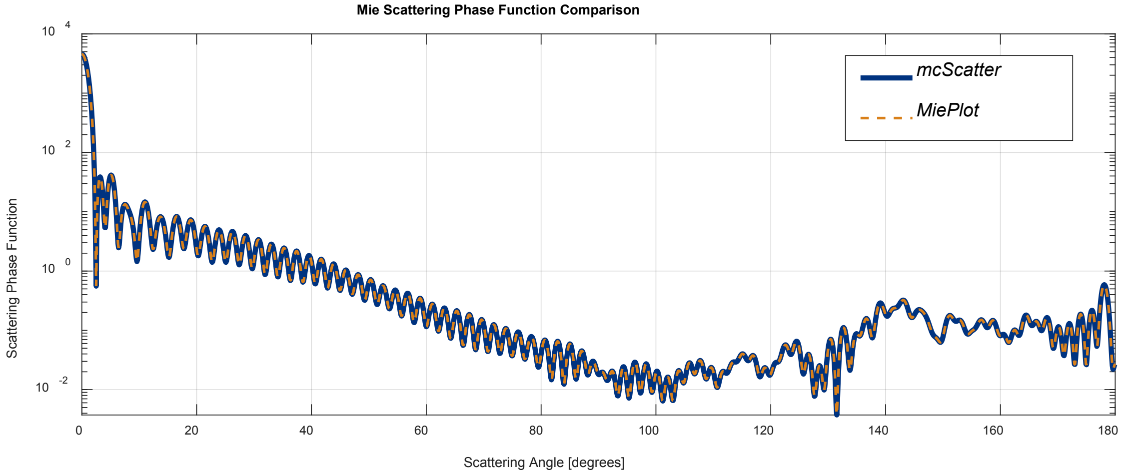

Figure 3.15. Representative comparison between the Mie scattering phase function in the *mcScatter* application and an output from Philip Laven's *MiePlot*. An optical wavelength of 550nm, droplet radius of 8 microns and a refractive index of 1.3356013 + *j*2.46E-09 was used for Mie scattering calculations.

These Mie probability density functions can be integrated over scattering angle and normalized to produce cumulative density functions for scattering angle generation. Like the HG polar angle generation method, uniform random numbers are drawn and used to calculate new scattering angles based on the Mie phase function results. In a polydisperse medium, the new scattering angle that results from each ray-particle collision is based on the appropriate precomputed droplet radius-specific phase function.

It is important to note that the HG phase function, which is meant to approximate the more accurate Mie PDF, makes some compromises regarding emphasis of forward-, side- and back-scattering. Figure 3.16 shows both the Mie and HG phase functions for a 14µm-radius water droplet (with a refractive index of $1.3356013 + j2.46\text{x}10^{-9}$) for the sake of comparison. Figure 3.17 illustrates the two phase functions near the forward scattering lobe; note the orders of magnitude difference between them near $\cos\theta = 1$.

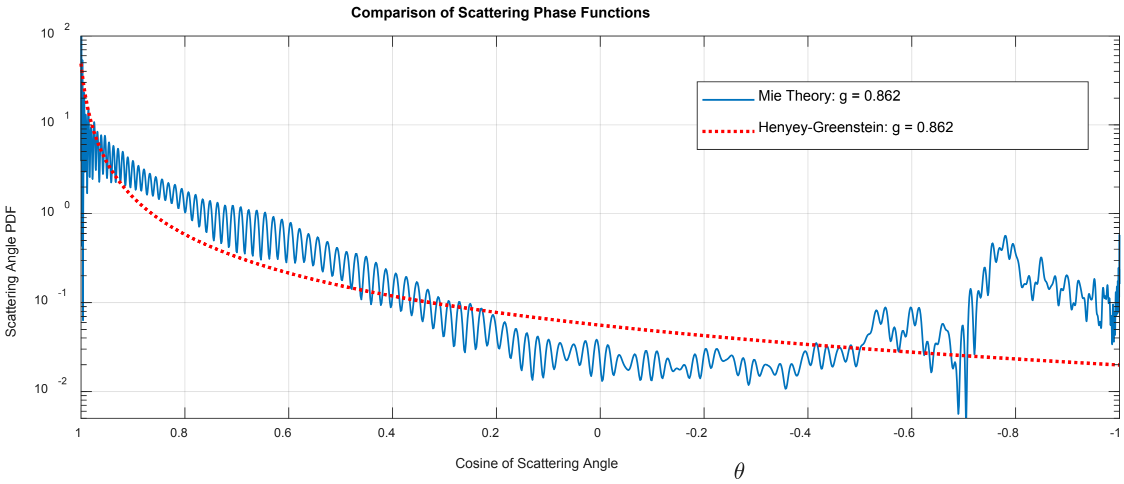

Figure 3.16. Comparison of phase functions calculated with Mie theory and approximated by the analytic Henyey-Greenstein (using a Mie-based asymmetry parameter).

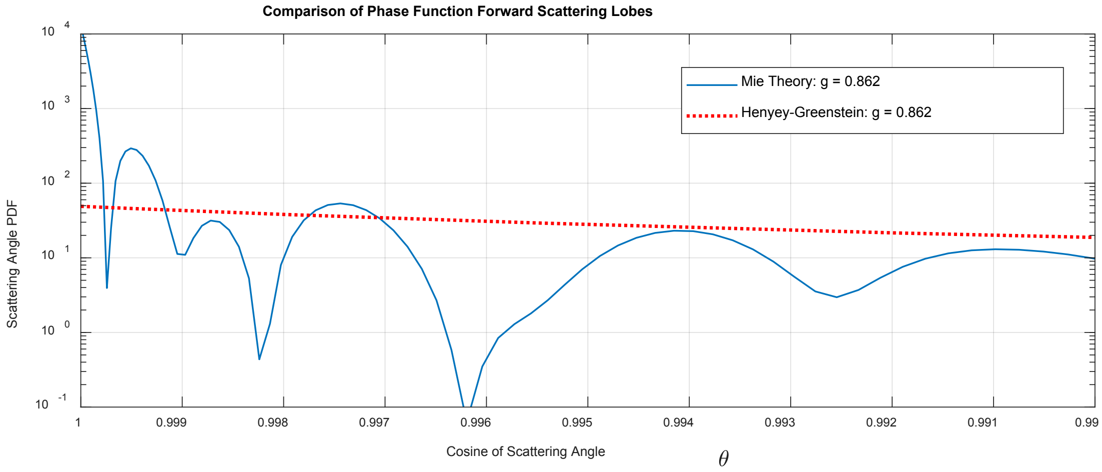

Figure 3.17. Comparison of the forward scattering lobes of the Mie theory and analytic Henyey-Greenstein phase functions.

3.4.4 Particle volume wall boundary conditions

The boundary conditions of the particle volume side walls can be set to one of four (4) modes including ‘absorbing’, ‘periodic’, ‘reflective’ and ‘diffuse’. For convenience the six (6) walls or “faces” of the cubic volume are referred to using the following labels:

- **Origin** (origination face for radiation, where photon-rays are cast from)
- **Sensor** (rays are cast from the Origin face towards this opposing face)
- **Right** and **Left** (opposite each other, orthogonal to Origin)
- **Top** and **Bottom** (opposite each other, orthogonal to Origin)

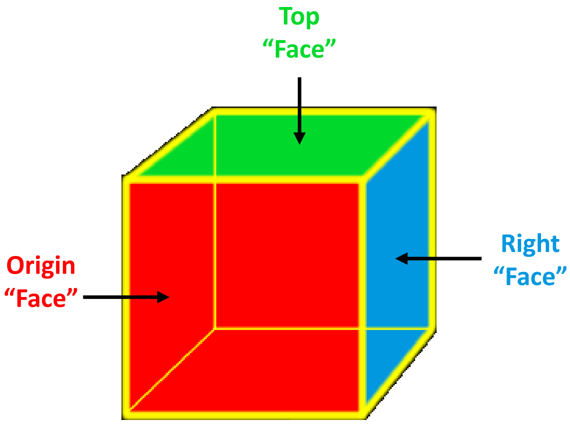

Figure 3.18. Particles are contained in a cubic volume with six (6) walls or "faces".

The '**absorbing**' mode treats all 6 faces of the cube as perfect absorbers with a reflectivity of zero. Any photon that strikes a face stops immediately at the point of impact; the ray ends, the path length ends, and the face struck is recorded for eventual reporting by the simulation output.

The '**periodic**' mode treats the *Right*, *Left*, *Top* and *Bottom* faces as soft boundaries. Rays that strike them are not terminated (as they would be with the 'absorbing' mode). Instead, the would-be termination point of the ray becomes the starting point of a new ray on the opposite wall. The new ray has the same scattering and azimuthal angles as the previous but will be cast into the volume instead of leaving the volume. This extends the possible path lengths that a ray can traverse. Essentially the size of the volume and number of particles can be extended, approximating a cloud whose lateral extent is infinite, without requiring an inordinate amount of memory (see Figure 3.19). Otherwise, the ray would have either terminated (artificially shortening the path length) or exited the particle volume (into a vacuum where no scattering could occur), violating the plane-parallel concept. When in 'periodic' mode, rays can terminate only on the *Origin* and *Sensor* faces. All analysis performed for this dissertation employed the 'periodic' mode.

The '**reflective**' and '**diffuse**' wall conditions, like the 'periodic' mode, allow ray termination only on the *Origin* and *Sensor* walls. When one of the other four faces is struck by a ray, the ray is reflected back into the particle chamber. If 'reflective' is selected, the reflection angle is based on a specular wall assumption, where the incident and outgoing rays follow Snell's law. For 'diffuse' reflections, the new angle is random and independent from the incident angle. Currently, both these modes are inoperable.

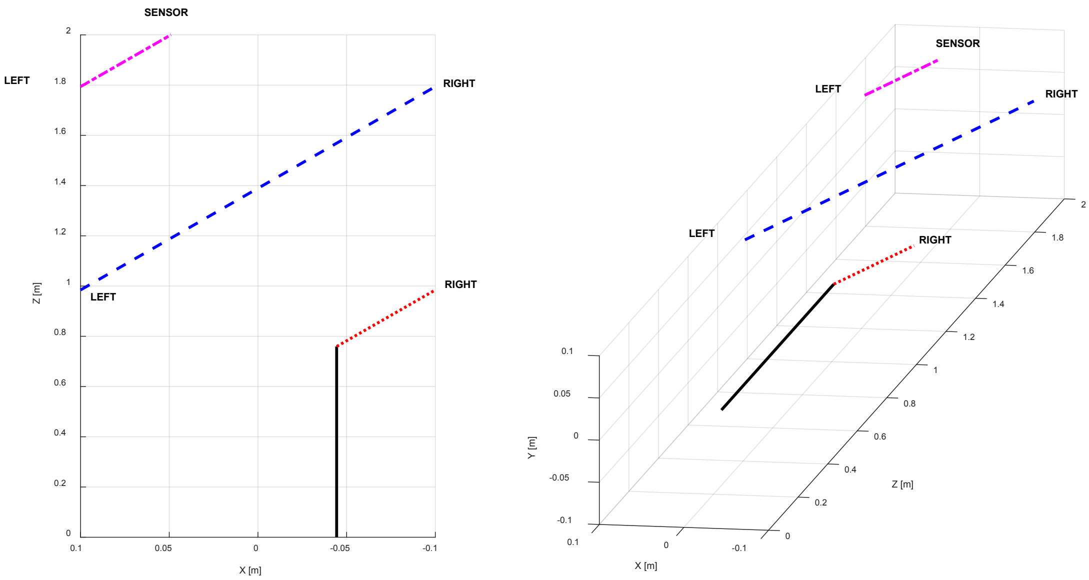

Figure 3.19. Illustration of the ‘periodic’ wall condition, where a ray wraps around until it terminates on the *Sensor* face. The solid black line segment represents the direct path, prior to and up until the first collision. The red dotted line shows the second path segment, after the first collision and until the *Right* face is struck. The ray wraps around and then is cast from the *Left* face at the same angle (shown with a dashed blue line). The *Right* face is struck again, and the last ray segment (shown as a magenta dash-dot line) begins on the *Left* wall and terminates on the *Sensor* face. For increased clarity, both a top view (left) and oblique perspective (right) are depicted.

3.5 Monte Carlo scattering inputs

The *mcScatter* simulation software is capable of running in many ways, with several modes provided to control a number of behaviors. Screenshots of the GUI are shown here with some description of the inputs and the intent behind them, to elucidate the potential user of *mcScatter* as to the proper settings needed to achieve a desired output.

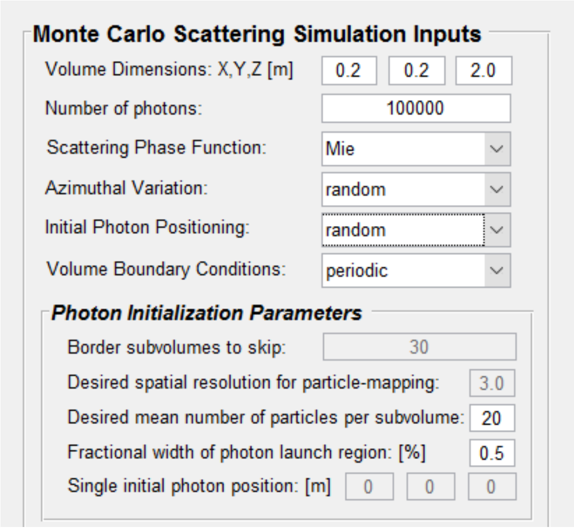

Monte Carlo Scattering Simulation Inputs

Volume Dimensions: X,Y,Z [m] 0.2 0.2 2.0

Number of photons: 100000

Scattering Phase Function: Mie

Azimuthal Variation: random

Initial Photon Positioning: random

Volume Boundary Conditions: periodic

Photon Initialization Parameters

Border subvolumes to skip: 30

Desired spatial resolution for particle-mapping: 3.0

Desired mean number of particles per subvolume: 20

Fractional width of photon launch region: [%] 0.5

Single initial photon position: [m] 0 0 0

Figure 3.20. Primary inputs for controlling the behavior of *mcScatter* simulations.

The primary inputs of the scattering simulation, shown in Figure 3.20, are grouped together on the *mcScatter* GUI. They are described only at a high-level here in Table 3-1; more detail on some of the more unique modes is given elsewhere.

Table 3-1. Description of primary *mcScatter* simulation inputs.

Input	**Description**	**Units**
Volume Dimensions	Outer dimensions of scattering volume	meters
Number of photons	Number of rays cast into the volume	photons
Scattering Phase Function	Phase function to use for scattering: [‘Mie’, ‘HG’, ‘random’, ‘none’]	*n/a*
Azimuthal Variation	Variation of azimuthal angle upon a scattering event: [‘random’, ‘none’]	*n/a*
Initial Photon Positioning	Method of choosing the initial (*x,y*) position of each ray: [‘littleJohn’, ‘robinHood’, ‘random’, ‘singleInit’]	*n/a*
Volume Boundary Conditions	Boundary conditions to assign the virtual walls of chamber: [‘absorbing’, ‘periodic’, ‘reflective’, ‘diffuse’]	*n/a*
Border subvolumes to skip	Number of subvolumes around the perimeter of the volume to disallow ray casting (for the ‘littleJohn’ positioning method only; reducing particle mapping time and avoids edge-casting if ‘periodic’ positioning mode is not selected)	subv.
Desired spatial resolution for particle-mapping	Edge dimension of cells used to discretize the particles in a subvolume (for the ‘littleJohn’ positioning method only)	µm

Desired mean number of particles per subvolume	Average number of particles to target for each subvolume (no. of subvolume is increased to reach this target; used by all positioning modes except ‘littleJohn’)	#/subv.
Fractional width of photon launch region	Width of chamber to allow rays to originate from (to avoid casting near an edge; used for ‘random’ positioning method only)	%
Single initial photon position	Initial (x,y,z) position for all rays (for ‘singleInit’ positioning method only)	meters

Several atmospheric parameters, listed in Table 3-2, are provided as inputs to the scattering simulation (see Figure 3.21). These are used to control the type of coherent light assumed for the simulation and the scattering medium into which photon rays are cast.

Table 3-2. Description of atmospheric input parameters

Input	**Description**	**Units**
Optical wavelength	Wavelength of light in simulation	µm
Refractive index of air	Refractive index of air	*n/a*
Refractive index of particle [real]	Real component of refractive index of particles in scattering medium	*n/a*
Refractive index of particle [imag]	Imaginary component of refractive index of particles in scattering medium	*n/a*

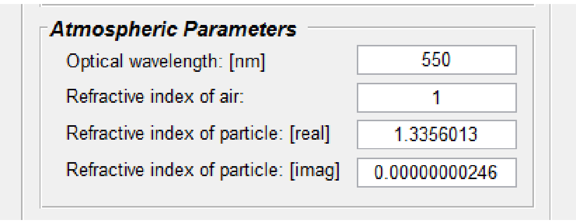

Atmospheric Parameters

Optical wavelength: [nm] 550

Refractive index of air: 1

Refractive index of particle: [real] 1.3356013

Refractive index of particle: [imag] 0.00000000246

Figure 3.21. Inputs to *mcScatter* simulation for atmospheric parameters.

The last input group (Figure 3.22) controls the method of particle location generation, the density and size distribution of those particles. Additionally, an estimate of the total number of particles required to achieve the user’s specifications and the resultant optical depth are shown for convenience prior to running the simulation. The intention of these estimates is to avoid running out of memory (due to too many particles) or simulating a cloud with an undesirable optical depth. These inputs are summarized in Table 3-3.

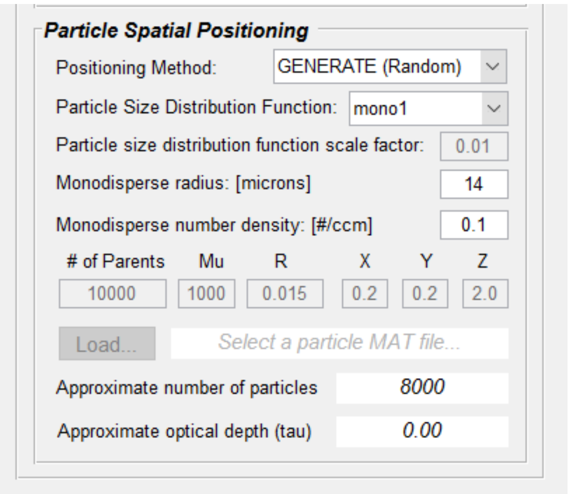

Positioning Method: GENERATE (Random)
Particle Size Distribution Function: mono1
Particle size distribution function scale factor: 0.01
Monodisperse radius: [microns] 14
Monodisperse number density: [#/ccm] 0.1

# of Parents	Mu	R	X	Y	Z
10000	1000	0.015	0.2	0.2	2.0

Approximate number of particles 8000
Approximate optical depth (tau) 0.00

Figure 3.22. Inputs to *mcScatter* simulation for spatial positioning of particles.

Table 3-3. Inputs for controlling the particle distribution generated for scattering.

Input	**Description**	**Units**
Positioning method	Method for generating spatial locations of particles [‘random’, ‘Matérn’, ‘Load’]	*n/a*
Particle size distribution function	Either a pre-determined polydisperse cloud or a user-defined monodisperse cloud can be generated [‘cloud1’, ‘mono1’]	*n/a*
Particle size distribution function scale factor	Scalar for reducing the total number of particles created while preserving the ratios between each particle radius	*n/a*
Monodisperse radius	Controls the particle radius for monodisperse cloud simulations	µm
Monodisperse number density	Defines number density for monodisperse cloud simulations	#/cm^3
Number of parents	Number of Matérn parents of particles (e.g., groups or clusters)	*n/a*
Mu	Mean number of particles contained in each Matérn parent or cluster	#/parent
R	Radius of Matérn clusters	*n/a*
< X, Y, Z >	Extent of Matérn particle domain	meters
Load…	Opens a file dialog to load a saved particle distribution (currently unavailable)	*n/a*
Approximate no. of particles	Estimate of the total number of particles required by the current simulation inputs	#
Approximate optical depth	Estimate of the total optical depth, τ, with the current simulation inputs	*n/a*

3.6 Running a Monte Carlo scattering simulation

A complete Monte Carlo simulation involves undertaking several major steps including particle distribution generation, dividing particles into subvolumes, and finally casting rays into the scattering medium and tracing their propagation paths. In a typical *mcScatter* simulation, all three steps would be enabled (via the checkboxes shown in Figure 3.23) and the LAUNCH button would be pressed.

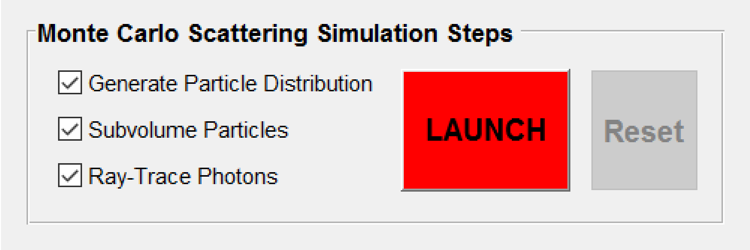

☑ Generate Particle Distribution
☑ Subvolume Particles
☑ Ray-Trace Photons

Figure 3.23. Controls for launching a *mcScatter* simulation

These three primary tasks each require several sub-tasks, detailed here:

Generate Particle Distribution:

1. First, optical properties and scattering phase functions are calculated for all required particle radii using Mie theory. The outputs of the Mie calculations, which are dependent on the particle radii (and optical wavelength), include:
    - scattering coefficient, k [m^{-1}]
    - scattering efficiency, Q_{sca}
    - asymmetry parameter, g
    - unpolarized scattering phase function, S
    - cumulative density function (CDF_S) for the phase function
2. Next, the spatial locations of the required number of particles are generated based on user inputs for number density and desired degree of homogeneity. The outputs include (x, y, z) 3D positions and corresponding radii values for all particles inserted into the virtual distribution volume. The number of subvolumes either specified or required by various user inputs are determined here as well.
3. Finally, a set of quantitative results are displayed in the right-most output window. These, described in greater detail in section 0, include the following:
    - scattering phase function method
    - azimuthal angular variation method
    - initial photon positioning method
    - modal aerosol/particle/droplet radius

    - total number of particles
    - particle number density
    - total scattering coefficient
    - propagation range from top to bottom of the virtual cloud
    - lateral dimensions (width and height) of particle distribution
    - total optical depth

Subvolume Particles:

1. The X-Y-Z limits of each subvolume (and their secondary boundaries once an additional margin is included) are calculated. These are used to determine which particles are located inside each subvolume, to expedite the ray-particle intersection testing involved in ray-tracing a particular subvolume.

2. During the prior step (determination of which particles are in each subvolume), additional particle discretization is performed if the ‘littleJohn’ initial positioning method has been selected due to the inputs required for this mode. These additional outputs include:
    - binary map indicating which subvolumes contain at least one particle
    - binary masks indicating which cells in a given subvolume are “filled”
    - numerical maps indicating the number of filled cells in each subvolume
    - numerical maps specifying the number of rays to cast into each subvolume based on total desired rays and number of particle cells in each subvolume

Ray-Trace Photons:

1. The ray-tracing procedure, which involves casting photons into a scattering medium and calculating their propagation through the virtual cloud, is complex. It involves a lot of bookkeeping, conditional logic and calculations along the way. The major functions performed by the ray-tracer for each photon cast into the particle distribution independently include:
    - Determining initial $(x, y, 0)$ ray origination points
    - Determining initial polar and azimuthal ray angles
    - Tracing each ray through the subvolumes that comprise a virtual cloud
    - Searching for intersections between each ray and particles contained in the subvolumes they traverse
    - Calculating new scattering angles and subsequent ray directions when ray-particle collisions occur

    - Following the propagation of rays through subvolumes filled with particles until a ray termination point is reached

2. The primary ray-tracing outputs recorded by this sophisticated scattering simulation include:
    - Array of polar and azimuthal scattering angles, recorded independently from photon ray, to compare against intended probability distributions
    - X, Y and Z arrays recording the initial, final and intermediate collision positions of each photon ray
    - Array indicating which face each ray struck upon termination
    - Arrays containing the direct and diffuse forward flux and diffuse backward flux for comparison against two-stream theory and alternative Monte Carlo codes

As the three primary steps of the scattering simulation are performed, the user is apprised of their status on the GUI. Figure 3.24 shows screenshots of the status portion of the GUI. The image on the left is seen before a simulation has begun; the right-hand image is an example of a status report seen while particles are being categorized into subvolumes.

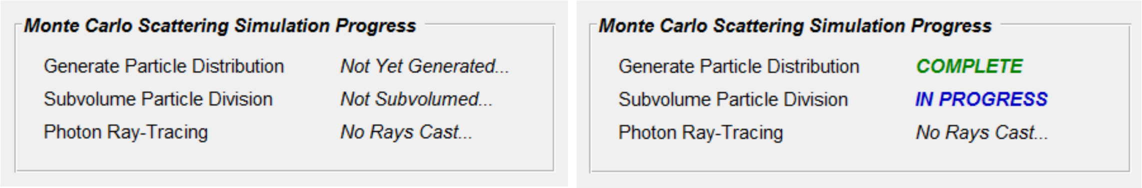

Monte Carlo Scattering Simulation Progress

Generate Particle Distribution *Not Yet Generated...*
Subvolume Particle Division *Not Subvolumed...*
Photon Ray-Tracing *No Rays Cast...*

Monte Carlo Scattering Simulation Progress

Generate Particle Distribution ***COMPLETE***
Subvolume Particle Division ***IN PROGRESS***
Photon Ray-Tracing *No Rays Cast...*

Figure 3.24. Status updates are reported to the user via the *mcScatter* GUI.

With some minor code changes, it would be possible for a subset of these steps to be used individually or together for various purposes. For example, users could choose only to Generate Particle Distribution without performing a scattering simulation.

3.7 Monte Carlo scattering simulation feedback

The *mcScatter* simulation provides feedback to the user regarding the specifics of progress including the time required for various steps. This feedback helps the user understand which steps are the most time consuming and aids in estimating the computation time remaining. An example of simulation feedback provided via the mcScatter GUI is shown in the two panels of Figure 3.25.

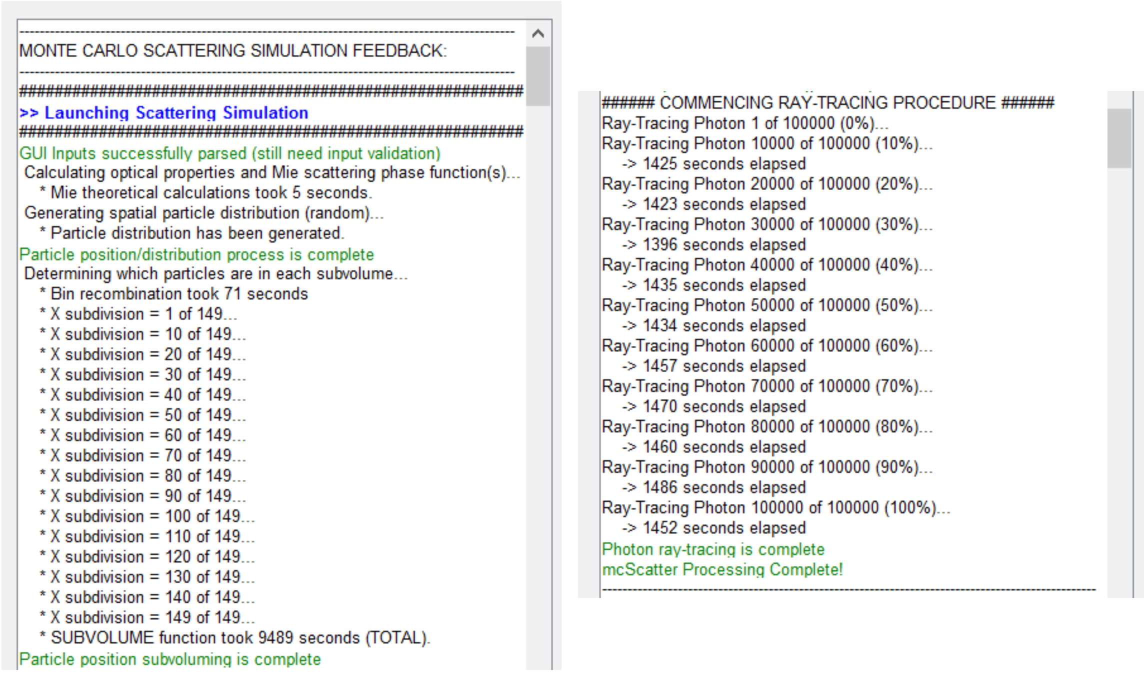

```
--------------------------------------------------------------------------------
MONTE CARLO SCATTERING SIMULATION FEEDBACK:
--------------------------------------------------------------------------------
################################################################
>> Launching Scattering Simulation
################################################################
GUI Inputs successfully parsed (still need input validation)
 Calculating optical properties and Mie scattering phase function(s)...
   * Mie theoretical calculations took 5 seconds.
 Generating spatial particle distribution (random)...
   * Particle distribution has been generated.
Particle position/distribution process is complete
 Determining which particles are in each subvolume...
   * Bin recombination took 71 seconds
   * X subdivision = 1 of 149...
   * X subdivision = 10 of 149...
   * X subdivision = 20 of 149...
   * X subdivision = 30 of 149...
   * X subdivision = 40 of 149...
   * X subdivision = 50 of 149...
   * X subdivision = 60 of 149...
   * X subdivision = 70 of 149...
   * X subdivision = 80 of 149...
   * X subdivision = 90 of 149...
   * X subdivision = 100 of 149...
   * X subdivision = 110 of 149...
   * X subdivision = 120 of 149...
   * X subdivision = 130 of 149...
   * X subdivision = 140 of 149...
   * X subdivision = 149 of 149...
   * SUBVOLUME function took 9489 seconds (TOTAL).
Particle position subvoluming is complete
```

```
###### COMMENCING RAY-TRACING PROCEDURE ######
Ray-Tracing Photon 1 of 100000 (0%)...
Ray-Tracing Photon 10000 of 100000 (10%)...
   -> 1425 seconds elapsed
Ray-Tracing Photon 20000 of 100000 (20%)...
   -> 1423 seconds elapsed
Ray-Tracing Photon 30000 of 100000 (30%)...
   -> 1396 seconds elapsed
Ray-Tracing Photon 40000 of 100000 (40%)...
   -> 1435 seconds elapsed
Ray-Tracing Photon 50000 of 100000 (50%)...
   -> 1434 seconds elapsed
Ray-Tracing Photon 60000 of 100000 (60%)...
   -> 1457 seconds elapsed
Ray-Tracing Photon 70000 of 100000 (70%)...
   -> 1470 seconds elapsed
Ray-Tracing Photon 80000 of 100000 (80%)...
   -> 1460 seconds elapsed
Ray-Tracing Photon 90000 of 100000 (90%)...
   -> 1486 seconds elapsed
Ray-Tracing Photon 100000 of 100000 (100%)...
   -> 1452 seconds elapsed
Photon ray-tracing is complete
mcScatter Processing Complete!
--------------------------------------------------------------------------------
```

Figure 3.25. Representative user feedback from scattering simulation.

3.8 Monte Carlo scattering statistics

At the conclusion of the particle generation step, various simulation parameters are reported to the user via the mcScatter GUI. These include both the user-defined primary modes selected for the simulation (scattering phase function, probability distributions for angular variations, etc.) and cloud distribution parameters (both user-defined and calculated). In addition to these parameters, various statistics - recorded during the simulation and calculated as a post-processing steps - are reported. A representative example of the parametric and statistical reporting is shown in Figure 3.26.

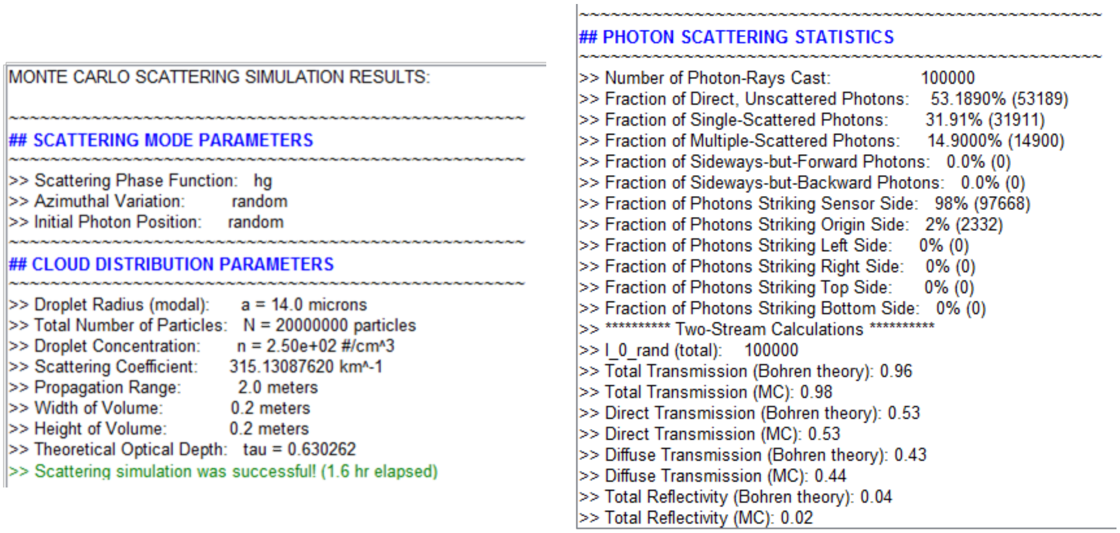

```
MONTE CARLO SCATTERING SIMULATION RESULTS:

~~~~~~~~~~~~~~~~~~~~~~~~~~~~~~~~~~~~~~~~~~~~~~~~~~~~~~~~~~~~
## SCATTERING MODE PARAMETERS
~~~~~~~~~~~~~~~~~~~~~~~~~~~~~~~~~~~~~~~~~~~~~~~~~~~~~~~~~~~~
>> Scattering Phase Function:   hg
>> Azimuthal Variation:         random
>> Initial Photon Position:     random
~~~~~~~~~~~~~~~~~~~~~~~~~~~~~~~~~~~~~~~~~~~~~~~~~~~~~~~~~~~~
## CLOUD DISTRIBUTION PARAMETERS
~~~~~~~~~~~~~~~~~~~~~~~~~~~~~~~~~~~~~~~~~~~~~~~~~~~~~~~~~~~~
>> Droplet Radius (modal):      a = 14.0 microns
>> Total Number of Particles:   N = 20000000 particles
>> Droplet Concentration:       n = 2.50e+02 #/cm^3
>> Scattering Coefficient:      315.13087620 km^-1
>> Propagation Range:           2.0 meters
>> Width of Volume:             0.2 meters
>> Height of Volume:            0.2 meters
>> Theoretical Optical Depth:   tau = 0.630262
>> Scattering simulation was successful! (1.6 hr elapsed)
```

```
~~~~~~~~~~~~~~~~~~~~~~~~~~~~~~~~~~~~~~~~~~~~~~~~~~~~~~~~~~~~
## PHOTON SCATTERING STATISTICS
~~~~~~~~~~~~~~~~~~~~~~~~~~~~~~~~~~~~~~~~~~~~~~~~~~~~~~~~~~~~
>> Number of Photon-Rays Cast:                  100000
>> Fraction of Direct, Unscattered Photons:     53.1890% (53189)
>> Fraction of Single-Scattered Photons:        31.91% (31911)
>> Fraction of Multiple-Scattered Photons:      14.9000% (14900)
>> Fraction of Sideways-but-Forward Photons:    0.0% (0)
>> Fraction of Sideways-but-Backward Photons:   0.0% (0)
>> Fraction of Photons Striking Sensor Side:    98% (97668)
>> Fraction of Photons Striking Origin Side:    2% (2332)
>> Fraction of Photons Striking Left Side:      0% (0)
>> Fraction of Photons Striking Right Side:     0% (0)
>> Fraction of Photons Striking Top Side:       0% (0)
>> Fraction of Photons Striking Bottom Side:    0% (0)
>> ********** Two-Stream Calculations **********
>> I_0_rand (total):     100000
>> Total Transmission (Bohren theory): 0.96
>> Total Transmission (MC): 0.98
>> Direct Transmission (Bohren theory): 0.53
>> Direct Transmission (MC): 0.53
>> Diffuse Transmission (Bohren theory): 0.43
>> Diffuse Transmission (MC): 0.44
>> Total Reflectivity (Bohren theory): 0.04
>> Total Reflectivity (MC): 0.02
```

Figure 3.26. Example of *mcScatter* results and statistics reported to the *mcScatter* GUI.

3.9 Monte Carlo scattering plots and results export

A number of plots can be generated by the *mcScatter* simulation software to visualize results from the ray-tracing procedure. These plots include:

- Spatial distribution of particles (see Figure 3.27)
- Particle size distribution function (see Figure 3.3)
- Scattering angle and free path distributions (see Figure 3.14 and Figure 3.28)
- Two-stream flux (see Figure 3.29 and Figure 3.30)

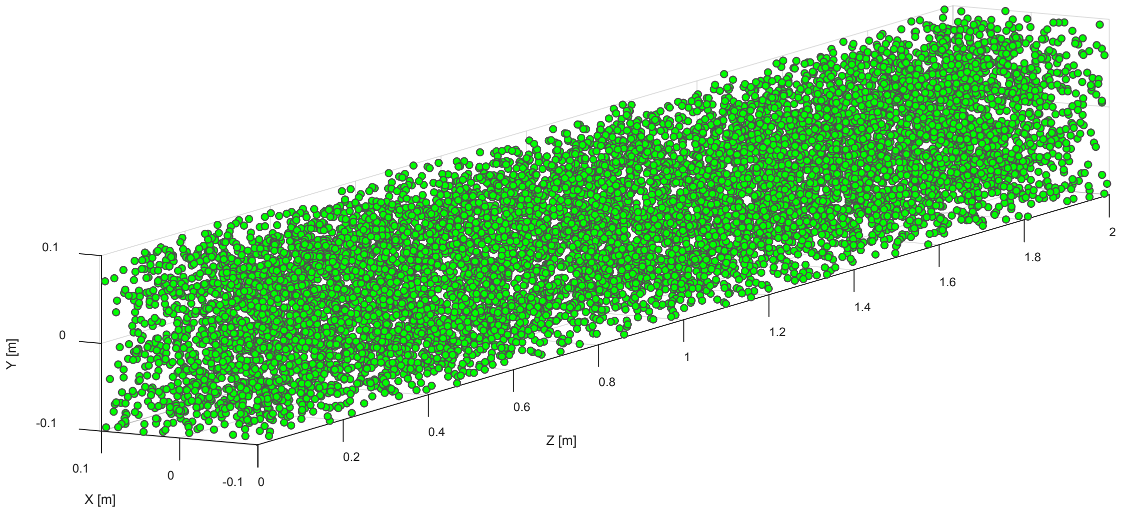

Figure 3.27. Example of spatial particle distribution plot that can be generated by mcScatter. The number of displayed particles is limited to a maximum of 10,000 and the marker color(s) are determined by particle radii.

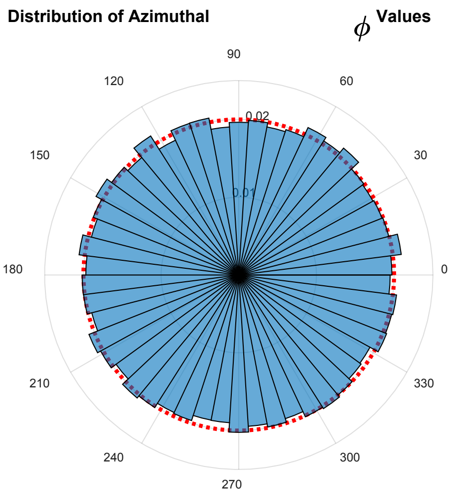

Figure 3.28. Distribution of azimuthal (not scattering) angles drawn by MC process.

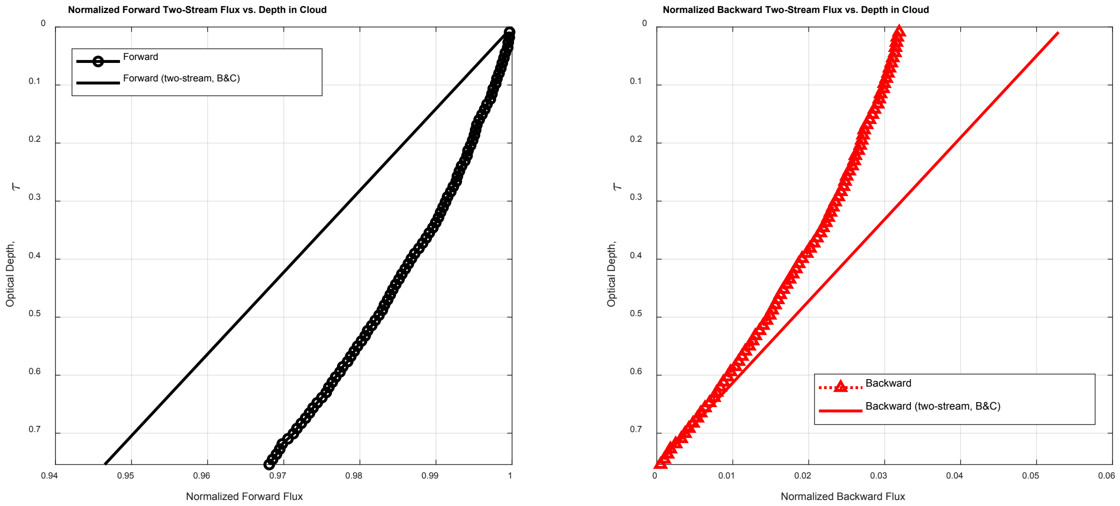

Figure 3.29. Comparison between MCRT forward and backward flux results and traditional two-stream theory (Bohren and Clothiaux, 2011).

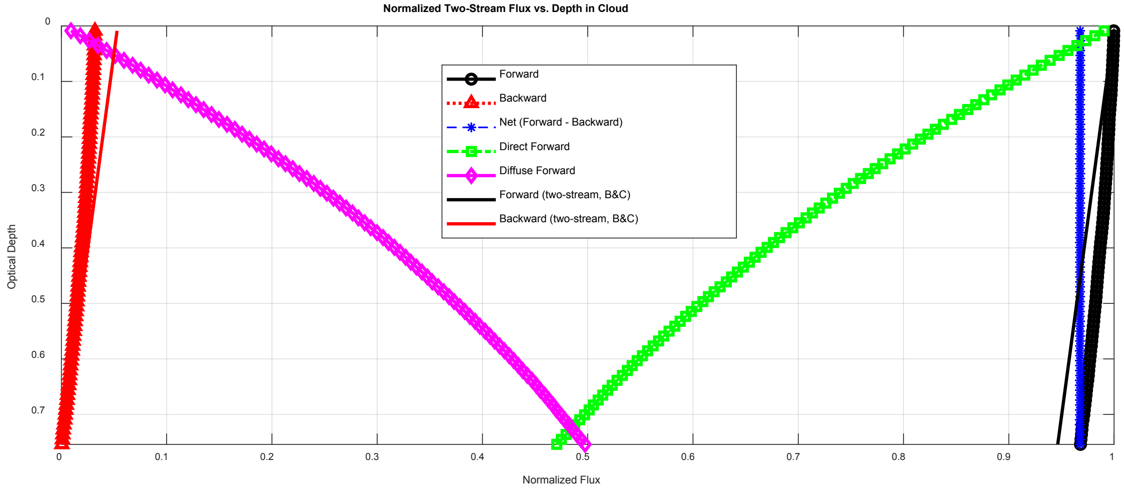

Figure 3.30. Various flux components recorded during a MCRT simulation, compared to two-stream theory.

In addition to these plots, directional flux components (e.g., direct, diffuse forward and backward) are recorded at a high spatial fidelity throughout the physical depth of the simulated cloud for export to an Excel spreadsheet. This allows for further post-processing, where the depth-dependent flux results from several simulations can be combined for better statistics. As an example, Figure 3.31 shows diffuse forward (normalized) flux curves for ten individual spatially correlated clouds, as well as their ensemble average. This demonstrates the convergence of MCRT results toward an ensemble mean once the results from at least ten cloud realizations have been aggregated.

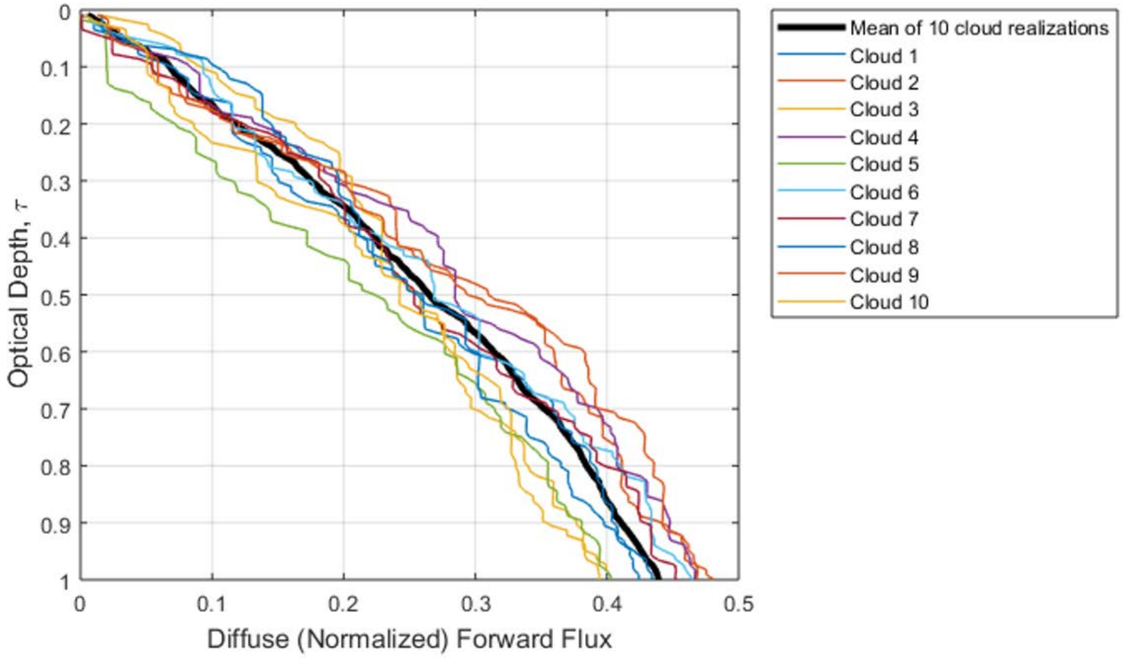

Figure 3.31. Diffuse forward flux results from ten (10) individual cloud simulations along with their mean.

4 Light scattering in a spatially-correlated particle field: Role of the radial distribution function

This chapter details predictions of direct and diffuse transmission of visible light through spatially correlated particle fields, focusing on the role of the radial distribution function in predicting deviations from radiative transfer theory for continuous media. This work was published in full form in the Journal of Quantitative Spectroscopy and Radiative Transfer.[3] [4]

4.1 Abstract

Radiative transfer through particle-laden media such as clouds can be impacted by variations in particle spatial distributions. Due to mixing and inertial effects of droplets suspended in the almost always turbulent atmosphere, cloud particles are often spatially-correlated. The correlations result in clusters and voids within the droplet field that, even when smaller than the photon mean free path, can lead to deviations from the exponential extinction law. Prior work has numerically investigated these departures from exponential attenuation in absorptive media; this work extends those results for a scattering medium. The problem is explored with a Monte Carlo Ray Tracing (MCRT) program capable of tracking light attenuation through both perfectly random (uncorrelated) and spatially correlated collections of scatterers and/or absorbers. The MCRT program is favorably compared to two-stream flux equations, and numerical exploration of the pure-absorption case is used to determine the sampling statistics necessary to characterize radiative transmission within the numerical simulation. Light transmission through fields of spatially-correlated, non-absorbing, scattering particles is explored. Particles are distributed following a Matérn Point Process, which allows cluster strength and size, as well as the usual variables of particle scattering cross section and number density to be varied. The results show that the degree of non-exponential attenuation is determined by the magnitude and shape of the radial distribution function, which describes correlations in discrete (non-continuous) particle distributions. Parametric studies revealed that the number of clusters and cluster radius, factors in the Matérn radial distribution function, impact direct, diffuse and backward radiative transfer. The Matérn RDF is shown to be consistent with a previous "cloudlet" approach, providing a bridge between the analytical cloudlet model and continuous correlation function approaches.

---

[3] Packard, C.D., Larsen, M.L., Cantrell, W.H., Shaw, R.A. "Light scattering in a spatially-correlated particle field: Role of the radial distribution function." Journal of Quantitative Spectroscopy and Radiative Transfer, 236, 106601 (2019). https://doi.org/10.1016/j.jqsrt.2019.106601

[4] © 2019 Elsevier Ltd. Used with permission.

4.2 Introduction

Radiative transfer through a spatially correlated medium results in a distinct behavior, essentially because photons propagate further in void regions, and experience stronger extinction in dense regions, relative to a homogeneous medium (Marshak and Davis, 2005). The problem has a multitude of applications, ranging from the cloudy atmosphere to biological and energy-generation systems (Davis and Marshak, 2004; Larsen and Vasques, 2011; Zoller et al., 2018). In this work, we consider distributions of discrete particles, with the atmospheric context as our motivating problem.

When spatial correlations are present in the positions of perfectly absorbing particles, deviations from the usual exponential extinction emerge (Kostinski, 2001; Larsen and Clark, 2014; Frankel et al., 2017); these deviations can be both super- or sub-exponential, depending on the nature of the spatial correlations (Shaw et al., 2002a). Spatial correlations between particles within a turbulent flow can be created by several mechanisms, including inertial clustering (Reade and Collins, 2000) and turbulent mixing (Warhaft, 2000). For example, mixing and entrainment in atmospheric cloud boundaries leads to pockets of cloudy and clear air on spatial scales ranging from km to mm (Davis et al., 1999; Shaw, 2003). Recent work has suggested that, at least in the absorbing-particle problem, the relevant clustering metric is the radial distribution function (Shaw et al., 2002a; Frankel et al., 2017).

How does the situation change when we consider diffuse radiation in a scattering medium? Previous results were for absorbing particles or, equivalently, extinction of a direct beam, and we might expect that the situation with scattering is more complex. Nevertheless, the key geometrical argument that suggests a mechanism for the non-exponential behavior should be general (see, e.g., Kostinski 2001; Kostinski 2002), and a natural follow-on question to the previous numerical work on absorbing clouds is to determine whether the radial distribution function can also capture the essential physics at play in a medium containing purely scattering particles.

We address the problem using the ray tracing Monte Carlo radiative transfer approach that has been shown to be consistent with standard radiative transfer (e.g., Bohren and Clothiaux, 2011). This should be consistent with the findings of Mishchenko (Mishchenko, 2006, 2008) that even in a correlated medium the classical radiative transfer equation holds, as long as high-order scattering paths can be neglected and assumptions of ergodicity and spatial uniformity are valid. To limit the scope of the work, we take as context the transport of visible light in a cloud of water droplets as found in atmospheric applications (e.g., wavelength ~ 550 nm and droplet radius ~ 14 μm). In this regime, absorption is extremely weak and therefore in the remainder of this work we take the single scatter albedo to be exactly unity. Furthermore, we consider the regime in which multiple scattering does not become dominant (e.g., optical thickness of order unity).

There are several reasons motivating the use of Monte Carlo Ray Tracing (MCRT) within a field of discrete particles rather than the more standard (and computationally efficient) photon-path-distribution function. At a fundamental level, we are exploring radiative transfer at scales on which the notion of a continuously-distributed system becomes ill-defined, and where discreteness effects such as sampling or ‘shot’ noise are relevant. We therefore take the direct approach of explicit representation of each particle. Another primary motivation is generality and flexibility when it comes to representing radiative transfer in a real system, such as the Pi Cloud Chamber (Chang et al., 2016). In that case, we must consider sampling of a dilute medium within a confined geometry. We find the possibility of future comparison between numerical computations of direct and diffuse radiation and measurements of these fields in a laboratory cloud chamber appealing; in particular, we have in mind the Pi Cloud Chamber, which is able to produce optical thicknesses of order unity (Chang et al., 2016). For example, the assumptions drawn into focus by Mishchenko merit direct experimental assessment, especially the insight that averaging scales play a central role (Mishchenko, 2006). Besides the finite-sample effects, the explicit, discrete-particle approach allows for simpler implementation of boundary conditions. The generality of this approach will also allow the method to be applied to conditions in which clustering may not be isotropic, such as in turbulent Rayleigh-Bénard convection. Eventually, it would be of interest to compare the discrete approach to the path-distribution approach for dilute, finite-size systems.

In this work, perfectly random and correlated spatial particle distributions (generated using a Matérn Point Process model, having a known closed-form radial distribution function) are generated within a simulation volume. Then, a Monte Carlo Ray Tracing code – capable of simulating scattering events either through full Mie computation or more approximately through the Henyey-Greenstein phase function – propagates individual photons through the simulation volume, tracking direct, diffuse forward, and diffuse backward radiative fluxes from an initially collimated beam of photons entering the simulation volume at normal incidence.

The paper proceeds as follows: In Sec. 2 we define the radial distribution function (RDF) and introduce the Matérn process as an analytic model for introducing particle spatial correlations via the RDF. In Sec. 3 we describe the Monte Carlo Ray Tracing (MCRT) code that is used to simulate light propagation through a medium containing discrete particles. In Sec. 4 we present results of the simulations, showing departure from propagation through a uniformly random particle field, and we interpret the results in the context of the RDF. In the concluding section we discuss the results and their possible implications for atmospheric radiative transfer.

4.3 Exploring the Matérn cluster process

4.3.1 The influence of particle clustering on transmission through a scattering medium

As noted above, deviations from exponential attenuation in traditional radiative transfer theory are expected when the particles in the medium are spatially correlated (Kostinski, 2001). Inertial particles in a turbulent fluid (e.g., cloud droplets in the atmosphere) provide one physical scenario where these spatial correlations are known to exist (Saw et al., 2012; Larsen et al., 2018). Previous work (Shaw et al., 2002a; Larsen and Clark, 2014; Frankel et al., 2017) suggests that the deviation from exponential behavior in such media may depend on the radial distribution function describing that statistical structure of particulate clustering.

The radial distribution function $g(r)$ of a particle-laden medium quantifies the scale-localized clustering of the particles in the medium (Landau and Lifshitz, 1980; Reade and Collins, 2000; Shaw et al., 2002a; Saw et al., 2012; Larsen and Shaw, 2018; Larsen et al., 2018). It can be readily understood through its relation to the joint probability of finding a particle in volumes dV_1 and dV_2, both separated by distance r, in a system with global particle number density n:

$$p_{(1,2)}(r) = (ndV_1)(ndV_2)\, g(r)\,. \tag{25}$$

Algorithmically, $g(r)$ can be understood as the observed number of particle pairs separated by distance $r \pm \delta r$ relative to the number of particle pairs expected at the same distance for a perfectly random population (Poisson distributed at all scales).

Testing the radial distribution function dependence on radiative transmission through a purely *scattering* medium will be facilitated by generating scatterer positions within the simulation volume via a method that produces a known, closed-form radial distribution function. Particle positions in a turbulent flow-field in steady-state are often modelled with a decaying power-law RDF that is dependent on the Stokes number (Chun et al., 2005). The construction of a simulation volume of scatterers with a power-law radial distribution function presents at least two challenges; (i) $g(r \to 0) = \infty$, which is physically impossible, and (ii) the lack of a simple algorithm to place particles in a way that replicates a power-law radial distribution. Additionally, there are some physical mechanisms that cause clustering that are not expected to have a power-law form like particle charging (Lu et al., 2010) or convective organization (Barker, 1992). For this study, in lieu of generating clustered particle spatial locations for a specific physical mechanism (e.g., running turbulence simulations), we instead take a more general approach. We have opted to utilize the Matérn cluster process to distribute scattering particles throughout the simulation volume, which has the advantage of providing an analytical form for the RDF that can be explicitly adjusted to change the scale and magnitude of clustering.

The Matérn cluster process (Matérn, 1972, 1986; Martínez and Saar, 2002) is a Neyman-Scott point process model that has several advantageous features for this work: (i) it has an analytically straightforward closed-form expression for its radial distribution function, (ii) it has a fundamental characteristic length-scale R, and (iii) it is numerically easy to simulate. For spatial scales larger than $2R$, the Matérn cluster process radial distribution function is the same as that for a perfectly random distribution. Additionally, like power-law RDFs, the RDF of the Matérn cluster process has a monotonic decrease with increasing spatial scale (but does not diverge at small distances like power-law RDFs).

4.3.2 Construction and properties of a Matérn cluster process

All Neyman-Scott point process models are constructed in the same way; (i) some number of "parent" particles N_p, are distributed in a perfectly random manner throughout the cloud volume V with spatial density N_p/V, (ii) some discrete probability distribution function with a specified mean λ_D is sampled to assign how many "daughter" particles will be associated with each parent particle, and (iii) some continuous probability density function is sampled to determine how far each daughter particle is placed from its associated parent particle. The final collection of particles will be the ensemble of daughter particles generated through this process. For the Matérn cluster process, the discrete probability distribution in step (ii) is a Poisson distribution and the continuous probability distribution in step (iii) is designed to place the daughter with uniform probability anywhere within a sphere of radius R around the associated parent particle. Ultimately, a statistically homogeneous but clustered distribution with approximately $(N_p \cdot \lambda_D)$ total particles is generated. More detail including a figure demonstrating this construction process in two-dimensions can be found in Larsen et al. (2014). For this system, the resulting radial distribution function $g_{3D}(r)$ for a 3-dimensional Matérn cluster process can be written (Chiu et al., 2013; Larsen et al., 2014)

$$g_{3D}(r) = \begin{cases} \dfrac{3V}{8\pi R^6 N_p}\left(R - \dfrac{r}{2}\right)^2 \left(2R + \dfrac{r}{2}\right) + 1 & (r < 2R) \\ 1 & (r \geq 2R) \end{cases} . \tag{26}$$

It is important to note here that with a constant cloud volume, the Matérn radial distribution function (RDF) given by Eq. (26) is dependent only on the number of parent clusters and the cluster radius (N_p and R, respectively), and does not vary with the average number of particles per cluster, λ_D. The dependence of the Matérn RDF, $g(r)$, on N_p and R is illustrated in Figure 4.1.

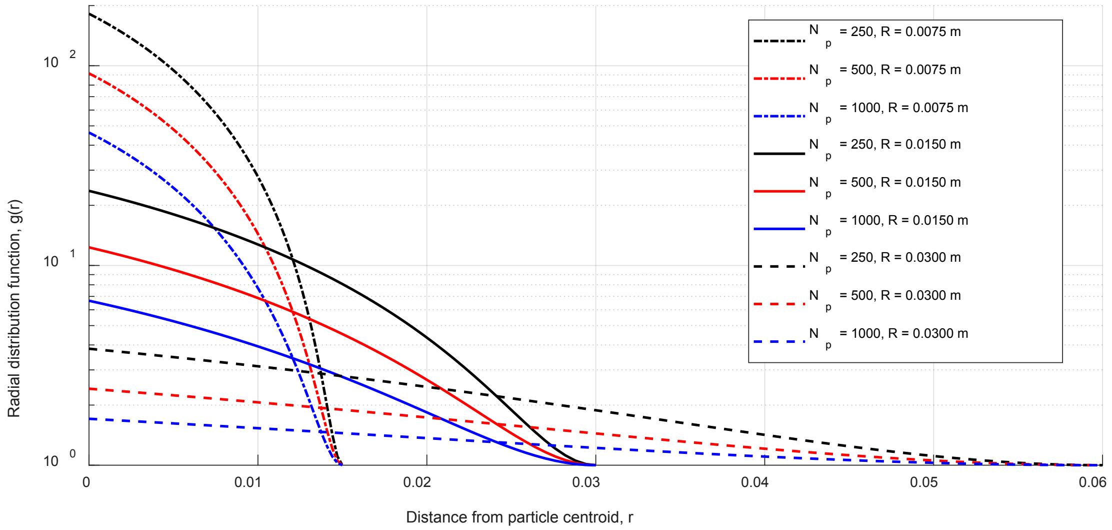

Figure 4.1. Dependence of theoretical Matérn radial distribution function (RDF) on number of clusters, N_p, and cluster radius, R, given the 0.08 m^3 cloud volume used in our simulations. Note that at distances r greater than $2R$ the RDF illustrates statistical structure equivalent to an uncorrelated distribution ($g_{3D} = 1$ for $r > 2R$).

4.4 Description and validation of Monte Carlo ray tracing code

4.4.1 Overview of the MCRT code ('mcScatter')

A Monte Carlo scattering simulation code, 'mcScatter', was created to explore the role that spatial correlations play in radiative transfer through a light-scattering medium such as an atmospheric cloud. The general structure of our MCRT code was motivated in part by a desire to eventually validate the numerical results with experiments in a cloud chamber facility (Chang et al., 2016). The virtual laboratory of a computer simulation allows for the relaxation of the physical constraints of an actual cloud chamber (such as particle clustering limits and experimental setup restrictions) to predict experimental results and develop an effective methodology for measuring parameters of interest.

To match experimental conditions potentially realizable in the chamber, the numerical work that follows is limited to a spatial domain of 2 m x 0.2 m x 0.2 m (inspired by a realistic optical path through the chamber) and total optical thickness of order $\tau^* \sim 1$. Our MCRT code, described in greater detail in chapter 3, allows for the specification of optical wavelength, particle size, complex index of refraction and many other boundary conditions. In this paper we focus our analysis in the visible spectrum with an optical wavelength of 550 nm, and examine relatively large but realistic cloud droplet sizes (e.g., radius ~ 14 μm) based on previous cloud chamber measurements (Chang et al., 2016; Packard et al., 2018). The resulting size parameter focuses our analysis on the forward-scattering regime with a single scatter albedo of 1 and a scattering efficiency of $Q_{sca} \approx Q_{ext} \approx 2$.

Approaches exist for addressing this problem directly from Maxwell's equations (Mishchenko, 2008; Mishchenko et al., 2016); however, direct use of methods like the superposition *T* matrix method remain impractical for systems with large numbers of particles like clouds. Previous work (Cairns et al., 2000; Petty, 2002; Davis, 2006) has led to the development of heuristic models to quantify the radiative transmission through inhomogeneous particle-laden media via a variety of methods. In Sec. 5 we discuss the ability of these heuristic techniques to predict results similar to those found by our MCRT analysis.

Others have investigated such heterogeneous systems through the development of numerical Monte-Carlo simulations (Marchuk et al., 1980; Marshak and Davis, 2005); a clear discussion can be found in Bohren and Clothiaux (2011) but numerous relevant publications can be found on the subject (Plass and Kattawar, 1968; Danielson et al., 1969; Collins et al., 1972). The Monte Carlo method (Sobol' et al., 1974) has often been applied to investigate radiative transfer problems where closed form solutions are challenging or impossible, and a detailed description of its application to inhomogeneous media has been presented (Cole, 2005).

These numerical methods typically explore radiative transmission without assigning physical locations to particles by stochastically modeling the free-path distribution between successive scattering interactions. In these simulations, the distances that photons travel before redirection are obtained via random draws from an analytic (usually exponential) free-path cumulative density function (CDF) based on the scatterer concentration of the medium. Modifications to propagation directions are obtained via random draws from an appropriate scattering phase-function (e.g. Henyey-Greenstein or Mie) describing the angular distribution of light intensity scattered by a particle for a given wavelength. This process of computing distance traveled prior to scattering, choosing a scattering angle, and re-computing distance traveled is repeated until all rays cast into the medium exit (based on specified "wall" boundary conditions).

In a ballistic 'photon' simulation (Shaw et al., 2002a; Larsen and Clark, 2014), particles are placed in a volume at specified locations, and numerous rays are cast into the scattering medium (Frankel et al., 2016; Banko et al., 2019). Each ray is traced until it either exits the cloud on the other side unscattered (direct radiation) or its path intersects a particle (i.e., a geometric "collision"). The path of a scattered photon proceeds similar to those in the standard Monte Carlo algorithm outlined above; the new propagation direction is chosen from a phase function and subsequent scattering events can occur until the particle leaves the computational volume. Details associated with the computational implementation of this model can be found in chapter 3.

This type of ballistic photon simulation allows particles to be placed anywhere in the volume to determine the impact of their spatial correlations on radiative transfer, but this benefit comes at the cost of recording and tracking a multitude of particle positions and collision locations. Though other approaches may resolve continuous media better (Mishchenko et al., 2016), ballistic photon simulations are especially well-suited for spatially-correlated media where analytic extinction CDFs may not be known (Shaw et al., 2002a). Our ballistic MCRT simulation extends the related numerical approach presented in Shaw et al. (2002) and Larsen and Clark (2014) to a scattering domain. These simulations employ explicit positions for each individual particle within the medium, thus allowing for geometric ray-tracing to explore an arbitrary inter-scatterer distribution, rather than utilize a blind draw from a static (known) distribution function.

The simplest limiting case of this MCRT analysis occurs when simulating a cloud of monodisperse particles identically and independently distributed randomly within the simulation volume (see top panel of Figure 4.2). Such a homogeneous system can serve as a control, where results can be validated against standard radiative transfer theory and expected analytic results. After validation on this simple (homogeneous) system, the MCRT code can be used to analyze virtual clouds comprised of non-uniform particle locations generated with the Matérn process described in the previous section (with an example of such a clustered distribution shown in the bottom panel of Figure 4.2).

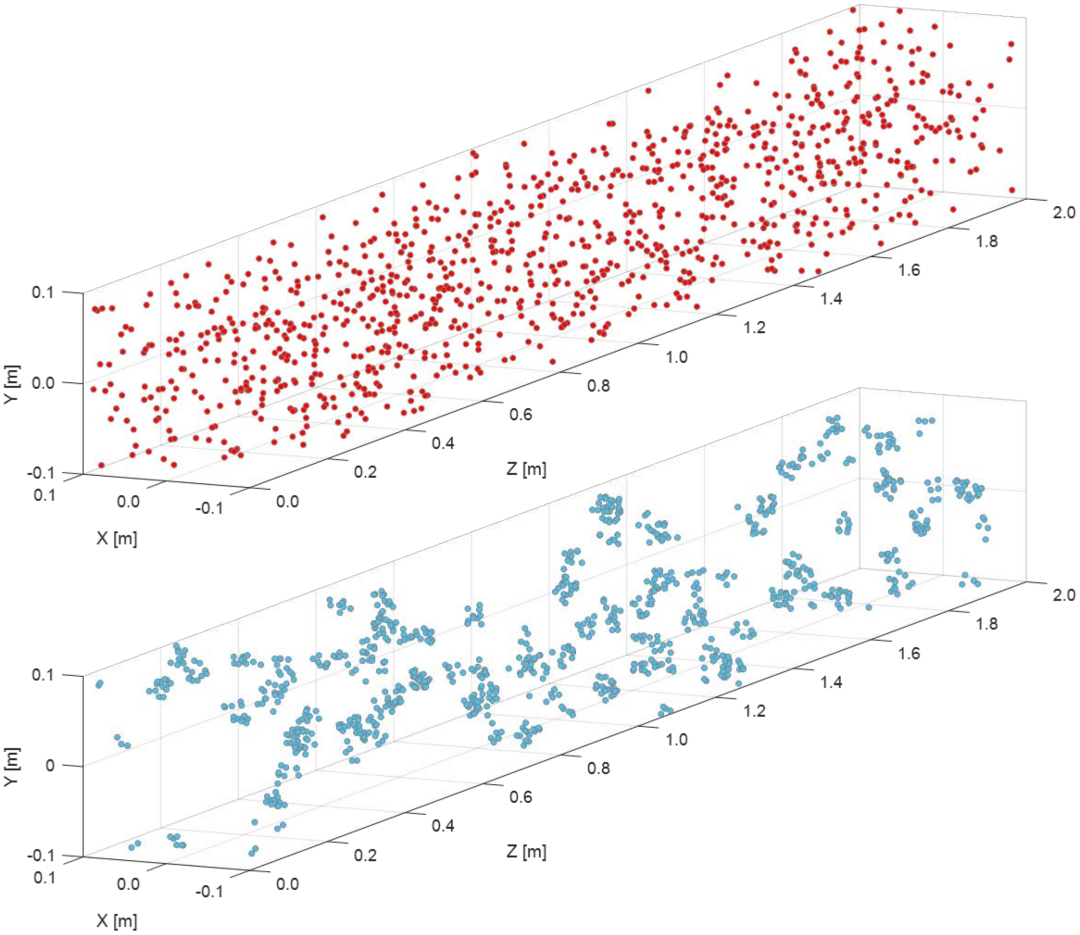

Figure 4.2. Comparison between a homogeneous, uniform random particle distribution (top) and a Matérn-generated clustered distribution (bottom). Total cloud volume illustrated here and used for all scattering simulations in this works is 0.2 m x 0.2 m x 2.0 m (0.08 m^3).

Rays (or ‘photons’) are initialized at uniformly-random (*x, y, z = 0*) positions and cast in a normally-incident collimated beam through one side of the volume, which contains numerous particles at specified (stationary) spatial locations. Intersections between these rays and particles create scattering events that modify the direction of each photon path; new ray directions are determined from the scattering phase function. Figure 3.13 illustrates a subset of rays from a typical simulation result. In the case of cloud droplets with typical diameters larger than the wavelength of visible light, the resultant size parameter yields a scattering pattern that is forward-dominant.

The most rigorous way to calculate the scattering phase function is through Mie theory, where particles are considered as homogenous dielectric spheres interacting with an incident plane wave of light. However, it is convenient to have an analytic formula that approximates the actual scattering phase function shape, especially at this initial stage where details of the scattering are not expected to be as important for the scientific questions being explored. The Henyey-Greenstein phase function, essentially a probability density function (PDF) of scattering angle, is a common surrogate for the actual phase function (Henyey and Greenstein, 1941). Its analytic form allows it to be integrated to calculate a closed-form cumulative density function (CDF). Its parametric nature allows it to be employed rather simply, with sufficient accuracy for many applications (Thomas and Stamnes, 1996; Ishimaru, 1997; Bohren and Clothiaux, 2011). The *mcScatter* software introduced here makes both Mie and HG (Henyey-Greenstein) phase functions available for scattering simulations.

As numerous rays are traced through the scattering medium, the locations of particle collisions and all individual ray segments are recorded. Direct and diffuse flux is recorded at a high spatial fidelity throughout the cloud depth, both backward and forward. This allows for direct, diffuse and total forward irradiance as well as backward irradiance to be calculated at many places within the cloud volume. Further details regarding the implementation of our scattering code beyond the basic phenomenological approach explained in this subsection can be found in chapter 3.

4.4.2 Validation of MCRT direct beam extinction through a homogeneous uncorrelated medium

Before analyzing the impact of a spatially-correlated particle field on light scattering, we first ensured the fidelity of our MCRT code for non-scattering particles that are distributed with uniform probability (no spatial correlations). Given initial downward irradiance on a cloud top, F_0, the direct (unscattered) irradiance $F_{direct}^{\downarrow}$ is an exponential function of optical depth into the medium. By normalizing the direct, unscattered irradiance by the initial downwelling irradiance (where $\tau = 0$) we get an expression for the normalized direct flux (Bohren and Clothiaux, 2011) which can be written as

$$\varphi_{direct}^{\downarrow} = \frac{F_{direct}^{\downarrow}}{F_0} = exp(-\tau) \ . \qquad (27)$$

To calculate normalized direct flux with our MCRT code, we uniformly divide the expected total optical thickness into numerous "slabs". We represent total optical thickness as ($\tau^* = c\sigma z$), where c is the (number) concentration of scatterers, σ is the effective scattering cross section of each scatterer, and z is propagation depth through entire cloud. We then cast N_{ray} rays into the particle-laden medium and trace each ray to determine how may slabs are traversed before an absorbing particle is encountered. The number of rays passing each slab boundary is dependent on the total number of rays initially cast, but by dividing the tabulations by N_{ray} we compute a normalized optical depth-dependent direct flux. These direct beam extinction results were compared to the expected exponential decay to validate that portion of our MCRT code. One such comparison, performed for a monodisperse cloud with 14 μm radius particles and a total optical thickness (τ^*) of 1, is shown in Figure 4.3. The simulation results matched the theoretical predictions exactly, with the expected exponential decay appearing linear due to the logarithmic y-axis.

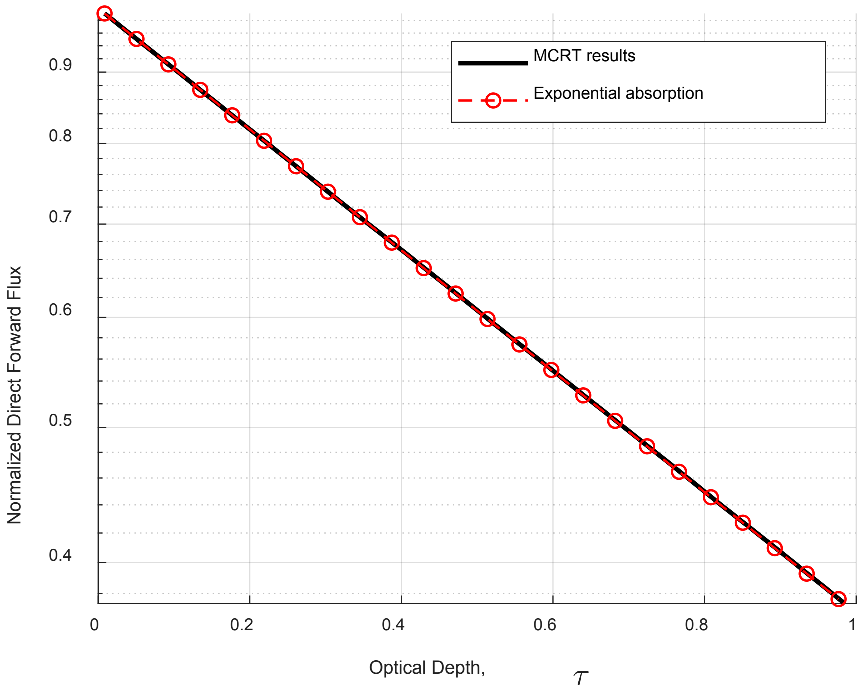

Figure 4.3. Normalized direct, unscattered flux comparison between theoretical (red circles) and Monte Carlo results (black solid line) for a monodisperse cloud with 14 μm radius particles and τ^* of 1. Note that the vertical axis employs logarithmic spacing to illustrate exponential absorption.

4.4.3 Comparison of MCRT results to two-stream theory

One commonly made simplification is the idealization of radiative transfer into only two propagation directions, forward and backward (Thomas and Stamnes, 1996; Bohren and Clothiaux, 2011). This two-stream approximation is most accurate in the case of isotropic scattering where the phase function is uniform but can be used for anisotropic scattering as well with reasonable accuracy (Thomas and Stamnes, 1996). Thomas and Stamnes (1996) state that, when Henyey-Greenstein phase function and two-stream approximations have been combined and compared to other (more accurate) methods, the resulting deviations are typically less than 2.5%, especially when the solar illumination is close to normally incident. For more information on the compromises made when using the Henyey-Greenstein phase function and multi-stream approximations the reader is referred to other works (Li et al., 2015). In order to place our MCRT results in a context that will be familiar to most readers, in this subsection we compare them to the two-stream theory and then to Monte Carlo results presented in the textbook by Bohren and Clothiaux (2011).

Using the Henyey-Greenstein phase function and periodic boundary conditions, each ray cast into the scattering medium continues moving either forward or backward until it terminates at the top or bottom of the simulated cloud. By normalizing the number of rays that cross each layer boundary (in either direction) by the total number of rays cast, the diffuse forward and backward flux components were computed. These MCRT simulation results were then compared to corresponding expressions from two-stream theory, such as the normalized diffuse forward flux given as (Bohren and Clothiaux, 2011)

$$\varphi_{diffuse}^{\downarrow} = \frac{D_{\downarrow}}{F_0} = \frac{1 + (\tau^* - \tau)\left(\frac{1-g}{2}\right)}{1 + \tau^*\left(\frac{1-g}{2}\right)} - exp(-\tau) \tag{28}$$

and the normalized diffuse backward flux, expressed as

$$\varphi_{diffuse}^{\uparrow} = \frac{D_{\uparrow}}{F_0} = \frac{(\tau^* - \tau)\left(\frac{1-g}{2}\right)}{1 + \tau^*\left(\frac{1-g}{2}\right)} \ . \tag{29}$$

In these normalized flux expressions, g refers to the asymmetry parameter, a scalar characterization of the degree of anisotropy calculated as the mean cosine of the scattering angle. Figure 4.4 shows a comparison between two-stream theory curves for normalized forward and backward flux components and their Monte Carlo simulation counterparts. In this example, particles with a radius of 14 μm and a number density (n) of 400 cm^{-3} were used to create a homogeneous monodisperse random distribution with a total optical thickness (τ^*) of 1 with an asymmetry parameter (g) of 0.85.

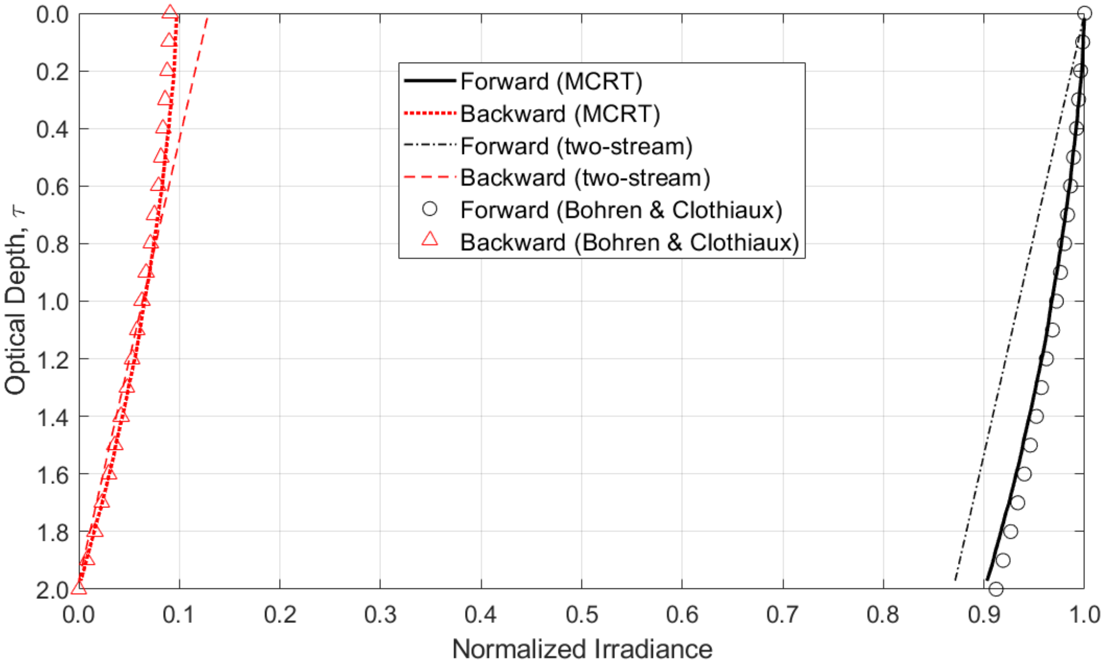

Figure 4.4. Flux comparison between two-stream theory and Monte Carlo (MCRT) results, both forward flux (rightmost black curves) and backward flux (leftmost red curves). Note that at their most divergent, the two-stream and MCRT flux curves differ by 2-3%. Also shown for validation purposes are the Monte Carlo results (circle and triangle symbols) given in Bohren and Clothiaux (2011), see top panel of their Fig. 6.10.

The discrepancies evident in Figure 4.4 between our MCRT results and two-stream theory are consistent with those suggested in Thomas and Stamnes (1996) and shown in a similar comparison of two-stream theory with Monte Carlo by Bohren and Clothiaux (2011). These depth-dependent differences are due to the fact that two-stream theory approximates radiative transfer by neglecting the details that a full angular scattering solution includes. For validation purposes, the Monte Carlo results from Bohren and Clothiaux (2011) are included in Figure 4.4 for reference (circle and triangle symbols). We hypothesize that the slight differences between the Bohren and Clothiaux results and the MCRT results presented here are likely a result of details related to horizontal fluxes, such as the domain geometry and side-wall boundary conditions. As a further test, we used our MCRT code to simulate isotropic scattering ($g = 0.0$) and found excellent agreement with the transmission and reflectivity predictions of two-stream theory.

4.4.4 Simulation design for correlated random media

We emphasize here that the cluster sizes used in our analysis are smaller than the mean free path (as defined for a homogeneous medium), and therefore are not necessarily captured by a macroscopic, spatially varying mean free path. The radial distribution function depends on N_p and R, while the expected cloud optical thickness is $N_P \lambda_D V^{-1} Q_{sca} \pi a^2 L$ and thus depends on N_p, λ_D and particle radius a. It is therefore possible to explore the scattering problem under the constraint of fixed total optical thickness τ^* for varying input parameters, including those that directly influence the radial distribution function and therefore the magnitude and scale dependence of particle clustering.

Multiple particle cloud realizations were stochastically generated for each set of input parameters, and the results from each individual cloud scattering simulation were averaged together to form the reported (mean) optical depth-dependent fluxes. Due to the small cross sectional area being illuminated (0.2 m x 0.2 m), we found it necessary to analyze ten (10) unique clouds to compile trustworthy average flux results (see Figure 3.31). Consequently, all results shown in this work are the result of averaging the depth-dependent flux curves of at least ten unique cloud realizations, each of which was probed with 100,000 rays (see Figure 3.14).

4.5 Results

4.5.1 Impact of particle clustering on depth-dependent flux

In this work we investigate both the direct and diffuse radiative transfer (forward and backward) in a purely scattering but correlated random medium to determine expected deviations from commonly used radiative transfer predictions for a uniform, homogeneous medium. The problem depends on four parameters: N_p, R, λ_D and particle radius a. While the radial distribution function contains only N_p and R, the expected cloud optical thickness depends on N_p, λ_D and a. For our analysis we varied these four input parameters while constraining the total optical thickness τ^* to determine the influence of particle size, clustering and the radial distribution function.

We performed numerous scattering simulations through both uncorrelated and spatially-correlated monodisperse cloud distributions to explore the impact of spatial correlations on optical-depth-dependent irradiance. Mean optical depth-dependent irradiances, including direct and diffuse forward flux as well as backward flux, were calculated as a function of distance through both homogeneous and spatially correlated clouds. An example illustrating these various flux components is shown in Figure 4.5, with the solid black line indicating the homogeneous case and the red dotted line indicating a Matérn-clustered scenario with ($N_p = 500$, $\lambda_D = 64000$, $R = 0.015$ m). We note that the corresponding RDF is included as the dot-dashed red curve in Figure 4.1.

When we consider the unscattered, direct flux traversing a simulated cloud, as shown in the top panel of Figure 4.5 where τ increases downward on reversed vertical axis, we see that direct transmission is increased when spatial correlations exist in the particle-laden medium. Previous publications have shown that propagation through a spatially-correlated medium deviates from expectations of Beer-Lambert-Bouguer exponential attenuation (Kostinski, 2001; Shaw et al., 2002a; Matsuda et al., 2012; Larsen and Clark, 2014; Frankel et al., 2017). Our Monte Carlo simulations, operating on clouds generated using a Matérn-process radial distribution function for particle positions, show this expected increase in direct flux through a field of particles. For the example in Figure 4.5, at optical depth $\tau = 1$, an increase of direct transmission from 37% to more than 40% is observed in the Matérn-clustered results.

(a) Direct (Normalized) Forward Flux

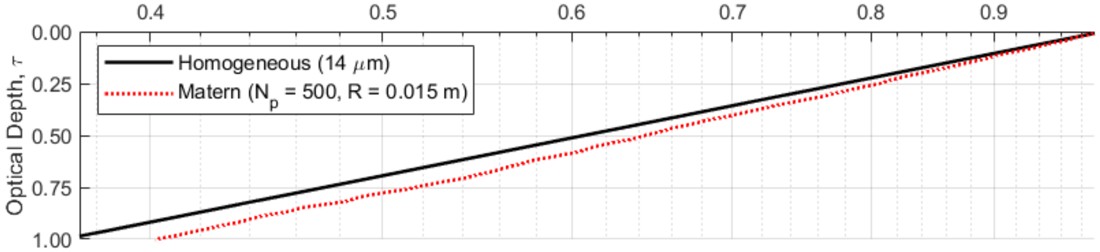

(b) Diffuse (Normalized) Forward Flux

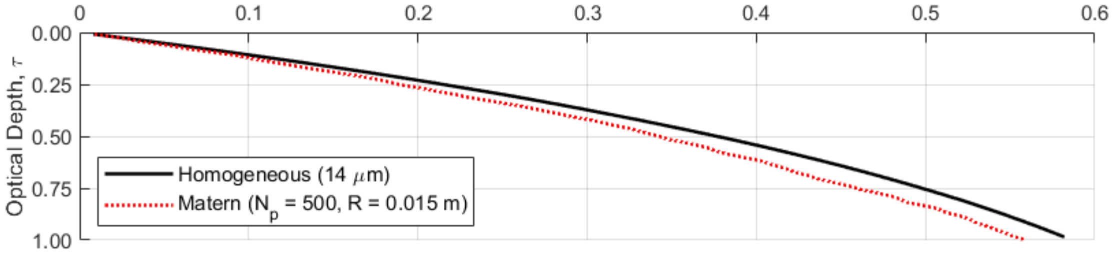

(c) Backward (Normalized) Flux

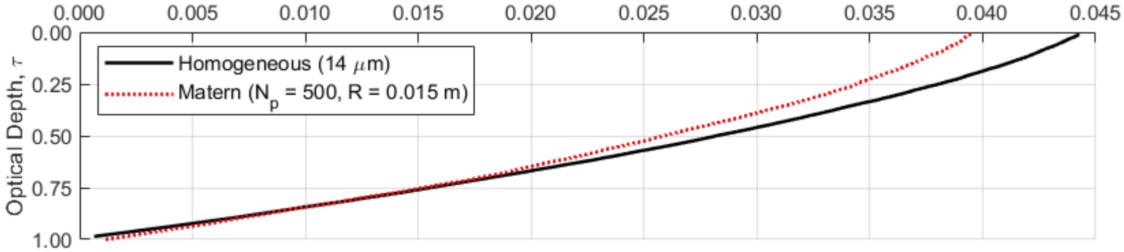

(d) Total (Normalized) Forward Flux

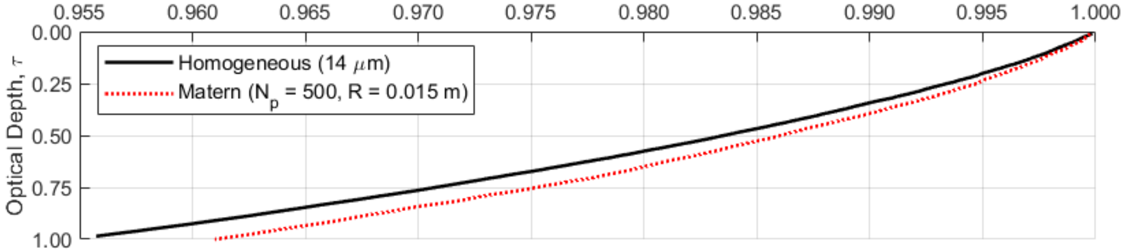

Figure 4.5. Impact of particle clustering on depth-dependent flux curves as computed by our MCRT scattering simulation. Both homogeneous and Matérn correlated results were obtained from monodisperse (14μm particle radius) cloud realizations with a total optical thickness, τ^*, of 1. Cluster radius, R, is 0.015 m and the number of cluster parents (N_p) is 500. The average number of particle per parent cluster (λ_D) is 64,000. Note that in this and subsequent figures, the independent variable optical depth (τ) increases downward on the reversed vertical axis, starting from the top of the cloud at $\tau = 0$ and finishing at the exit point at the bottom of the cloud ($\tau = 1$).

Note that while panel (a) of Figure 4.5 shows an increase in direct transmission for the clustered compared to the unclustered distribution, panel (b) indicates a similar *decrease* in diffuse forward flux. Panel (c) indicates that, for this case, the amount of backward flux is slightly impacted by the existence of spatial correlation. Together these results signify that the difference in total forward flux (direct plus diffuse) due to spatial correlation, shown in panel (d) to be less than 0.5%, is only distinguishable when very tight normalized flux axis limits are chosen. In other words, when comparing only the mean normalized irradiances that would be detected at the bottom of the cloud, little difference would be measured, although presumably a radiance measurement separating direct from diffuse would reveal the distinction. Decreased direct attenuation is not totally compensated for by increased diffuse forward radiation, though they counterbalance to dampen the effect of particle clustering.

4.5.2 Impact of Matérn RDF parameters on depth-dependent flux

The Matérn RDF expression listed in Eq. (26) demonstrates dependency on both the number of parent clusters (N_p) and cluster radius (R). To test the hypothesis that these two parameters are the primary contributors to changes in depth-dependent flux for Matérn spatially correlated particle distributions, we simulated additional clustered clouds where these inputs were unchanged. The number of Matérn clusters was held constant at $N_p = 500$, and the cluster radius was fixed at $R = 0.0075$ m. While keeping N_p and R constant, we varied the monodisperse particle radius (e.g., 9.9 μm, 14 μm and 19.9 μm) and changed the mean number of particles per cluster accordingly (e.g., $\lambda_D = 128000$, 64000 and 32000 respectively) to maintain a total optical depth of $\tau^* = 1$ for all simulated clouds. To ensure that we limited our exploration to parameters of interest, we enforced a constant asymmetry parameter and scattering efficiency (e.g., $g = 0.85$, and $Q_{sca} = 2.0$, respectively) in spite of changing particle radius.

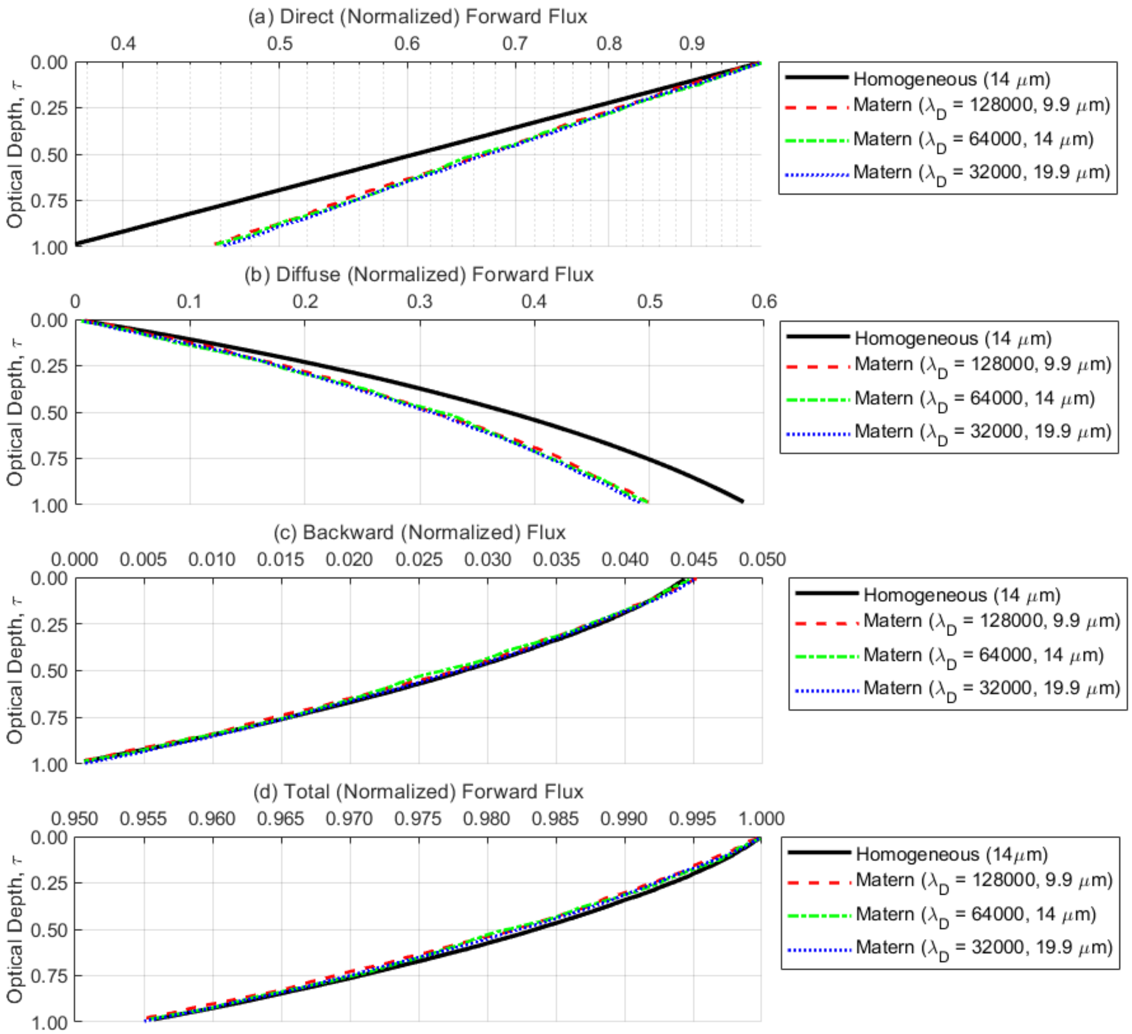

Figure 4.6. Optical depth-dependent flux curves for a variety of Matérn-generated cloud distributions, with homogeneous particle distribution results shown for comparison. Note that in all three Matérn scenarios, the density of clusters and cluster radius are constant (e.g., $N_p = 500$ and $R = 0.0075$ m, respectively). Changes in monodisperse particle radius and number of mean particles per cluster (λ_D) have almost no impact on depth-dependent flux curves when N_p and R are held constant.

As can be seen in Figure 4.6, the three Matérn curves appear to collapse on each other. This supports the hypothesis that the N_p and R parameters, as with the underlying radial distribution function, are the driving factors impacting deviations from scattering theory for a homogeneous medium.

4.5.3 Variations in optical depth-dependent flux due to changes in Matérn clustering parameters

The optical depth-dependent irradiance results previously shown in Figure 4.6 demonstrate a lack of dependence on changes to the clustering parameters absent from the Matérn RDF (namely, particle radius and mean number of particles per cluster, λ_D). We next investigate the impact of the parameters that are present in the Matérn RDF, namely cluster radius (R) and number of clusters (N_p). To determine the sensitivity of depth-dependent irradiance to cluster radius, we held all other quantities constant; 500 cluster parents with an average of 64,000 daughter particles of radius 14μm were inserted using the Matérn process. Three cluster radii were explored (R = 0.03, 0.015 and 0.0075 meters) and compared to the homogeneous (spatially-uncorrelated) case; the results are shown in Figure 4.7. We see that as cluster radius decreases and the same number of particles are packed more densely, direct transmission is maximized and diffuse forward flux is minimized. Differentiation between the three Matérn curves is evident in both panel (a) and panel (b), illustrating the dependence on cluster radius R found in the RDF. We also note that there is a significant deviation of the backward diffuse flux for these Matérn cases as opposed to the homogeneous medium, as shown in panel (c); this ultimately results in a change in the total forward flux shown in panel (d).

Similarly, we explore the relationship between the number of cluster parents (N_p) and depth-dependent irradiance by constraining R and a, and allowing the average number of daughter particles per cluster, λ_D, to increase as N_p decreases to maintain constant expected optical thickness. The results of this investigation of constant cluster size R are shown in Figure 4.8. We see that decreasing N_p increased the deviation from the spatially-uncorrelated case, supporting the notion that the optical-depth-dependent irradiance is impacted by a changing RDF. As can be seen from the dependence of the RDF expression on number of parents N_p and illustrated in Figure 4.1, decreasing N_p with fixed R leads to an increase in the magnitude of the radial distribution function for all $r < 2R$. Once again, in Figure 4.8 there is an observed departure of the backward flux from the homogeneous expectation.

(a) Direct (Normalized) Forward Flux

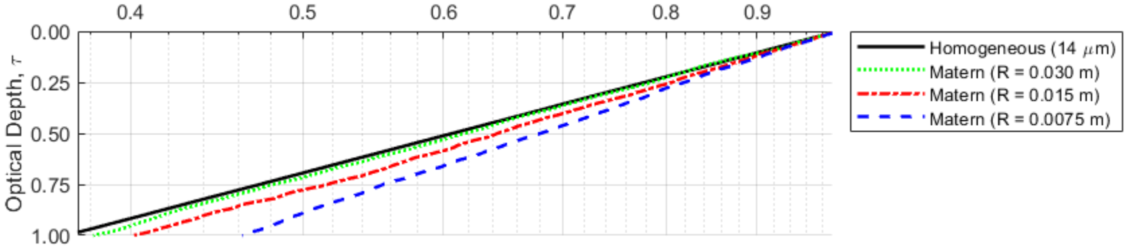

(b) Diffuse (Normalized) Forward Flux

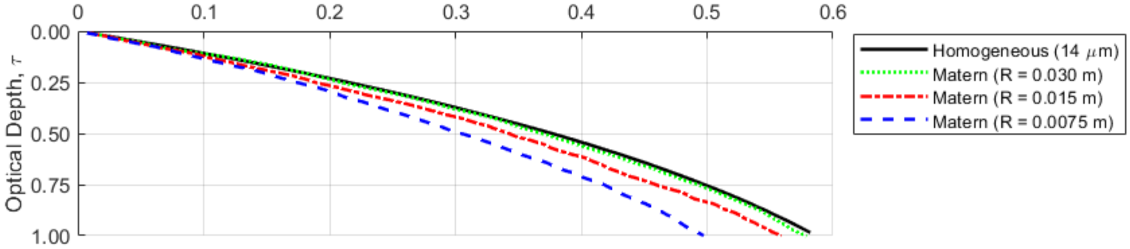

(c) Backward (Normalized) Flux

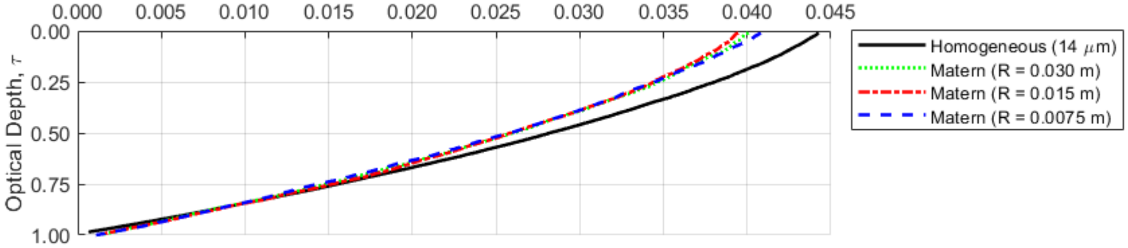

(d) Total (Normalized) Forward Flux

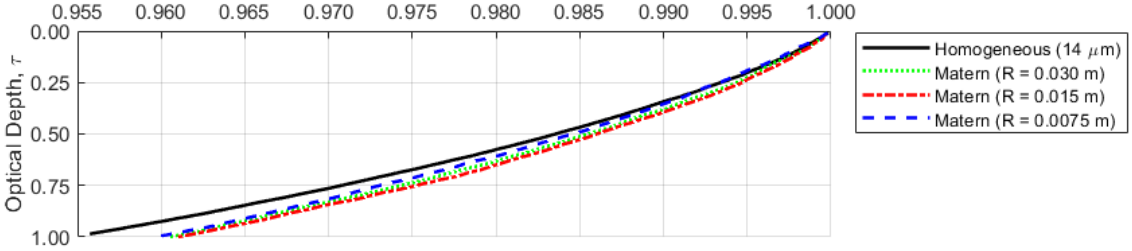

Figure 4.7. Optical depth-dependent flux curves for a variety of Matérn-generated cloud distributions, with homogeneous particle distribution results shown for comparison. All virtual cloud distributions are monodisperse with 14 μm particle radius. Note that in all three Matérn scenarios, the density of clusters and mean number of particles per cluster are constant (e.g., N_p = 500 and λ_D = 64000, respectively).

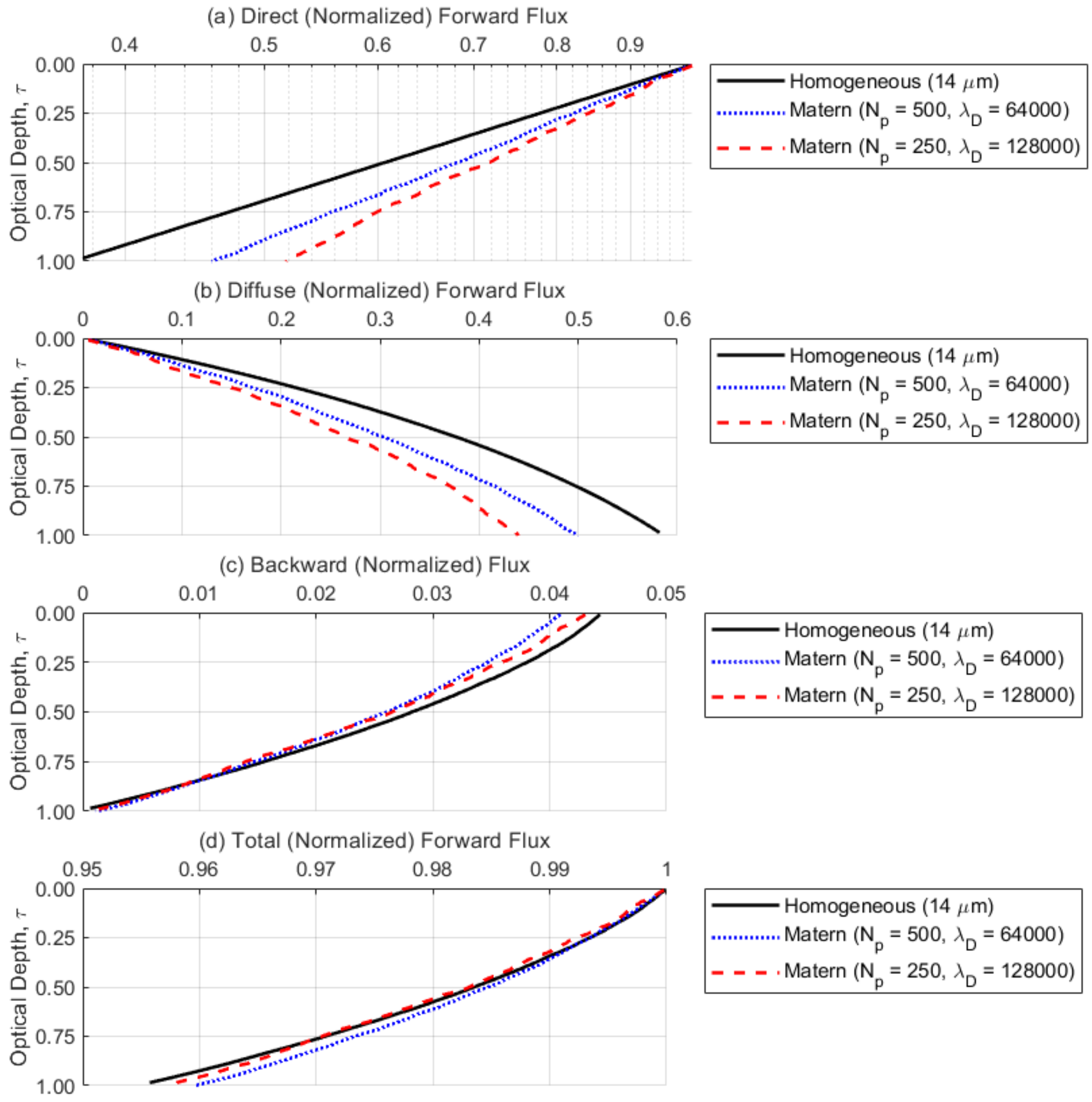

Figure 4.8. Optical depth-dependent flux curves for a variety of Matérn-generated cloud distributions, with homogeneous particle distribution results shown for comparison. All virtual cloud distributions are monodisperse with 14 μm particle radius. Note that for both Matérn scenarios, cluster radius is constant (e.g., R = 0.0075 m).

The family of RDF curves shown in Figure 4.1 were created by varying N_p and R, the two primary independent variables (beyond distance from cluster center, r); each of those nine RDF curves have a different $g(r = 0)$ peak correlation value. To explore the relevance of the shape of the Matérn RDF beyond just the peak correlation value, we study the impact of various RDF curves with equivalent $g(r = 0)$. Solving the Matérn RDF expression in Eq. (26) for the peak correlation value for $r = 0$ yields

$$g_{3D}(0) = \frac{3V}{4\pi R^3 N_p} + 1. \tag{30}$$

This means that for a given set of (R, N_p) input parameters, if R is doubled (or halved) and N_p is divided by (or multiplied by) eight, the peak correlation value $g(0)$ will be unchanged. We studied the impact of three Matérn RDFs with the same peak correlation value with this method, and the recorded depth-dependent flux curves are shown in Figure 4.9. These results indicate that the impact of RDF on the radiative transfer depends on more than simply the peak correlation value, but also on the shape of the RDF itself. This confirms that both correlation strength and correlation length are relevant parameters.

(a) Direct (Normalized) Forward Flux

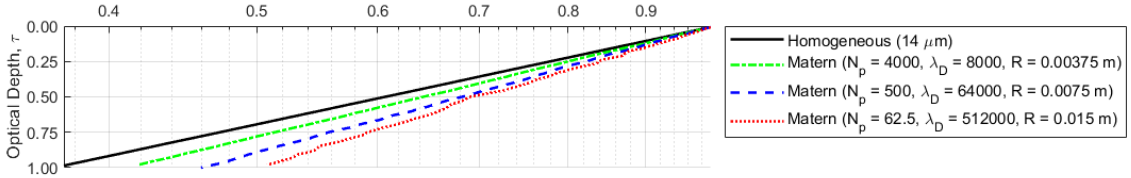

(b) Diffuse (Normalized) Forward Flux

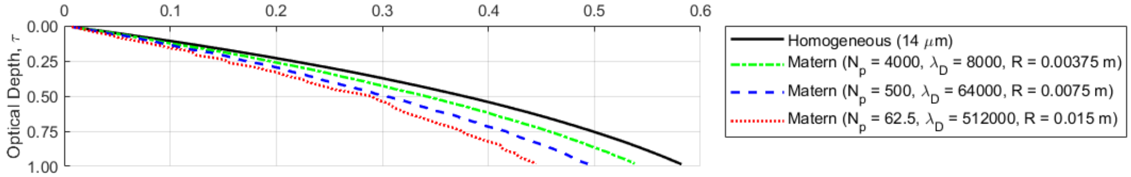

(c) Backward (Normalized) Flux

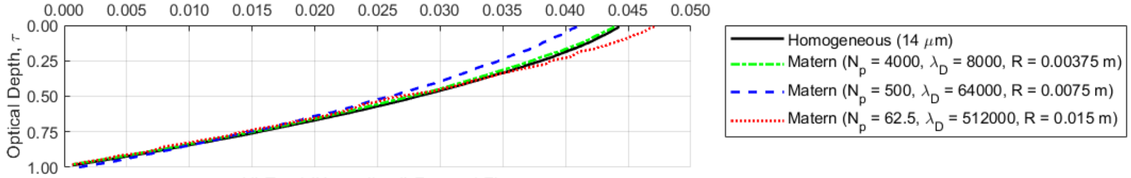

(d) Total (Normalized) Forward Flux

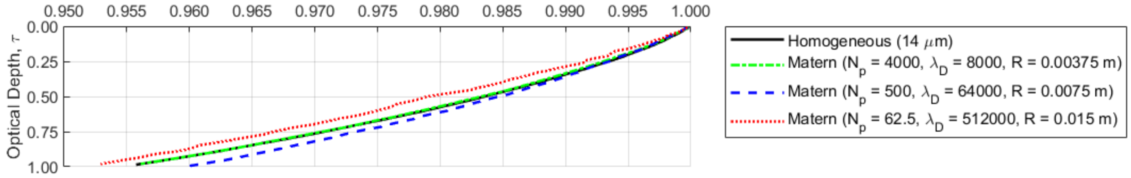

Figure 4.9. Matérn scattering results from three combinations of N_p and R, both present in the RDF and varied together to achieve a constant RDF at g($r = 0$), are compared. Note that λ_D was changed in correspondence with N_p to ensure a constant τ^* of 1.

4.6 Discussion and Conclusions

4.6.1 Summary and interpretation of results

The presence of absorbing particles in a medium influences the direct radiative transfer through the medium, and the resulting optical transmissivity is dependent on the size and number of particles. However, if spatial correlations exist in particle locations, the resulting nonuniformities can lead to both clusters and voids on scales of the same order as or smaller than the optical mean free path (as defined for a uniform medium). In a purely absorbing medium, the net effect of these voids and clusters is to increase the direct radiative transfer through such a spatially-correlated medium, leading to sub-exponential extinction that deviates from the prediction of Beer-Lambert-Bouguer attenuation theory (Kostinski, 2001). Conversely, negative spatial correlations (e.g., repelling particles) can lead to super-exponential extinction (Shaw et al., 2002a).

In the scattering-dominated limit, for which absorption is essentially non-existent, radiation is either transmitted directly (no interaction with particles in the medium) or diffusely (once a particle is encountered, the direction of propagation changes but the photon continues to traverse the medium). In this work, we have investigated direct and diffuse radiative transfer in a medium with spatially correlated scattering particles with a simplistic “ballistic photon” model. Our simulations explored the forward-dominant scattering regime that is typical of atmospheric clouds. The results are framed in the context of forward and backward fluxes, motivated by the commonly used two-stream flux equations.

Clustering was introduced using a Matérn clustering process with an analytical RDF to rigorously study the impact of four independent parameters, namely the number of clusters N_p, the cluster size R, the density of particles within a cluster λ_D, and the particle radius a. The parameter space was explored by constraining total optical depth τ^* to be 1 for all scattering simulations, and then considering various combinations of N_p, λ_D and a which together comprise the inputs to cloud optical thickness. Optical depth does not depend on cluster radius R, but the Matérn RDF depends on both R and N_p.

We found that particle clustering does indeed increase direct transmission, but we also found that diffuse forward irradiance is correspondingly reduced by a similar amount (Figure 4.5). Additionally, we found that varying only parameters absent from the Matérn RDF (e.g., a and λ_D) had no statistical impact on depth-dependent flux recordings (Figure 4.6). However, we determined that varying R and N_p (which are present in the RDF) did impact the irradiance results calculated by the scattering simulations (Figure 4.7 and Figure 4.8, respectively). Smaller clusters resulted in greater deviations from the direct and diffuse forward homogeneous baseline results, as did fewer but more densely packed parent clusters. Both of these conclusions are consistent with the hypothesis that these deviations are caused by voids in the scattering medium, and the heuristic prediction of the Beer-Lambert-Bouguer deviations developed by Kostinski (Kostinski, 2001, 2002).

For a constant total number of particles in a volume, both smaller clusters (all else equal) and fewer clusters result in larger voids and less (forward-dominant) scattering.

Lastly, we explored the relevance of the shape of the Matérn RDF beyond the peak correlation value (i.e., $r > 0$) by changing R and N_p in tandem to study the impact of various RDF curves with equivalent $g(r = 0)$ peak values. We found that in addition to peak correlation value, the shape of the Matérn RDF is also significant, as evidenced by the varying depth-dependent flux curves in all four panels of Figure 4.9. The Monte Carlo scattering simulations confirm that both correlation strength and correlation length are relevant parameters for predicting radiative transfer in a spatially correlated particle-laden medium.

Some insight can be gained from considering the relevant length scales in this radiative transfer problem. There are at least four scales: particle radius a, cluster size R that can be referred to as the correlation length scale, the photon mean free path defined for the volume-average properties $l \approx 1/(nQ_{sca}\pi a^2)$, and the box size L. In this work L has been fixed and constrained to be equal to l, such that $\tau^\star = 1$ for all cases. The clustering or correlation length R in all cases explored here is smaller than l. The results show that both the correlation length and the strength of correlation, expressed for example through $g(r = 0)$ (cf., Eq. 6 for the relationship with N_p), determine the extent to which optical propagation and scattering deviate from the theoretical prediction for domain-average properties.

4.6.2 Results in context with prior work

Previous work (Petty, 2002; Larsen and Clark, 2014) has gone into detail on trying to understand the inter-relationships between length scales in this problem. For purely absorptive media, Larsen and Clark (2014) used numerical simulations to reveal that at least three different length-scales will be relevant – particle size, correlation length-scale, and optical mean-free-path between particles. The work of Petty (2002) also has similarities to the approach presented here, with the “cloudlets” designed in that model similar in structure to the individual Matérn clusters in our simulation. Petty’s approach employs a non-dimensional parameter τ' (referred to as the effective mean optical thickness of a cloudlet) to attempt to capture all relevant information about small scale variability necessary to resolve the deviations from expected Beer-Lambert-Bouguer exponential transmission. For our Matérn-clustered clouds, this τ' parameter can be expressed as

$$\tau' = \frac{3Q_{sca}a^2\lambda_D}{2R^2}. \qquad (31)$$

In Petty’s notation the effective optical thickness, which accounts for enhancement in transmission due to non-uniform distribution of liquid water, is expressed as $\tau^*_{eff} = \varphi(\tau')\sigma\overline{W}$ where $\varphi(\tau')$ is the optical depth reduction factor and $\overline{W}$ is the average liquid water path. This can be written as $\tau_{eff}^{*} = \varphi(\tau')\bar{n}Q_{sca}\pi a^2 L$ where $\bar{n}$ is the domain-averaged number density. In terms of Matérn parameters, the mean volumetric number density is $\bar{n} = N_p\lambda_D V^{-1}$, allowing us to write the effective optical thickness as $\tau_{eff}^{*} = \varphi(\tau')N_p\lambda_D V^{-1}Q_{sca}\pi a^2 L$. Petty's cloudlet optical thickness can be expressed as $\tau' = 3Q_{sca}a^2\lambda_D(2R^2)^{-1}$, but since we constrained the global optical thickness through constant $\bar{n}$ we can re-write that as $\tau' = 3Q_{sca}a^2\bar{n}V\left(2R^2N_p\right)^{-1}$.

This is an intriguing result because we can now see that we have the same variable dependence, i.e. N_p and R, as seen in our Matérn RDF in Eq. (26). Given this encouraging similarity, we computed $\varphi(\tau')$ and τ_{eff}^{*} for the conditions in all of our simulations to compare predictions of direct, non-exponential transmission. The results of this comparison (see Figure 4.10) show reasonable agreement between our Monte Carlo results and the cloudlet model, suggesting that the Matérn RDF is consistent with the cloudlet approach.

Because of the connection between the RDF and traditional, continuous correlation functions (Shaw et al., 2002b), this RDF-based work can serve as a bridge between the two approaches: radiative transfer calculations based on continuous correlation functions (Borovoi, 1984; Frankel et al., 2017) and those based on the analytical results from the clearly-visualized cloudlet model. The RDF has the advantage that it has a direct link to discrete particle distributions, and it is general in the sense that it can describe more than Matérn or cloudlet models. For example, analytical expressions exist for less defined forms of clustering, beyond the Matérn notion of spherical particle clouds surrounded by voids (e.g., modified Thomas, Gibbs systems, excluded volume, etc.). The links identified here open the door for exploring to what extent other RDF expressions are able to facilitate comparison of Monte Carlo results, and furthermore suggest that it should be possible to find a quantitative link between $\varphi(\tau')$ and the RDF.

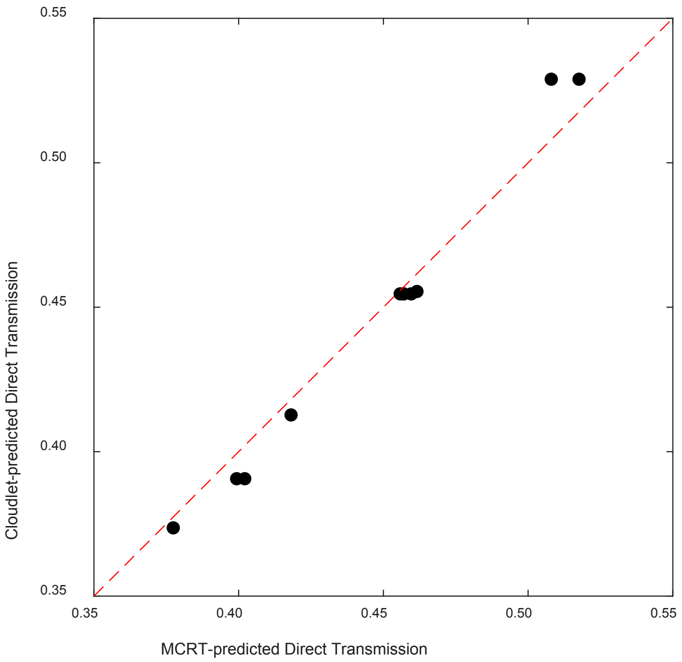

Figure 4.10. Comparison of direct, non-exponential transmission through spatially correlated particle distribution.

A renormalization technique for predicting radiative transfer for inhomogeneous clouds was proposed by Cairns et al. whereby single scattering parameters are modified based on spatial variances in scatterer concentration for use with plane-parallel calculations (Cairns et al., 2000). They propose that for random, purely scattering media where the correlation length is of the same order as the mean free path, an augmented extinction cross section and asymmetry parameter can be computed as

$$\begin{gathered} \sigma'_{ext} = \sigma_{ext}(1 + V_{rel})^{-1} \\ g' = g[1 + V_{rel}(1 - g)]^{-1} \end{gathered} \tag{32}$$

where V_{rel} is the relative variance of scatterer concentration. When spatially-varying scatterer concentration $N(r)$ is comprised of a mean concentration $\bar{N}$ and zero-mean fluctuating component $\eta(r)$, as in

$$N(r) = \bar{N} + \eta(r), \tag{33}$$

relative variance can be expressed as

$$V_{rel} = \langle \eta(r)^2 \rangle \, \bar{N}^{-2} \, . \tag{34}$$

For our analysis, the average scatterer concentration is simply the total number of scatterers divided by the simulation volume. The variance calculations will depend on how the simulation volume is subdivided, i.e., it will be scale dependent. The number of scatterers in each subvolume can be used to compute $\eta(r)$ and ultimately V_{rel}. For example, when 32x10^6 particles are grouped into 500 parent clusters with an average of 64,000 particles per cluster (of radius 7.5 mm), dividing the 0.08 m^3 volume into ten subvolumes along the path of the direct beam yields a small relative variance of 1x10^{-2}; division into 1000 cubic subvolumes (e.g., 10x10x10) results in a larger relative variance of 1.3. These values of V_{rel} lead to modified asymmetry parameter g' values of 0.849 and 0.711 (respectively) and modified scattering efficiency Q'_{sca} values of 1.98 and 0.87 (respectively). In the former case, where the scattering parameters are only slightly augmented, the MCRT results match those of the homogeneous case (where $g = 0.85$ and $Q_{sca} = 2.0$) and do not predict the direct and diffuse forward flux deviations seen in the Matérn clustering simulation. In the latter case, where the scattering parameters are heavily modified by the calculated relative variance, total optical thickness is greatly reduced (from 1.0 to 0.425, due to a reduced Q_{sca}) and none of the various flux components are predictive of the Matérn-based MCRT results. This serves to illustrate the dependence of averaging scale when considering a system of discrete particles. Here we have considered correlation lengths smaller than the mean free path, and it should be noted again that this is outside the range explored by Cairns et al. (2000).

4.6.3 Concluding remarks and implications

It is reasonable to consider the implications of this work for radiative transfer in the cloudy atmosphere, as a specific example of a particulate system that possesses spatial correlations over a large range of scales. The influence of spatial inhomogeneity on three-dimensional radiative transfer has been considered in depth, for the limit in which the scale of the inhomogeneity is larger than the mean free path defined for the medium. The pioneering work of Kostinski (2001) makes clear, however, that fundamental assumptions of the continuum approach to radiative transfer are called into question when correlations in a discrete-particulate medium are considered. Indeed, in atmospheric clouds typical mean free paths for regimes dominated by scattering (e.g., visible light) are of order 100 m, so essentially the entire turbulence inertial subrange lies at smaller scales. Therefore, entrainment and mixing processes generate strong spatial correlations in droplet positions from the ~100-m energy injection scale to the ~1-mm dissipation scale, and inertial clustering generates spatial correlations from the ~1-cm scale down to the ~10 µm scale of a single particle diameter (Wyngaard, 1992, 2010b). The question of how these sub-free-path-scale correlations might influence radiative transfer has been studied by several groups for the absorbing-particle limit (Kostinski, 2001; Shaw et al., 2002a; Larsen and Clark, 2014; Frankel et al., 2017). In this work we have explored the regime in which light scattering is dominant, and specifically for particles larger than the illuminating wavelength for which forward scattering is pronounced; this is the relevant regime for atmospheric clouds and visible/near-IR radiation. The results of the study suggest that the degree to which there is a deviation from standard radiative transfer using the medium-averaged optical properties (e.g., mean free path) can be quantified through the radial distribution function. This implies that knowledge of the RDF resulting from inertial clustering and turbulent mixing in atmospheric clouds would be valuable (Larsen et al., 2018). Treatment of the RDF is a first step, as a two-particle correlation function, and eventually it will be insightful to consider the possible relevance of multi-particle correlations on light propagation.

This work has focused on the influence of clustering at scales below the mean free path of the radiation, for optical depths up to order unity. Implications for larger scales such as would be relevant to cloud remote sensing or energy budgets will require consideration of cloud organization at the full range of scales: for example, it is already widely appreciated that clustering on spatial scales large compared to the photon mean free path is of significance in practical applications. It is known, however, that the turbulent energy cascade stretches down to the 1 mm scale in the atmosphere, so clouds can be assumed to be non-uniform far below the scale of a mean free path. The next stage of this work is validation of the MCRT results directly with measurements in the Pi cloud chamber. Characterization of actual clustering strength in natural clouds will be required to put the chamber measurements into atmospheric context. This kind of comparison will allow the overall approach of MCRT methods to be assessed; although they are widely used in applied radiative transfer, they are known to neglect the detailed electromagnetic treatment that is potentially necessary for full representation of propagation in a correlated medium (e.g., Mishchenko et al. 2016). Experimental results will be the ultimate arbiter.

In some cases presented here, the changes to direct and diffuse radiation are nearly compensating; do such results suggest that there is no significance to the clustering? That depends on the problem under consideration: for any problem depending on directional properties of the radiation field, the details of direct versus diffuse will be of significance. It is a subject that will be investigated in subsequent, combined computational and experimental work. Indeed, the geometry chosen in this study was originally motivated by the desire to explore the extent to which optical propagation through a turbulent cloud can be studied in the laboratory. That has the advantage of allowing well-characterized cloud and turbulence conditions, as well as statistically homogeneous and stationary conditions needed for spatial and temporal averaging. The sensitivity actually required in a study of this phenomenon, for realistic turbulence and clustering levels, will be the subject of future work, but the results presented here suggest that measurement of the cloud particle RDF will be a necessary step in possible experiments.

5 Light scattering in a turbulent cloud: Simulations to explore cloud-chamber experiments

This chapter details predictions of direct and diffuse transmission of visible light through spatially correlated particle fields generated by Large Eddy Simulations, focusing on measurements that could be observed in the Pi cloud chamber. This work is in preparation for publication.[5]

5.1 Abstract

Radiative transfer through clouds can be impacted by variations in particle spatial distributions, particularly in the visible spectrum when considering larger water droplets. Due to mixing and inertial effects, spatial correlation often exists, resulting in clusters and voids within the droplet field that can lead to deviations from exponential extinction. Prior work has numerically investigated these departures from exponential attenuation in absorptive and scattering media; this work focuses on investigating the feasibility of detecting spatial correlation in realistic atmospheric clouds generated in a laboratory setting. Large Eddy Simulations (LES) are used to create atmospheric mixing clouds realistic for a turbulent laboratory cloud chamber. The resulting polydisperse particle fields, with some level of inherent spatial correlation, are explored via MCRT scattering simulation. The key result of this study is that differences in both mean flux and standard deviation about the mean differ when correlation exists, suggesting that an experiment in a laboratory cloud chamber could be designed to detect (and potentially measure) the presence of spatial correlation. While total forward flux is largely unchanged (due to scattering being highly forward-dominant with our size parameters), direct and diffuse forward flux are appear to be modified to a measurable extent. This finding, a result of using scattering simulations to explore chamber-realistic polydisperse particle size distributions functions, upholds our previously-published predictions regarding monodisperse cluster-induced flux deviations.

5.2 Introduction

Radiation transfers differently through a spatially correlated medium than through a homogeneous medium due to void and clusters; photons propagate further in less thick regions and experience stronger extinction in more dense regions (Marshak and Davis, 2005). Properly predicting radiative transfer through inhomogeneous media has many applications, including the cloudy atmosphere (Davis and Marshak, 2004; Larsen and Vasques, 2011) where pockets of clear and cloudy air on many spatial scales can be formed by mixing and entrainment (Davis et al., 1999; Shaw, 2003). In recent published work (Packard et al., 2019), we examined various components of radiative transfer

---

[5] Packard, C.D., Larsen, M.L., Cantrell, W.H., Shaw, R.A. "5 Light scattering in a spatially-correlated polydisperse particle field: Predicting laboratory cloud-chamber observations." *To be submitted*.

through homogeneous and clustered monodisperse particle distributions of discrete particles. We found that while direct transmission is increased in the presence of spatial correlation, diffuse forward transmission is reduced by a similar amount (nearly offsetting the increase in direct transmission).

In this work, we consider polydisperse distributions of discrete particles within a realistic laboratory atmospheric cloud as our motivating problem. We address the problem of predicting radiative transfer through both homogeneous and inhomogeneous media using a Monte Carlo Ray Tracing (MCRT) methodology previously shown to be consonant with standard radiative transfer (e.g., Bohren and Clothiaux, 2011). To limit scope, we focus this work on the transfer of visible light (e.g., wavelength ~ 550 nm) through an atmospheric cloud generated under laboratory conditions. In the visible spectrum, with the size of droplets in our particle size distributions, the size parameter dictates that absorption is practically non-existent. Consequently, in this study we assume a single scatter albedo of unity. Additionally, the number densities we consider (e.g., optical thickness near 0.1) allow us to concentrate on a regime where multiple scattering is not dominant.

Our principal motivation is the use of simulation to explore experimental designs which could be conducted to measure the presence (and possibly the severity) of particle clustering in a laboratory cloud chamber such as the Pi Cloud Chamber (Chang et al., 2016) is appealing. In a previous publication (Packard et al., 2019), we focused on monodisperse distributions with somewhat extreme Matérn clustering; a single particle size and rather small, dense collections of droplets were used for much of our analysis as we evaluated the role of radial distribution functions. In this work, a primary interest is the extent of deviation from the spatially homogeneous case expected when less extreme spatial correlation and realistic polydisperse size distributions are present. To represent radiative transfer in a real system such as the Pi Cloud Chamber, which is able to produce optical thicknesses near unity during short-lived expansion clouds and an order of magnitude smaller during long-lasting mixing clouds, we consider an atmospheric medium within a confined geometry. Computer simulation, acting as a surrogate laboratory, allows for the prediction of experimental results and development of an effective methodology for measuring relevant parameters absent physical limitations.

In this work, a Large Eddy Simulation (LES) code is used to generate particle clouds with properties (such as optical thickness, particle size distribution function and spatial correlation) realistic for a laboratory-generated mixing cloud. A MCRT code, capable of simulating scattering events with appropriate phase functions, propagates individual photons from a normally incident collimated beam through the LES-based particle distribution while tracking direct, diffuse forward and backward radiative fluxes. Two types of spatial particle distributions were employed, the first using the droplet locations exported from the LES, and the second replacing these particle locations with uniformly random positions to remove any spatial correlation. Hereafter, the product from the former method will be referred to as “LES-positioned” since the particle locations come directly from LES exports; the latter method will be referenced as “random” or "homogeneous" due to the lack of spatial correlation. Directional radiative transfer components (e.g., direct, diffuse forward, backward and total forward flux) are compared to determine the impact of realistic spatial correlation in a laboratory setting.

The paper proceeds as follows: First, we describe the MCRT scattering code and its ability to employ particle distributions imported from LES cloud realizations. Next we describe our LES methodology and summarize some of the most relevant statistics of the numerous cloud regions extracted for our scattering simulations. Then, we presents results of the simulations, showing the impact of spatial correlation on radiative flux components. Of primary interest is the effect of particle number density and optical thickness variations on both the mean direct and diffuse flux (average impact of spatial correlation) and the standard deviation that might be measured through a fluctuating mixing cloud. In the concluding section we discuss the results and their implications for atmospheric radiative transfer measurements in a laboratory setting.

5.3 Summary of the Monte Carlo Ray Tracing (MCRT) Methodology

5.3.1 Overview of the MCRT code ('mcScatter')

The Monte Carlo scattering software used for our analysis, referred to as 'mcScatter', is a ballistic photon simulation code (Shaw et al., 2002a; Larsen and Clark, 2014) created to explore radiative transfer through scattering media, such as light transport through an atmospheric cloud (Packard et al., 2019). The construction of this Monte Carlo Ray Tracing (MCRT) code was motivated, in part, by a desire to eventually compare numerical results with experiments performed in a cloud chamber facility (Chang et al., 2016). The *mcScatter* software is summarized here for convenience; a more detailed description can be found in Packard et al. (2019) and its supplemental material (see chapter 3).

Our MCRT code allows users to specify particle size, optical wavelength, complex index of refraction (to model various types of droplets) and many other boundary conditions. Here we focus our analysis on visible wavelengths (e.g., 550 nm) and examine chamber-realistic cloud droplet sizes based on previous laboratory measurements (Chang et al., 2016; Packard et al., 2018). The resulting size parameters concentrate our analysis on the single-scattering, forward-scattering dominant regime with a single scatter albedo of unity and a scattering efficiency of $Q_{sca} \approx 2$. Inspired by a realistic optical path through the chamber, the virtual spatial domain is limited to 2 m x 0.2 m x 0.2 m.

Monte Carlo numerical methods (Danielson et al., 1969; Plass and Kattawar, 1968; Collins et al., 1972; Sobol' et al., 1974) employ large numbers of random draws to explore challenging problems for which closed-form solutions may not exist, such as heterogeneous media (Marchuk et al., 1980; Marshak and Davis, 2005; Cole, 2005). Photons are virtually cast into a medium, scattering events are detected and new scattering angles are chosen using a Mie or HG (Henyey and Greenstein, 1941; Thomas and Stamnes, 1996; Ishimaru, 1997) scattering phase function. This process is repeated until all rays exit the medium. Many Monte Carlo numerical methods avoid assigning physical locations to particles; instead, the distribution of free paths between consecutive scattering interactions is modeled stochastically via random draws from an analytic cumulative density function (CDF) based on the concentration of particles in the medium (Bohren and Clothiaux, 2011).

Conversely, in a ballistic 'photon' simulation (Shaw et al., 2002a; Larsen and Clark, 2014), particles in a volume are placed at specific locations (Frankel et al., 2016; Banko et al., 2019). By employing an explicit location for each particle in the medium, geometric ray-tracing can be used to explore any inter-scatterer distribution since scattering events are determined by the intersection between a photon ray's path and a particle (i.e., a geometric "collision"). Since ballistic photon simulation allows for particle spatial distributions of any kind, there is no need for stochastic free-path distribution models to exist.

Other methods, such as approaches derived directly from Maxwell's equations (Mishchenko, 2008; Mishchenko et al., 2016), incorporate a detailed electromagnetic treatment of the problem and are especially well-suited for continuous media. However, even for a small atmospheric cloud (e.g., many millions of particles), methods like the superposition *T* matrix remain largely impractical. Ballistic photon simulations, in contrast, are well-matched for resolving generalized spatially-correlated media (Shaw et al., 2002a). Our ray tracing Monte Carlo radiative transfer approach is consistent with standard radiative transfer theory (Bohren and Clothiaux, 2011) and should be consistent with Mishchenko's findings (Mishchenko, 2006, 2008) that even in a correlated medium, classical radiative transfer equations hold as long as high-order scattering is negligible and assumptions of ergodicity and spatial uniformity are valid.

During a *mcScatter* simulation, ray segments are recorded as rays are traced through particle fields before and after the occurrence of scattering events. Direct and diffuse flux components, both backward and forward, are recorded at numerous physical depths in the virtual cloud. This allows for the calculation of direct, diffuse forward, backward and total forward irradiance components as a function of physical depth in the cloud. Further details regarding the implementation of our scattering code and comparisons with theoretical and other published numerical works can be found in Packard et al. (Packard et al., 2019).

5.3.2 Use of the 'mcScatter' MCRT software with chamber-realistic particle distributions

The MCRT software *mcScatter* can perform ballistic photon scattering simulations using a variety of atmospheric media including both monodisperse and polydisperse particle size distributions with either homogeneous or spatially correlated spatial distributions. In our most recent publication (Packard et al., 2019) we focused on the impact of spatial correlation on depth-dependent direct and diffuse radiative transfer for monodisperse particle distributions. That study was enabled by a Matérn Point Process particle clustering algorithm which generates spatially correlated droplet distributions with user-specified parameters (Larsen et al., 2014).

For the current study we incorporate the additional but realistic and unavoidable complexity of polydisperse particle size distributions found in actual atmospheric conditions, and we explore the impact of spatial correlation on the order of that expected in our laboratory cloud chamber facility (Chang et al., 2016). Computer simulations, referred to as Large Eddy Simulations (LES) and described in Section 5.4, were used to generate realistic particle distributions; the output from these simulations was used as an input to the mcScatter photon simulation (rather than employing either homogeneous or Matérn-clustered clouds). Data files generated by the cloud chamber simulations include both the radius of each droplet (quantized to a finite number of size bins) and three-dimensional position of that droplet.

These data files were read by the *mcScatter* software for analysis, which has the ability to use or ignore the somewhat correlated particle locations from the LES-exported records. When the LES-positioned droplet locations are ignored, uniformly random (*x, y, z*) values are generated for ballistic photon simulation. This allows us the capability to compare realistic polydisperse particle clouds with either homogeneous or correlated spatial properties.

5.4 Large Eddy Simulation

5.4.1 Large Eddy Simulation Methodology

The System for Atmospheric Modeling, referred to as SAM (Khairoutdinov and Randall, 2003), is a Large Eddy Simulation (LES) code modified to simulate the Pi chamber at Michigan Tech (Chang et al., 2016). For simulating the aerosol - cloud interactions, the code has been coupled with HUJISBM, a spectral bin microphysics code (Khain et al., 2004). To simulate the cloudy Rayleigh-Bénard convection, SAM has been scaled down and the top and lateral boundary conditions have been modified and quantitatively verified against experiments (Thomas et al., 2019). For completeness, a brief description of the SAM model is provided below.

The dimensions of the simulated cloud chamber are 2 m x 2 m x 1 m, with the shortest dimension being the height of the volume. We discretized this volume into small cubic boxes of side length 3.125 cm yielding 64 x 64 x 32 grid boxes. The time step was chosen to be 0.02 seconds, and the system was initialized with an unstable temperature and water vapor gradient along the direction of gravity. For the current study, we allowed the system to evolve and reach a steady supersaturation of 2.5%, measured as a planar average at the mean height in the chamber (being careful to avoid wall effects). Once this supersaturation point was reached (Thomas et al., 2019), we injected a single bin of cloud condensation nuclei (CCN) at the center of the chamber at a rate of ~92400 particles per cm^3 per second; all introduced CCN had a radius of 62.5 nm, representing a unimodal CCN distribution bin ranging from 56 nm to 71 nm. The cloud reaches a steady state by striking a balance between activation and removal due to sedimentation. On reaching steady state after 1 hour, the system is allowed to persist for another 45 simulated minutes.

Turbulence in the chamber involves multiple timescales, ranging from very fast processes (e.g., dissipation on the order of 0.1 seconds) to slow processes like large scale oscillations estimated at 90-135 seconds (Niedermeier et al., 2018). The 3D data are output at every five minutes (at least two times longer than the largest time scale in the system) during this final 45 minute evolution to get statistically independent droplet distributions within the simulated cloud chamber. Each of the 131,072 grid boxes (3.125 cm on each side) contains a number of droplets which are sorted into 33 different size bins according to their radii. Since the spatial distribution of droplets within each grid box is not resolved, the current study assumes non-intersecting droplets which are randomly distributed within the corresponding grid box volume. To achieve this, the droplets in each of the 3.125 cm cubic grid boxes are redistributed randomly inside its volume; care is taken to avoid droplet intersection while retaining a lack of correlation on sub-3.125 cm scales.

For analysis purposes, and to better compare with previous MCRT studies, we desired to extract many subvolumes from the overall chamber volume, each with dimensions of 0.2 m x 0.2 m x 2.0 m. These rectangular prisms serve as virtual cloud “subsamples” through which we can trace many optical paths. To this end we define a number of rectangular prisms, each of which comprise 3,136 adjacent 3.125 cm grid boxes – 7 wide, 7 tall and 64 in the direction of intended photon propagation. Each of these cloud subsamples has dimensions of 21.875 cm x 21.875 cm x 200 cm, which is trimmed slightly to the desired 0.08 m^3 volume. To improve our statistics, we chose 24 such subvolumes along each of the two perpendicular lateral walls, resulting in a total of 48 cloud subsamples per cloud realization (see Figure 5.1). Thus the output from the LES code is a file with a record entry containing an (x, y, z) position and binned radius for each droplet, which serves as the input for our ray tracing Monte-Carlo simulation code. Note that, as shown in Figure 5.1, no cloud subsamples are extracted from directly adjacent to a bounding surface of the LES volume.

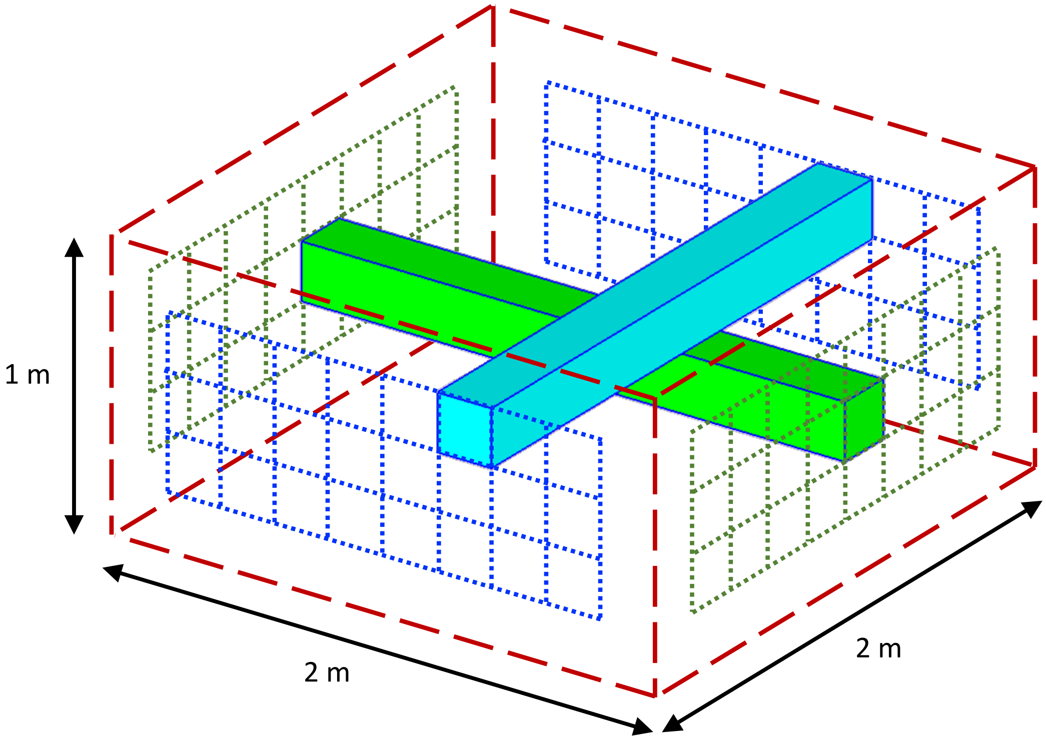

Figure 5.1. The entire volume of the simulated cloud chamber (2 m x 2 m x 1 m) is depicted with a dashed rectangular prism outline. Inside this volume, 48 high aspect ratio cuboids are extracted for optical analysis. Each cuboid, or cloud subsample, has dimensions of 0.2 x 0.2 x 2.0 m; 24 subsamples are taken from each horizontal direction in the chamber. Here the dotted grids show the ends of the 48 cloud subsamples, with only a single 3D subsample (rectilinear parallelpiped) portrayed in each direction; the other 46 are hidden for the sake of clarity.

5.4.2 Statistics of the LES Output

As previously described, after the LES simulation reaches steady state, the system is allowed to evolve for another 45 minutes and droplet sizes and 3D spatial positions are output from the cloud realization every five minutes for a total of nine statistically independent droplet distributions (Chandrakar et al., 2016, 2017). As shown in Figure 5.1, 48 cloud subsamples are extracted from each of the 9 cloud realizations for a total of 432 cloud sections. Before analyzing these cloud subsamples to determine the impact of spatial correlation between droplet positions, we first describe the statistics of their atmospheric properties including mean number density, mean geometric cross section and total optical thickness. The variation of values for the relevant atmospheric properties are shown in Figure 5.2, with total optical thickness, mean number density and mean geometric cross section shown in the top (a), center (b) and bottom (c) panels respectively.

Here it is useful to explain that in this work, total optical thickness refers to the total *expected* optical thickness. This is computed by summing the scattering cross sections of all particles in the distribution, scaled by the number density for each particle size, as shown in the expression

$$\tau_{exp} = \sum_{r} \frac{N(r)}{V} Q_{sca} \pi r^2 z \, . \tag{35}$$

In this estimate of total optical thickness, the scattering efficiency used in the summation is not computed using Mie theory but instead employs a geometric approximation (e.g., $Q_{sca} = 2$). All references to optical thickness in this work refer to expected optical thickness, calculated from particle size distribution functions only without the use of a scattering simulation to determine *actual* optical thickness.

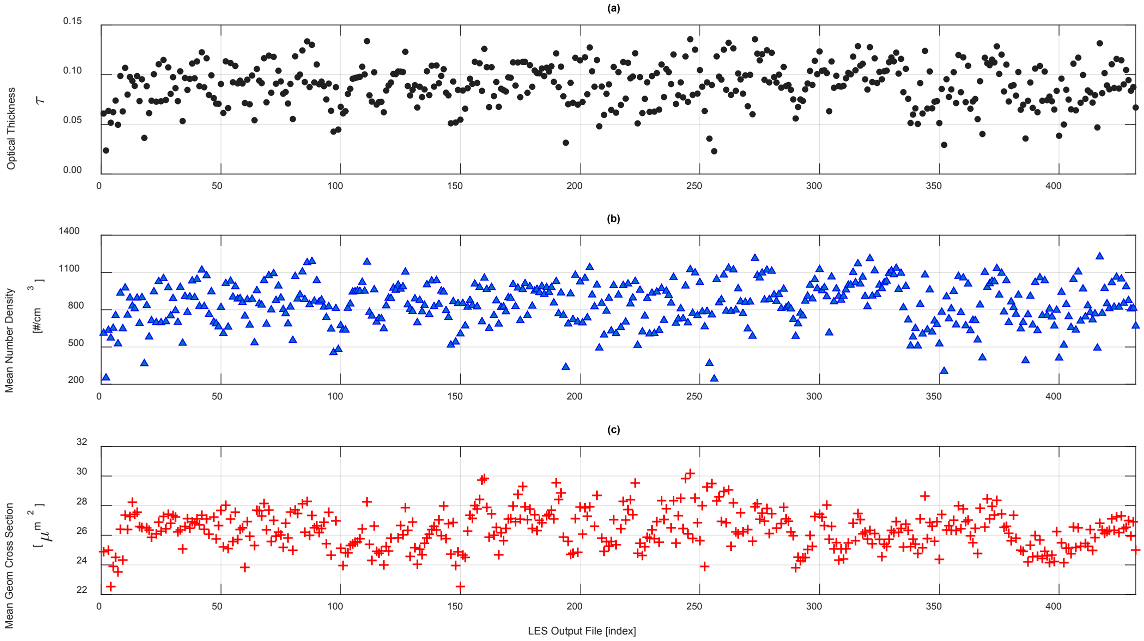

Figure 5.2. Mean number density (top), mean droplet radius (center) and total optical thickness (bottom) calculated from all 432 LES output files. It should be noted that these scatter plots are not time series; the index values used for the horizontal axis come from having 48 subsamples extracted from each of the nine time-steps.

Histograms of these statistics, depicted in panels (a), (b) and (c) of Figure 5.3, show total optical thickness, mean number density values and mean geometric cross section (respectively). Mean number density and total optical thickness were highly correlated ($R^2 = 0.97$), as shown in panel (a) of Figure 5.4, while mean geometric cross section and total optical thickness were related but not as correlated ($R^2 = 0.49$) as can be seen in the wider spread of points in panel (b) of Figure 5.4.

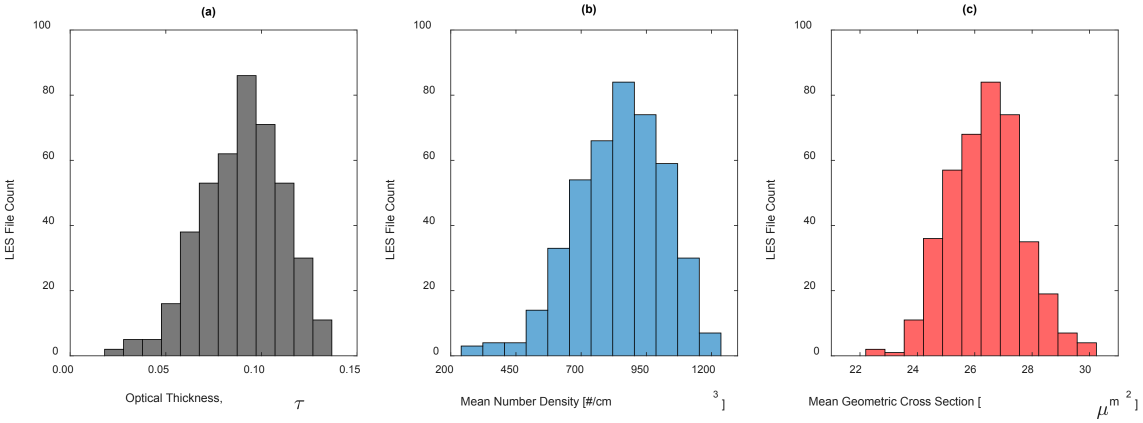

Figure 5.3. (a) Histogram of optical thickness from 432 LES output files. Values in the distribution range from 0.02 to 0.14 with an average optical thickness of 0.09, a standard deviation of 0.02 and a relative dispersion of 0.222. (b) Histogram of mean number density from 432 LES output files. Values in the distribution range from 243 to 1227 droplets per cubic centimeter with an average of 846 #/cm3, a standard deviation of 174 #/cm3 and a relative dispersion of 0.206. (c) Histogram of mean geometric cross section from 432 LES output files. Values range from 22 to 30 µm2 with a mean of 26.4 µm2, a standard deviation of 1.27 µm2 and a relative dispersion of 0.048.

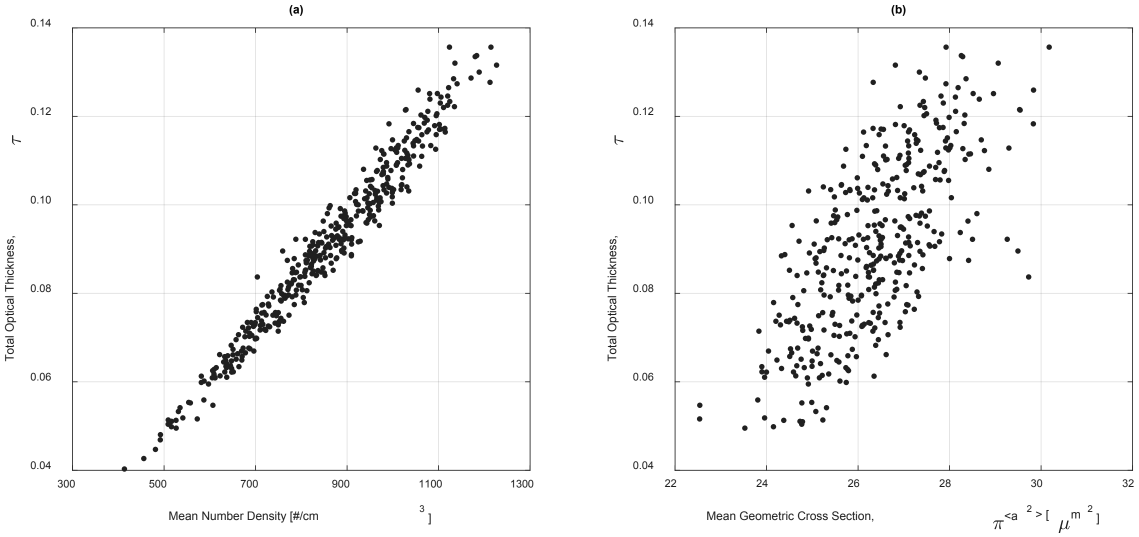

Figure 5.4. (a) Scatter plot showing high correlation ($R^2 = 0.97$) between mean volumetric number density and total optical thickness. This suggests that LES output files chosen based on similar number densities are highly likely to have very similar total optical thicknesses. (b) Scatter plot showing correlation ($R^2 = 0.49$) between mean geometric cross section and total optical thickness. This suggests that LES output files chosen based on similar mean geometric cross section are likely to have similar but not exactly the same total optical thickness.

The horizontal axes of panels (a) and (b) in Figure 5.4 indicate that the range of number density values is not only larger than the range of geometric cross sections but also more similar to the span of expected optical thickness values (vertical axes in both panels). Also of interest is the similarity and dissimilarities in the nine statistically independent cloud realizations from which the 432 LES subsamples were extracted. To this end, a box-and-whisker plot is shown in Figure 5.5 to depict some relevant statistics. The median value of optical thickness for each cloud realization is shown with a circular bullseye, the solid edges of the boxes represent the 25th and 75th percentiles, and the dashed "whiskers" extend to the most extreme values of τ. A solid red vertical line was added to represent the mean optical thickness of all 432 LES cloud subsamples (e.g., global average value of τ).

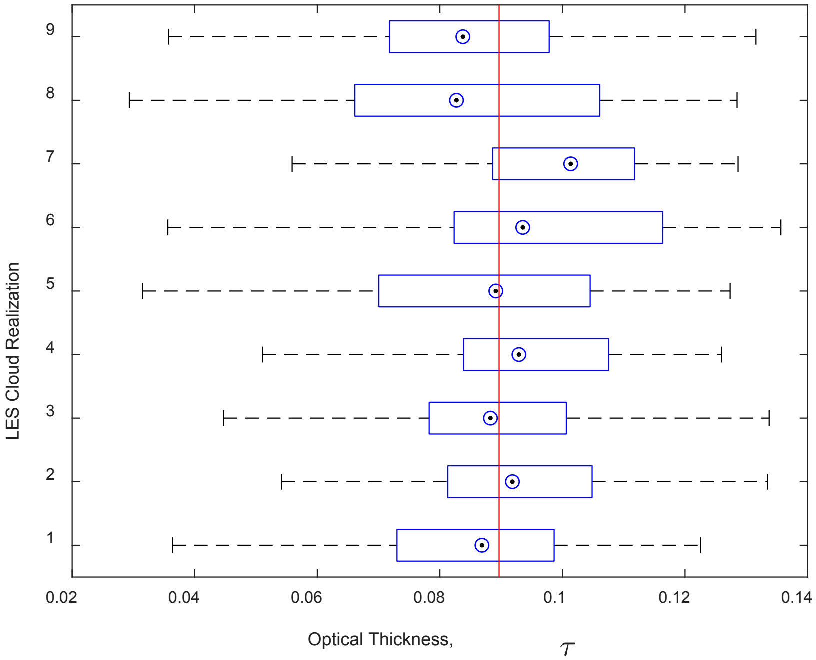

Figure 5.5. Expected optical thickness statistics shown for the nine LES cloud realizations (with 48 subsamples per realization). Circular bullseyes indicate median values, solid box edges show 25th and 75th percentiles, and dashed "whiskers" extend to the most extreme values. A solid vertical line was added to indicate the global mean optical thickness across all 432 cloud subsamples.

5.5 Results

5.5.1 Scattering MCRT results for LES particle clouds conditioned on estimated optical thickness

As shown in the expected optical thickness histogram depicted in panel (a) of Figure 5.3, the mean for all 432 cloud subsamples is close to a value of $\tau = 0.1$. With numerous cloud subvolumes near this average (expected) optical thickness value, a very tight window ($0.099 < \tau < 0.101$) can be used to select ten LES output files from all timesteps which are very similar from the perspective of total optical thickness. These ten LES polydisperse droplet distributions were used to run two sets of MCRT scattering simulations. In the first set, the spatial locations and droplet radii were used directly from the LES export process. Consequently, spatial correlation (on scales greater than the 3.125 cm grid resolution) may exist due to any voids and clusters formed during the turbulent LES process.

The results of this first LES set, conditioned on $\tau = 0.1$, are shown in Figure 5.6. Each of the four panels show a family of curves for different flux components including total forward flux, backward flux, diffuse forward and direct forward flux (clockwise from upper left, respectively). The deviations from curve to curve indicate the effects of spatial variations in the polydisperse droplet distributions.

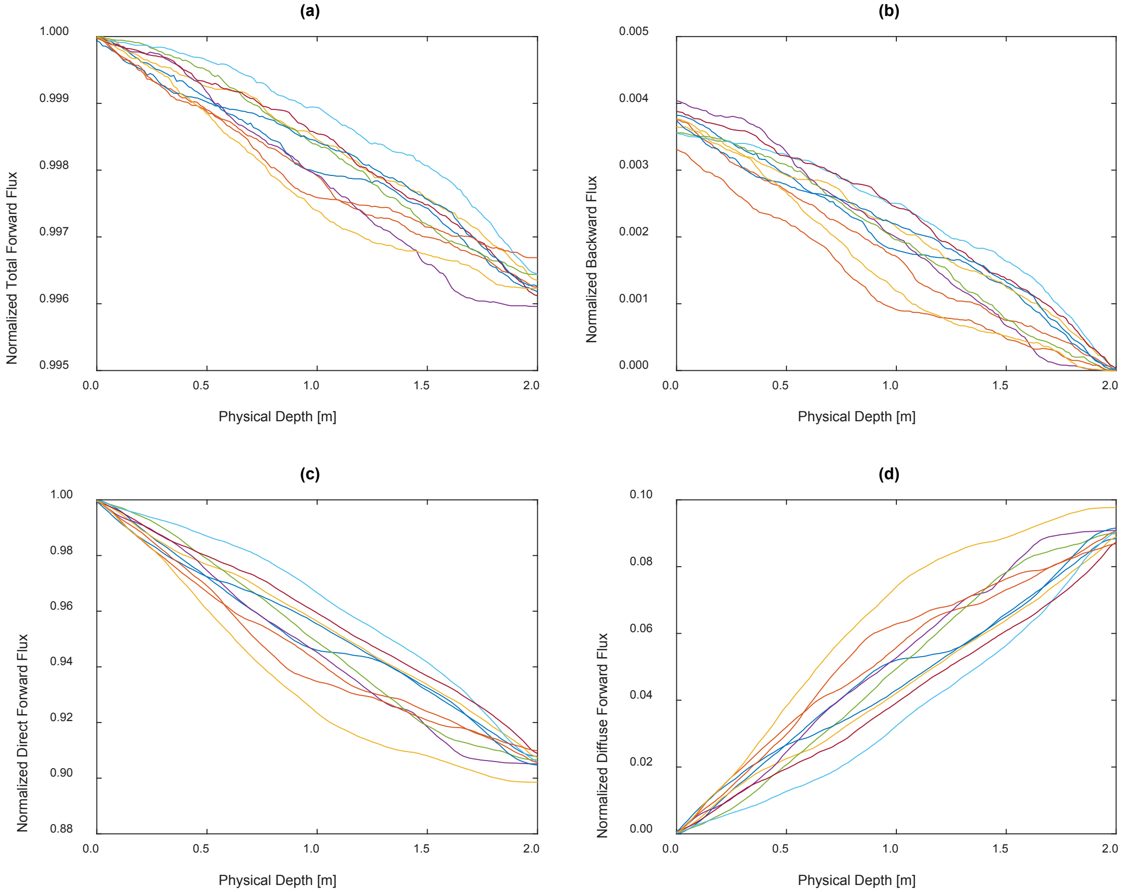

Figure 5.6. Depth-dependent flux curves for ten LES polydisperse spatial distributions, chosen to be very near an (expected) total optical thickness of 0.1. Spatial positions come directly from LES output records.

In contrast, the second set of scattering simulations employed the same LES-exported files but utilized only the radii values recorded for each droplet; the spatial locations determined by the LES process were discarded and replaced by uniformly random positions to create corresponding polydisperse distributions without spatial correlation. The results of this second set of simulations, also conditioned on $\tau = 0.1$, are shown in Figure 5.7. A much tighter grouping in the family of curves is evident and is due to the lack of clusters and voids in the spatial distributions. As this set of ten scattering simulations used the same (ten) polydisperse particle size distribution functions as the first set, with only droplet spatial locations being different from the LES-positioned results of Figure 5.6, only spatial correlation can explain these flux differences.

These flux component results show stronger deviations within a set (i.e., from the ensemble average) when LES spatial positions are used compared to uniformly random droplet locations.

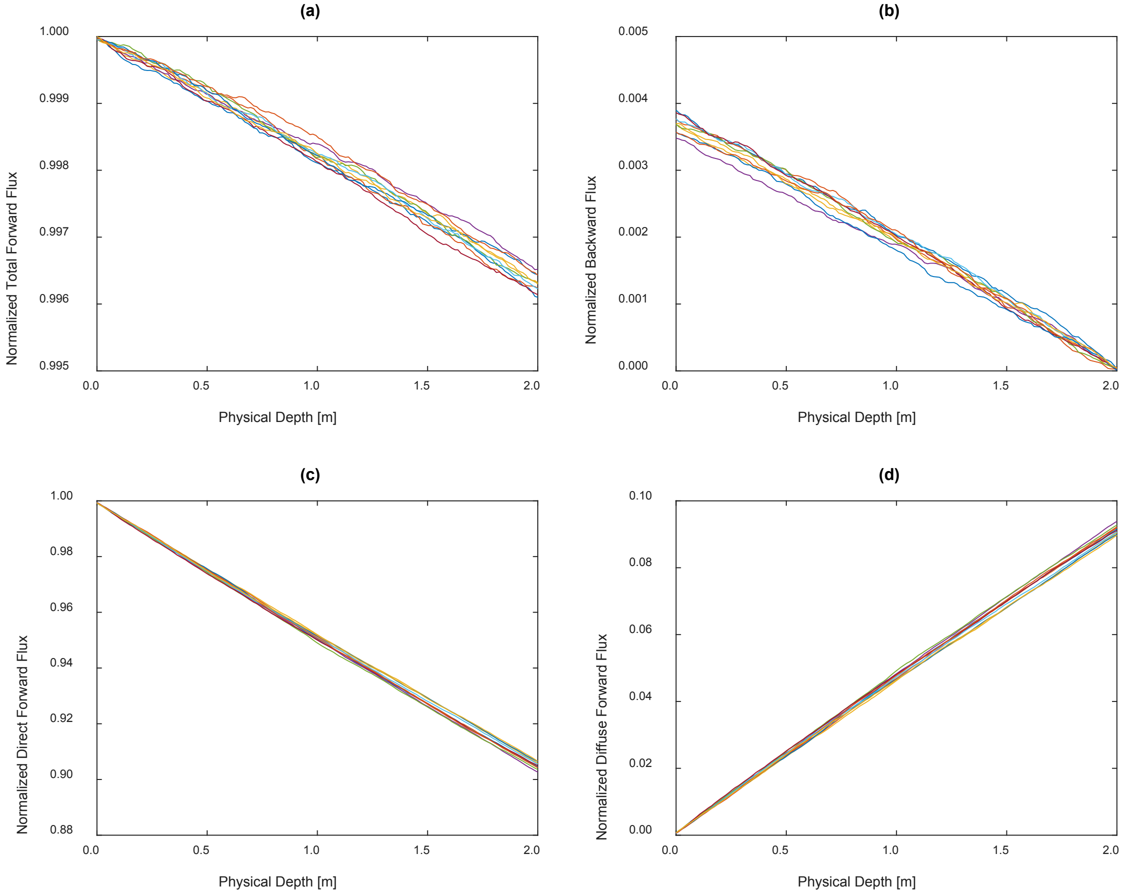

Figure 5.7. Depth-dependent flux curves for ten LES polydisperse spatial distributions, chosen to be very near a total optical thickness of 0.1. Spatial positions are uniformly random.

For reference, it may be instructive to better understand the variation in number density and optical thickness inside a representative LES cloud subvolume compared to its corresponding random counterpart (illustrated in the top and bottom panels of Figure

5.8). To this end, the two meter propagation path through the cloud subvolume was divided into four 0.5 meter slabs, and the number density and optical thickness of each slab were computed for both the LES-positioned and uniformly random spatial distributions. Panel (a) in Figure 5.9 shows the spatial correlation-created difference in number density for each 0.5 meter slab, while panel (b) shows the discrepancies in optical thickness.

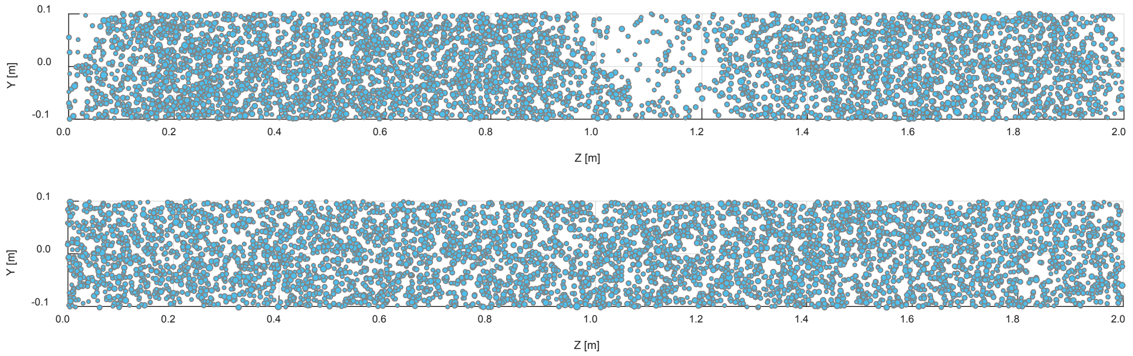

Figure 5.8. A random selection of 10,000 particles from each of the spatial distributions whose flux results are shown in Figure 5.10. The representative illustration in the top panel shows LES-positioned droplet locations, with high number density in the first meter and a large void between 1.0 and 1.2 meters. The bottom panel shows the same number of particles which have been placed in a uniformly random fashion.

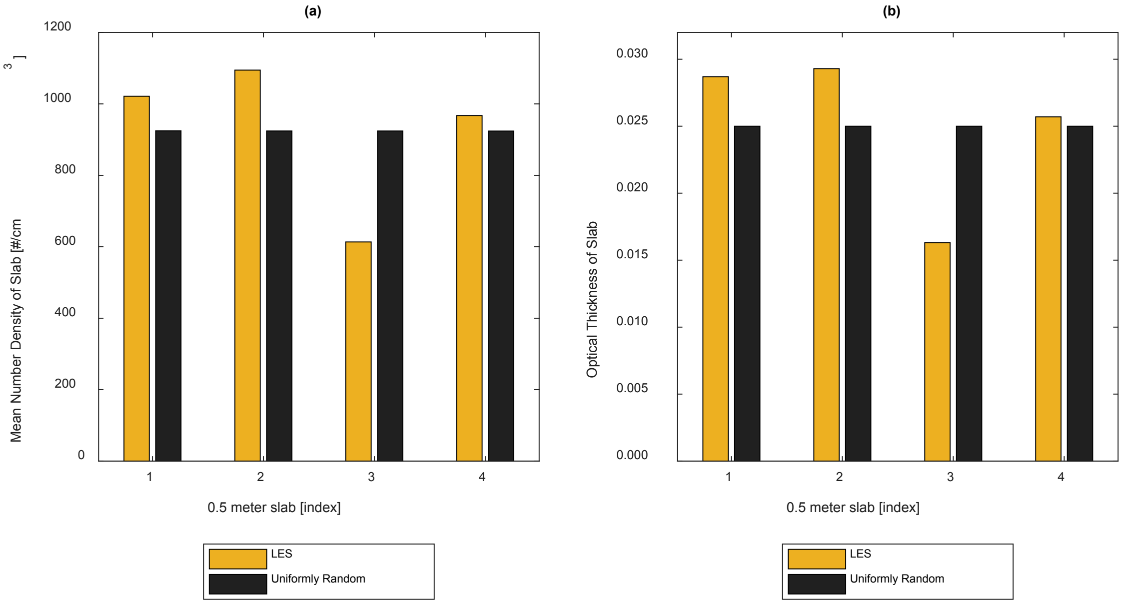

Figure 5.9. Comparison of LES-positioned and uniformly random polydisperse particle distributions for the four 0.5 meter slabs that comprise the two meter propagation path.

The local variations in number density and optical thickness lead to deviations in various flux components. While Figure 5.6 and Figure 5.7 each portrayed a set of ten depth-dependent flux curves, Figure 5.10 shows a flux comparison between a single LES subvolume (including its polydisperse particle size distribution function and spatial correlation) and its uniformly random counterpart.

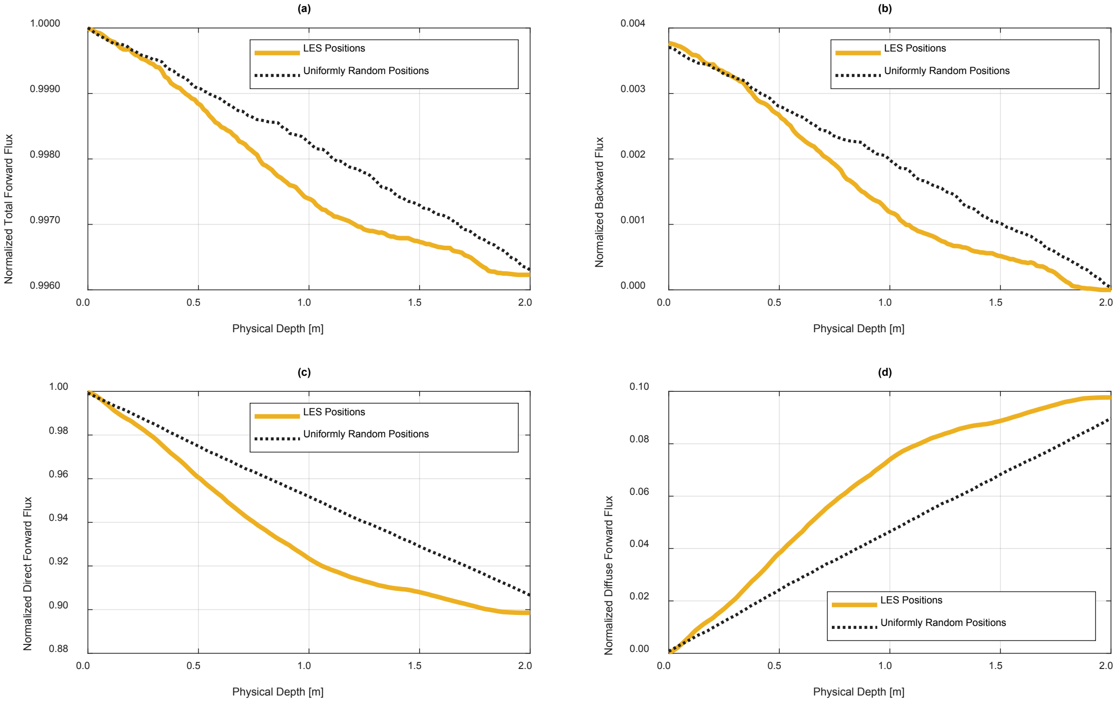

Figure 5.10. Normalized flux components from two scattering simulations which both employ the same particle size distribution function. The thick yellow line results from the use of LES-positioned droplet locations, while the dotted black line results from the use of uniformly random particle positions.

5.5.2 Impact of spatial correlation on depth-dependent flux results

As predicted in previous works (Petty, 2002; Packard et al., 2019), spatial correlation typically leads to an increase in direct flux but a largely compensating decrease in diffuse forward flux. When backward flux is relatively unchanged, the total forward flux is also largely unchanged due to the offsetting nature of direct and diffuse forward flux. This is evident in Figure 5.11, where the dashed vertical lines show the mean flux values for each component. The yellow dashed lines display the means of the simulations which employed LES-positioned spatial records, while the black dotted lines indicate the means of those with uniformly random droplet locations. As can be seen in panels (a) and (b) in Figure 5.11, the total forward and backward flux means are nearly identical; easier to differentiate are the direct and diffuse forward flux means shown in panel (c) and (d), respectively.

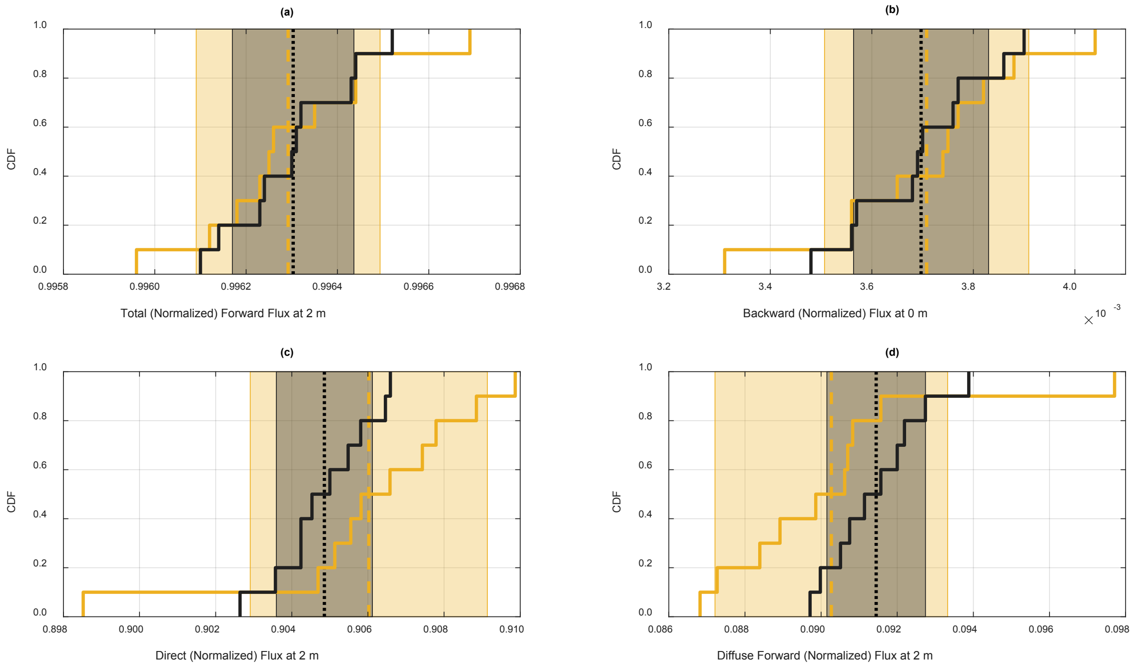

Figure 5.11. CDF calculated from the flux results of two sets of scattering simulations, one with LES-positioned particles with some level of spatial correlation and the other with uniformly random droplet locations. Both sets of results employed the same LES-exported particle size distribution functions (chosen for total optical thickness near 0.1), meaning the only difference between the two sets is the use of LES spatial positions vs. uniformly random positions (same droplet size distribution). Each horizontal axis is a different flux component, normalized by incident illumination. Mean flux values are shown with dashed and dotted vertical lines, and filled rectangles are created by adding and subtracting a standard deviation to show the variation in flux values. These filled rectangular regions are shown at 2 m for all flux components except backward flux, which is shown at 0 m (incoming face).

Also of interest is the standard deviation of each set, which is significantly larger for the spatially correlated simulations. This is depicted in Figure 5.11 with filled rectangular regions (yellow rectangular fill for the LES-positioned set vs. grey fill for the randomly positioned set) created with horizontal limits one standard deviation from the mean (e.g., $\mu_{set} \pm \sigma_{set}$). For both total forward flux and backward flux, shown in panels (a) and (b) respectively, the LES-positioned results have a standard deviation of 0.0002 while the uniformly random set has a standard deviation of 0.0001. Of more interest are differences in standard deviation for the direct and diffuse forward flux components, shown respectively in panels (c) and (d) of Figure 5.11. The standard deviation in direct flux for the uniformly-random set is 0.0013, while the corresponding LES-positioned set has a standard deviation of 0.0031 - almost 2.4 times larger. The statistics for the diffuse forward flux are the same, with the LES set having a standard deviation almost 2.4 times that of the set with no spatial correlation.

Even this relatively small number of scattering simulations suggest that while the means from the two sets may be difficult to differentiate in the absence of other information, deviations from their respective mean (calculated at the extremes of the volume where sensors could most easily be placed) are likely to be larger in the presence of spatial correlation. It is worth noting that in both panels (c) and (d) of Figure 5.11, the LES-positioned mean (yellow dashed vertical line) is nearly outside the limits of the grey-filled region. This means that the average direct and diffuse forward flux expected under typical cloud chamber mixing cloud conditions are almost a full standard deviation away from the mean expected in the absence of spatial correlation.

5.5.3 Using ratios of flux results as an alternative analysis tool

The deviations in flux results can be portrayed another way; the variation within each set of 10 simulations from the ensemble mean can be seen by dividing the flux component family of curves by their respective ensemble average. The standard deviation comparison shown in Figure 5.12 details the wider variation from mean when the LES spatial positions are employed (light grey fill and solid black stairstep plot) relative to the use of uniformly random droplet locations (indicated with dark grey fill and dotted red stairstep plot). Since both sets of scattering simulation results are normalized by their respective means, the deviations seen in the two flux distributions are depicted about 1; this is done to highlight the difference in standard deviation (rather than similarity or dissimilarity in flux means).

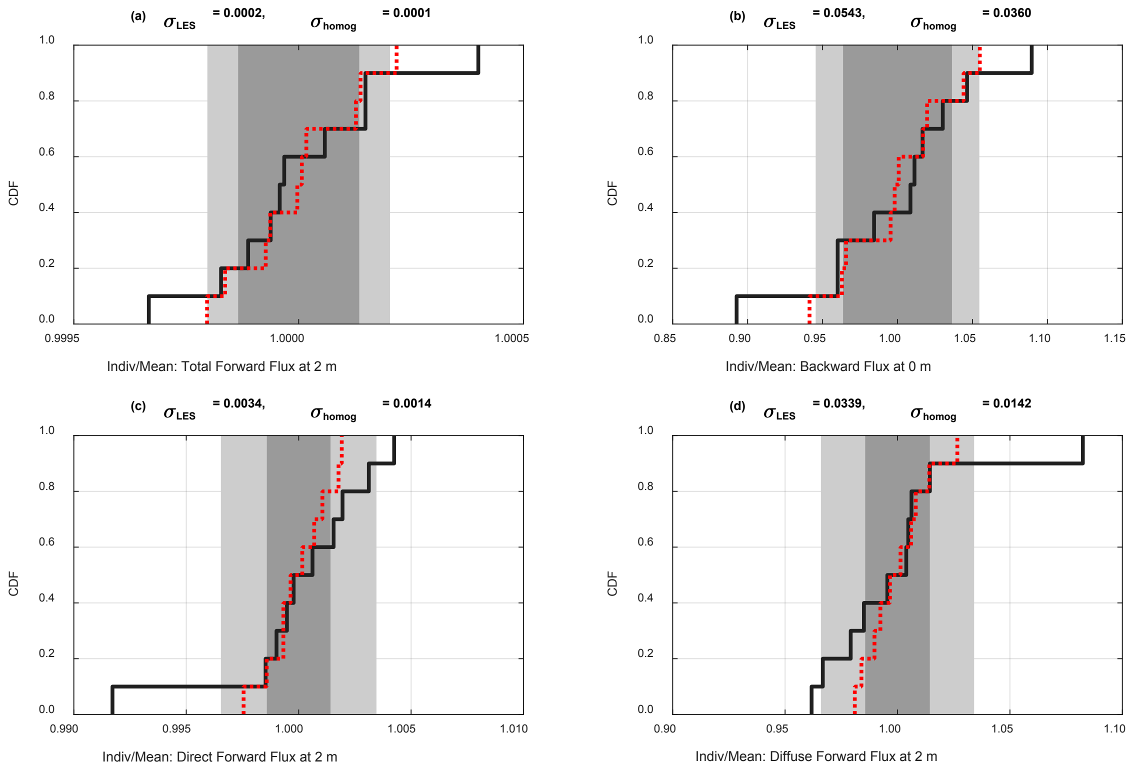

Figure 5.12. Cumulative distribution functions (CDF) computed from propagation endpoints of the individual flux curves from both the LES-position and random position sets, normalized by ensemble mean of each set. Standard deviations, computed from the endpoint values of each set of 10 scattering simulations, are shown above each panel. Since each set has been normalized by the ensemble mean, these ratios are centered about one.

Another way to view the variation caused by spatial correlation is to normalize the 10 individual LES-positioned scattering results by their uniformly random spatial counterpart, curve by curve, instead of their ensemble mean. Using a curve-by-curve, point-by-point division between LES-correlated and spatially uncorrelated results, a ratio can be computed which shows the depth-dependent deviation due only to droplet location (as particle size distributions are identical for both numerator and denominator). The results of these curve-by-curve ratio calculations are shown in Figure 5.13. Values of one indicate a perfect match at a given physical depth, suggesting negligible impact from spatial correlation, while values above and below one suggest increases and decreases (respectively) from the homogeneous case due to spatial correlation. Effects of spatial correlation are somewhat exaggerated for backward and diffuse forward flux since division by small flux numbers for the same absolute flux difference results in a larger deviation ratio.

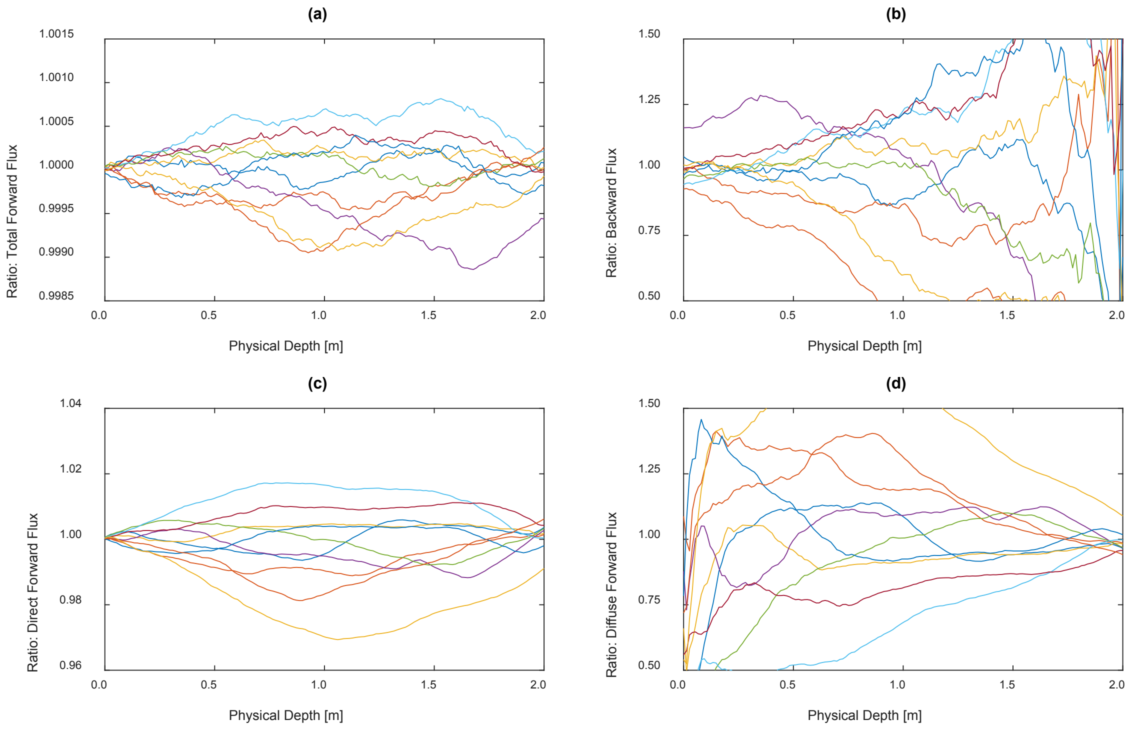

Figure 5.13. Point-by-point ratios calculated between results from LES-positioned droplet locations and those where uniformly random particle locations are used, shown as a function of physical depth. Values of 1 indicate a perfect match at a given physical depth, suggesting negligible impact from spatial correlation. Values above and below 1 suggest increases and decreases (respectively) from the homogeneous case due to spatial correlation. Note that the impact of spatial correlation is much larger in the center of the chamber, while the ratio curves tend to converge at the propagation endpoints (since the effective optical thickness values are very similar).

Examining these ratio results at the most convenient sensor locations (a depth of 2 m for all forward flux components, and a depth of 0 m for backward flux) allows us to estimate both the steady and variable impacts of spatial correlation. Positive shifts of the mean (ratios above 1) correspond to increases in average flux sensed at that location, while negative shifts (ratios below 1) indicate a reduction in average flux. Larger standard deviations, indicate higher fluctuations about the mean flux ratios, represent a more variable impact of spatial clustering. Table 5-1 summarizes the mean and standard deviation flux ratio values for the flux components shown in Figure 5.13. The backward and diffuse forward flux components are more impacted by from spatial correlation, while the impact on total forward and direct flux is less variable.

Table 5-1. Mean and standard deviation of flux ratios computed from the propagation endpoints of the flux ratio component curves (see Figure 5.13; probable sensor locations are at a depth of 2 m for forward flux components, and a depth of 0 m for backward flux).). Values above and below 1 suggest variations in direct and diffuse radiative transfer caused by spatial correlation. Means shifted away from one indicate average increases or decreases in flux, while standard deviation differences suggest the amount of variation in the impact of spatial correlation.

	Total Forward Flux Ratio	**Direct Forward Flux Ratio**	**Diffuse Forward Flux Ratio**	**Backward Flux Ratio**
Mean Value	1.000	1.001	0.988	1.004
Standard Deviation	0.0002	0.0042	0.0417	0.0657

5.6 Discussion & Conclusions

5.6.1 Summary and interpretation of results

Radiative transfer through a dilute medium, and the resulting optical transmissivity, is dependent on the number and size of particles in the distribution. If spatial correlations exist in particle locations, clusters and voids may exist on scales of the same order as or smaller than the optical mean free path (as defined for a uniform medium). In the scattering-dominated regime where absorption is essentially non-existent, radiation is either transmitted directly (without any particle interaction) or diffusely (photons change propagation direction but continue traversing the medium).

In this work, we have investigated direct and diffuse radiative transfer in a medium with spatially correlated scattering particles using a ballistic photon MCRT model. Our simulations explored the forward-dominant scattering regime that is typical of atmospheric clouds. The results are framed in the context of direct and diffuse forward and backward fluxes. Polydisperse LES particle distributions were generated with boundary conditions realizable in the Pi Cloud Chamber to aid the design of an experimental setup meant to measure the presence and impact of spatial correlation.

We found much more cloud-to-cloud variation when the LES-positioned droplet locations were employed (as opposed to uniformly random positions). This was especially evident in the center of the clouds at a physical depth of one meter (see Figure 5.6 and Figure 5.7), but the impact of spatial correlation was still apparent at the propagation endpoints (edges of the confined geometry). The change in mean total forward flux and backward flux for the ten cloud sections analyzed (chosen for their estimated optical thickness of 0.1) was negligible. Panels (a) and (b) of Figure 5.11 indicate that while the standard deviation of these flux components is 1.5-2x larger, the means are essentially the same.

However, the direct and diffuse forward flux results shown respectively in panels (c) and (d) vary in both mean and standard deviation. The standard deviation of the results set with LES-positioned droplets is approximately 2.5x larger than when spatial correlation is removed by using uniformly random particle locations. Additionally, the mean of these flux components are separated sufficiently such that the mean values of the LES-positioned results are almost a standard deviation away from the mean values from the uncorrelated distributions. If we denote the spatially correlated and uncorrelated direct flux means values (respectively) as μ_{LES} and μ_{homog}, and the standard deviation values as σ_{LES} and σ_{homog}, we find that the direct and diffuse forward flux means are related by the expressions

$$\mu_{LES_{direct}} \cong \mu_{homog_{direct}} + \sigma_{homog_{direct}} \tag{36}$$

and

$$\mu_{LES_{diffForw}} \cong \mu_{homog_{diffForw}} - \sigma_{homog_{diffForw}}. \tag{37}$$

With flux means separated by 1-2% and significantly different standard deviations, it seems that the direct and diffuse forward flux components are the most differentiable. This conclusion is consistent with the findings of a recent study (Packard et al., 2019) even though that work focused on monodisperse distributions and the current study employs realistic polydisperse distributions from large eddy simulations (LES).

When the entire set of LES-positioned results are normalized by the uncorrelated results, curve-by-curve at each physical depth along the propagation path, the means of the resulting flux components ratios indicate the average fractional increase or decrease in radiative transfer due to spatial correlation. The mean flux ratios listed in Table 5-1 show that while the total forward flux is essentially unchanged, the flux ratios of the direct, diffuse forward and backward components are 1.001, 0.988 and 1.004 (respectively). While the backward flux has a larger percentage change than the direct flux, the absolute difference is very small and might require a high signal-to-noise ratio (SNR) to measure with confidence. The largest percentage change is the reduction in diffuse forward flux, due to the fact that while the absolute differences in the direct and diffuse forward flux are similar, the denominator is smaller for the diffuse forward (9% vs. 90% for direct). The flux ratio standard deviation values given in Table 5-1 suggest the variation in impact on flux ratio due to spatial correlation.

Focusing on a single LES-positioned cloud subsample and a corresponding uncorrelated uniformly random cloud with the same particle size distribution function, we can examine variations in the spatial distributions themselves. Figure 5.9 shows the variation in mean number density and optical thickness as a function of physical depth into the clouds, with each two meter propagation path divided into half-meter slabs. The high density and low density regions apparent in the LES series in both panels help explain the depth-dependent flux differences seen in the other results figures, since localized concentration discrepancies lead to variations in direct and diffuse forward flux. The LES-induced increases and decreases in number density and optical thickness relative to the uniformly random series can be used to understand the yellow curve shown in Figure 5.6 and Figure 5.13, where direct flux decreases (relative to the uniformly random case) through the first two slabs before that trend reverses during the second half of the propagation path. The opposite trend is evident in diffuse forward flux, which increases (relative to the spatially uncorrelated case) in the first meter and then returns back during the second meter.

5.6.2 Implications for future laboratory experimentation

The flux results presented in this work suggest some possible experimental setups that could be successful at detecting the presence (and potentially, the severity) of particle clustering. In the Pi Chamber owned and operated by Michigan Technological University, mixing clouds can be sustained for hours and the particle size distribution function can be measured with Phase Doppler Anemometry (PDA) throughout the life of the cloud. A normally incident collimated visible light beam could be used to illuminate the chamber-confined cloud, and the total forward flux could be monitored on the opposite side of the chamber. Speed of light measurements means that a sufficiently large number of values can be recorded to ensure the frozen field assumption is valid. As the mixing cloud changes over time, the effective optical thickness (measured using the fractional amount of light exiting the chamber after propagating through the particle distribution) will vary as well. By measuring the direct and diffuse forward flux while monitoring total forward flux, conditioning based on total forward flux (and, as a result, total effective optical thickness) becomes possible. This would allow analysis of the statistics (e.g., mean and standard deviation) of the forward flux components for cloud paths with the same optical thickness (as measured using total forward flux). These means and standard deviations could be compared to values predicted using the measured particle size distribution function and a uniformly random position assumption to test the likelihood (and possibly estimate the magnitude) of particle clustering.

Another possible laboratory setup for a cloud chamber experiment to explore particle clustering would be to employ a series of mirrors and one or more beam splitters. This would allow some interesting experiments to be performed. One such test might be to compare the flux components measured during a single (two meter) propagation path to values recorded after a double pass through the chamber (photons which have traversed the chamber and then back again for a total propagation distance of four meters). This would test whether the statistics of the double-pass beam can be explained by an increased propagation distance through the same particle distribution (homogeneous assumption); deviations from this would suggest a difference in optical paths such as variations in voids and clusters.

A variation of this test would be to measure two different double-pass beams, one that is re-routed back through the same optical path and another that is redirected such that the second pass traverses a different region of the mixing cloud. If the cloud volume is indeed homogeneous, both double pass beams should register similar statistics. However, statistically significant differences between the two would call into question assumptions about the entire cloud volume being homogeneous (in terms of local number density).

6 Summary and Future Work

6.1 Summary and future work concerning optical blurring due to aerosol scattering

This work deals with contributions from aerosol scattering to the problem of blurring and contrast reduction in measured optical images. An analytic theoretical modulation transfer function can be computed which includes atmospheric attenuation, diffraction effects, and small-angle aerosol scattering which results from the near-forward scattering of light by particles large compared to the wavelength. This aerosol MTF, which assumes an aperture diffraction-limited case, is composed of two primary components. The first is a broad pedestal created by an attenuated version of the diffraction MTF whose peak magnitude is lowered as optical depth increases. The second aerosol MTF component is a decaying exponential located at small spatial frequencies, created by scattered light spread over a portion of the image plane. The spatial frequency at which this indirect light ceases to contribute in a significant way is reduced when aerosol modal radius decreases. These two components comprise the total MTF, which includes both aerosol and imaging system artifacts.

The significance of blurring due to aerosol scattering is not agreed upon in the literature, and this apparent controversy appears to focus on the severity of the phenomenon and shortcomings of aerosol experiments meant to settle this debate (Bissonnette, 1992; McDonald et al., 1992; D. Sadot and Kopeika, 1993; Bruscaglioni et al., 1993; Dan Sadot and Kopeika, 1993; Kopeika and Sadot, 1995; Dror and Kopeika, 1995; Ben Dor et al., 1997; Kopeika, 1997; Kopeika et al., 1998; Eismann and LeMaster, 2013). There are relatively few published measurements of the impact of aerosol scattering, and they tend to focus on specific aspects of the full problem. Most significantly, detailed comparisons between theory and measurements are challenging because characterization of conditions in the atmosphere is challenging, and uncertain assumptions must be made regarding spatial and temporal uniformity (i.e., statistical homogeneity or stationarity).

After detailing theoretical MTF expressions to predict the impact of aerosol scattering on measured imagery, we showed the results from a closure experiment using the MTU cloud chamber. Knife-edge imagery was captured through a controlled expansion cloud while the particle size distribution was measured directly. Experimental aerosol MTFs were calculated from these images and compared to theoretical predictions made using the measured atmospheric conditions. Predicted MTF responses for both the control and aerosol scenarios were made with and without finite bit-depth detector limitations, and the impact of quantization and noise floor was illustrated. These predicted aerosol MTF curves, created with atmospheric properties based on measured expansion cloud distributions, were compared to MTF responses measured in the cloud chamber.

According to analysis of MTF measurements performed in numerous laboratories (Williams and Becklund, 2010), measuring a modulation transfer function to within 5%

of a theoretically-predicted curve demonstrates sufficient accuracy. The measured control MTF response (prior to quantization), obtained with a manual focus procedure, was within 7% of the diffraction-limited MTF that would be expected under ideal conditions including perfect focus, absence of lens aberrations, uniform knife-edge illumination, etc. After quantization was applied to incorporate finite bit-depth detector limitations, the theoretical control MTFs closely resembled the measured control MTF. The theoretical control MTF with simulated 13-bit quantization was an almost exact match when compared to the measured control MTF.

The (ideal) predicted aerosol MTFs showed only a slight sensitivity to small variations in dominant droplet radius, with moderate MTF response changes due to various optical depths. However, bit-depth quantizations of the ideal aerosol MTFs displayed high sensitivity to changes in droplet radius. In contrast, the ideal and quantized aerosol MTFs responded similarly to changes in optical depth. Our investigation revealed that the MTF response modifications depended on how far from the centroid of the PSF the dynamic range cutoff occurred and how much PSF energy was contained in the portion below the detector noise floor. Other things being equal, moving the noise floor cutoff closer to the PSF center increased the difference between the ideal and quantized MTF. Loss of all but the Bessel function near the PSF centroid means the resulting MTF is essentially the diffraction-limited control case, which is sensible given that the indirect (scattered) light is spread over the image plane (not well focused). Removing this scattered contribution diminishes the discrepancy between aerosol and control MTF. This means that with the expansion cloud conditions present in the chamber, aerosol scattering is an evident but subtle contributing effect (Eismann and LeMaster, 2013) that is significantly impacted by the optical imaging system used to measure it. In an atmospheric context, the significance of aerosol-induced blurring would depend not only on the details of the aerosols and propagation path length but also on the hardware configuration of the imaging system, especially the dynamic range of its detector.

The (quantized) predicted MTFs matched the measured aerosol curves reasonably well, disagreeing by less than 10% for a single combination of droplet radius and optical depth. Due to the sensitivity to the droplet radius selected for the predicted curves, and the uncertainty of the exact dominant droplet radius for each of the three expansion clouds, this amount of prediction error is encouraging. Theoretical aerosol MTFs computed from a small range of droplet radii based on values in Table 2-1 easily bound the measured MTFs everywhere but below 3×10^{-2} cycles per milliradian, which is approximately the limit of reliable information from the detector footprint used for image capture. The authors believe that the theoretical expressions, which utilize a single, modal particle radius, are likely most accurate for nearly-monodisperse particle distributions. For strongly polydisperse distributions such as our expansion clouds, which were measured to have a broad distribution of droplet radii with similarly-dominant number densities, the choice of a single radius is apparently insufficient when sensitivity to this value is considered. This further explains why the various measured aerosol MTFs were similar; the particle distributions of the generated expansion clouds largely overlapped and often had several strongly-contributing adjacent radius bins.

Overall, the concept of closure between MTFs obtained from directly-measured images and MTFs calculated from theory using measured cloud properties in a laboratory setting, has been demonstrated to be qualitatively successful. The comparison led to several findings: the theoretical expression for MTF is likely overly simplistic and does not account for broad particle size distributions; the relevance of optical blurring from light scattering by aerosol particles depends sensitively on the properties of both the particles and the imaging system; regarding the latter, the digital dynamic range was found to be especially relevant, having the ability to reveal or mask aerosol blurring effects for realistic bit levels.

In future experiments a wider range of cloud conditions could be explored, especially larger values of optical depth and a broader range of particle sizes. Further, the thermal convection capability of the cloud chamber will enable exploration of the influence of turbulence, simultaneously with particles, thereby testing the common assumption of independence and additivity. On the instrumentation side, as better sensors become available, it would be instructive to explore the influence of camera digital dynamic range. A higher bit depth detector would lead to a lower noise floor, so that the aerosol MTF could be measured more directly with less contamination from the electronics of the imaging system. Additionally, a larger detector cutoff frequency would allow the imaging aperture to be enlarged without additional aliasing. This would potentially allow a wider range of scattering angles to impact the aerosol measurements.

6.2 Summary and future work concerning particle clustering, depth-dependent flux and the role of RDFs

The influence of spatial inhomogeneity (in particle fields) on three-dimensional radiative transfer has been considered in depth, especially for the limit in which the scale of the inhomogeneity is larger than the mean free path defined for the medium. Pioneering work by Kostinski (2001) makes clear, however, that the validity of fundamental assumptions of the continuum approach to radiative transfer is questionable when correlations in a discrete-particulate medium are considered. In atmospheric clouds, typical mean free paths for regimes dominated by scattering (e.g., visible light) are of order 100 m; this means that, essentially, the entire turbulence inertial subrange lies at smaller scales. Entrainment and mixing processes generate strong spatial correlations in droplet positions from the ~100-m energy injection scale to the ~1-mm dissipation scale, and inertial clustering generates spatial correlations from the ~1-cm scale down to the ~10 µm scale of a single particle diameter (Wyngaard, 1992, 2010b).

The question of how these sub-free-path-scale correlations might influence radiative transfer has been previously studied by several groups for the absorbing-particle limit (Kostinski, 2001; Shaw et al., 2002a; Larsen and Clark, 2014; Frankel et al., 2017). In this work we have explored the regime in which light scattering is dominant ($\omega \sim 1$), and specifically for particles larger than the illuminating wavelength for which forward scattering is pronounced; this is the relevant regime for atmospheric clouds and visible/near-IR radiation. The results of our study suggest that the degree to which there is a deviation from standard radiative transfer (using the medium-averaged optical properties, such as mean free path) can be quantified through the radial distribution function. This implies that knowledge of the RDF resulting from inertial clustering and turbulent mixing in atmospheric clouds would be valuable (Larsen et al., 2018). The RDF, as a two-particle correlation function, is a first step; eventually it will be insightful to consider the possible relevance of multi-particle correlations on light propagation.

This work has focused on the influence of clustering at scales below the mean free path of the radiation, for optical depths up to order unity. This emphasis on optical thicknesses near $\tau = 1$ is partially due to our desire to compare numerical predictions to laboratory measurements that could be made in a controlled environment such as the Pi chamber (Chang et al., 2016). Expansion clouds in the cloud chamber have been generated with measured optical depth in the range $0.5 < \tau < 1.0$ (Packard et al., 2016, 2018), motivating our focus on this region. Implications of our findings for larger scales, such as cloud remote sensing or energy budgets, will require consideration of cloud organization at the full range of scales. For example, it is already widely appreciated that clustering on spatial scales large in comparison to the photon mean free path is of significance in practical applications. It is known, however, that the turbulent energy cascade stretches down to the 1 mm scale in the atmosphere, so clouds can be assumed to be non-uniform far below the scale of a mean free path.

One logical next step is validation of the MCRT results by direct comparison with measurements recorded in the Pi cloud chamber. Characterization of actual clustering strength in natural clouds will be required to put the chamber measurements properly into atmospheric context, since only with knowledge of the atmospheric boundary conditions can radiative transfer predictions be usefully compared to laboratory measurements. This kind of comparison will allow the overall approach of MCRT methods to be assessed; although they are widely used in applied radiative transfer, they are known to neglect the detailed electromagnetic treatment that is potentially necessary for full representation of propagation in a correlated medium (e.g., Mishchenko et al. 2016). Determining shortcomings in the MCRT approach will be greatly helped by having confidence in both measurements of atmospheric inputs (e.g., particle size distribution and particle clustering) and directional radiative transfer outputs (e.g., direct and diffuse flux). Experimental results will be the ultimate arbiter.

In some scenarios we examined, the changes to direct and diffuse radiation are nearly compensating (i.e., direct flux increases and diffuse forward flux decreases are essentially offsetting). Do such results suggest that there is no meaningful impact on radiative transfer due to particle clustering? We believe the answer to this question depends on the problem under consideration: for any problem depending on directional properties of the radiation field, the details of direct versus diffuse will be of significance.

6.3 Summary and future work concerning the detection of particle clustering in Pi Chamber-generated clouds

In our further investigations of particle clustering and how it impacts direct and diffuse radiative transfer, prior to a comparison between computations and experimental observations, we simulated radiative transfer in chamber-realistic boundary conditions to predict the effects of clustering and how best to conduct such a sensitive experiment. Subtle effects can be notoriously difficult to measure, and simulation is often an invaluable tool for designers of laboratory experiments. We sought to determine what and where measurements should be made, and performing this study numerically (rather than risking a series of ill-conceived experiments) was a fruitful path of inquiry.

As a consequence, the geometry chosen in our study was motivated by the desire to explore how best to study optical propagation through a turbulent cloud in the laboratory, since the Pi chamber has the advantage of well-characterized and steady-state cloud and turbulence conditions. We used LES-generated, polydisperse particle fields to study the impact of droplet clustering on directional propagation of visible light, and noted that both mean direct and diffuse flux and the standard deviation about those means are impacted, even by atmospheric clouds realistic for our laboratory chamber. Even with less extreme particle clustering than our Matérn study, it would seem a measurable impact could be observed with the use of proper sensing equipment.

For example, with a nominal (expected) optical depth of 0.1 (typical for a sustainable mixing cloud), direct flux was observed to increase from less than 90.5% of incident illumination to 90.6% when realistic clustering is present. Furthermore, the standard deviation of the same measurement increased from 0.0013 to 0.0031 (a factor of 2.4). In a similar fashion, the mean diffuse forward flux decreased from 9.15% of incident illumination to 9.03%, but the standard deviation increased from 0.0013 to 0.0031 (same factor of 2.4). Sensing equipment sensitive enough to measure the levels of illumination of interest, with sufficient resolution to reliably detect variations and build flux histograms with confidence, should be capable of discriminating between subtly different means with significantly dissimilar standard deviations.

It should be noted that while our analysis employed the Henyey-Greenstein scattering phase function, our Monte Carlo software is capable of using full Mie scattering phase functions if desired. While depth-dependent flux results from these two scattering methods were compared, this evaluation was performed using an uncorrelated monodisperse particle field. Direct and diffuse forward results were essentially identical, though backward flux did differ (due to phase functions). A logical progression of our work would be to analyze polydisperse LES particle fields with the aid of Mie scattering phase functions to determine their impact on direct and diffuse radiative transfer predictions.

Chapter 5 explained that the smallest LES grid resolution was 3.125 cm; particle locations within these grids were unresolved and thus given random positions within the appropriate grid. During a future investigation, it may be possible to implement a clustering algorithm - within a grid, or perhaps several adjacent grids - for the purpose of adding further spatial correlation to the exported LES particle fields. Perhaps a Matérn process (similar to that described in chapter 4) could be used to create clusters with the appropriate number of particles. Results from these additionally-clustered particle fields could be compared to those predicted using random-within-a-grid particle positions.

Recent investigations into free-space optical (FSO) communication through atmospheric scattering media (e.g., haze, fog, cloud, rain) have suggested that transmission losses and reductions in data rates are problematic (Khalighi and Uysal, 2014). The culprit is believed to be partially caused by temporal spreading of the transmitted pulses propagating through the atmosphere, due to scattering-induced diffusion (Shin Hong et al., 1977; Kim et al., 1999). The strongly attenuated ballistic signal is detected upon direct time-of-flight arrival, but temporally-delayed energy arrives (after this initial ballistic energy) as it propagated diffusely through the atmosphere. Essentially, multiply-scattered energy arrives later than the initial (direct) ballistic energy. A common assumption is that this delayed signal can be described as the arrival of a slowly decaying late-time diffusion (LTD) tail. The temporal spread of this tail, given by the expression $\Delta t_{LTD} \sim R^2/(c \cdot l)$, is inversely proportional to the speed of light, c, and mean-free-path in the medium, l; it is proportional to the square of the propagation distance, R (Bleszynski et al., 2018). Through atmospheric clouds or fog, Δt_{LTD} may exceed a microsecond scale; for the sake of comparison, Δt_{LTD} in the MTU Pi chamber might range from less than a nanosecond (in the case of a mixing cloud) to several nanoseconds (in the case of an expansion cloud).

However, recent time-dependent radiative transfer equation (RTE) analysis has revealed that scatterers large compared to the optical wavelength contribute to the development of an additional early-time diffusion (ETD) component which arrives immediately after the ballistic component (Bleszynski et al., 2014). This component is due to multiple small-angle scattering inside the forward-scattering lobe of the phase function and is related to the optical wavelength, particle radius and mean-free-path of the medium. This ETD component may be several orders of magnitude shorter than the more-discussed LTD (Bleszynski et al., 2018); in the case of the Pi chamber, Δt_{ETD} might be on the order of femtoseconds. The hope is that by isolating the ETD with proper high-pass filtering, higher FSO communication data rates and significantly less attenuation may be possible.

In their analysis, Bleszynski et al. (2018) present time-dependent RTE predictions of the ETD and LTD signals and their relative intensities. A logical extension of our MCRT scattering code would be to preserve and export ray-traced photon paths, which would enable the calculation and visualization of photon travel-time distributions. By summing all the consecutive segments of each scattered ray, a total propagation time could be computed for each photon path. These path lengths, each with arrival times greater than that of the initial (direct) energy, could be used to create a distribution of arrival times. This distribution could be normalized by the total number of rays cast, which would provide the ability to determine the relative strength of the ballistic (direct) and delayed (diffuse) transmissions as a function of scattering medium properties.

To this point our published results have focused on two-stream flux components; periodic wall boundaries were used to efficiently create a semi-infinite scattering medium with a tractable number of particles. However, scattering angles and ray segments are recorded internally and could be preserved to investigate angular energy distribution and arrival times for comparison to time-dependent RTE predictions for similar atmospheric problems. While our recent work employed the HG phase function for simplicity, our MCRT code is capable of using an accurate Mie scattering phase function to fully represent the small-angle behavior induce by the forward-scattering lobe of large (relative to wavelength) scatterers. By placing a theoretical detector opposite the virtual illumination source, the ray-tracing code could use received energy (as a function of arrival time) to predict if the ETD and LTD “tails” are consistent with published time-dependent RTE predictions.

7 Reference List

Banko, A.J., Villafañe, L., Kim, J.H., Esmaily, M., Eaton, J.K., 2019. Stochastic modeling of direct radiation transmission in particle-laden turbulent flow. J. Quant. Spectrosc. Radiat. Transf. 226, 1–18. https://doi.org/10.1016/j.jqsrt.2019.01.005

Barker, H.W., 1992. Solar Radiative Transfer Through Clouds Possessing Isotropic Variable Extinction Coefficient. Q. J. R. Meteorol. Soc. 118, 1145–1162. https://doi.org/10.1002/qj.49711850807

Ben Dor, B., Devir, A.D., Shaviv, G., Bruscaglioni, P., Donelli, P., Ismaelli, A., 1997. Atmospheric scattering effect on spatial resolution of imaging systems. J. Opt. Soc. Am. A 14, 1329. https://doi.org/10.1364/JOSAA.14.001329

Bissonnette, L.R., 1994. Imaging through the atmosphere: practical instrumentation-based theory and verification of aerosol modulation transfer function: comment. JOSA A 11, 1175–1179. https://doi.org/10.1364/JOSAA.11.001175

Bissonnette, L.R., 1992. Imaging through fog and rain. Opt. Eng. 31, 1045–1052. https://doi.org/10.1117/12.56145

Bleszynski, E., Bleszynski, M., Jaroszewicz, T., 2018. Enhancing early-time diffusion through beam collimation in pulse propagation in sparse discrete random media. Opt. Lett. 43, 3762–3765. https://doi.org/10.1364/OL.43.003762

Bleszynski, E., Bleszynski, M., Jaroszewicz, T., 2014. Early-time diffusion in pulse propagation through dilute random media. Opt. Lett. 39, 5862–5865. https://doi.org/10.1364/OL.39.005862

Bohren, C.F., Clothiaux, E.E., 2011. Fundamentals of Atmospheric Radiation: An Introduction with 400 Problems. Wiley-VCH, Weinheim.

Bohren, C.F., Huffman, D.R., 2004. Absorption and scattering of light by small particles. Wiley-VCH Verlag, Weinheim.

Boreman, G.D., 2001. Modulation transfer function in optical and electro-optical systems. SPIE Press, Bellingham, Wash., USA.

Borovoi, A.G., 1984. Radiative transfer in inhomogeneous media. Dokl. Akad. Nauk SSSR 276, 1374–1378.

Bruscaglioni, P., Donelli, P., Ismaelli, A., Zaccanti, G., 1993. Monte Carlo calculations of the modulation transfer function of an optical system operating in a turbid medium. Appl. Opt. 32, 2813. https://doi.org/10.1364/AO.32.002813

Cairns, B., Lacis, A.A., Carlson, B.E., 2000. Absorption within Inhomogeneous Clouds and Its Parameterization in General Circulation Models. J. Atmospheric Sci. 57, 700–714. https://doi.org/10.1175/1520-0469(2000)057<0700:AWICAI>2.0.CO;2

Chandrakar, K.K., Cantrell, W., Chang, K., Ciochetto, D., Niedermeier, D., Ovchinnikov, M., Shaw, R.A., Yang, F., 2016. Aerosol indirect effect from turbulence-induced broadening of cloud-droplet size distributions. Proc. Natl. Acad. Sci. 113, 14243–14248. https://doi.org/10.1073/pnas.1612686113

Chandrakar, K.K., Cantrell, W., Ciochetto, D., Karki, S., Kinney., G., Shaw, R.A., 2017. Aerosol removal and cloud collapse accelerated by supersaturation fluctuations in turbulence. Geophys. Res. Lett. 44, 4359–4367. https://doi.org/10.1002/2017GL072762

Chang, K., Bench, J., Brege, M., Cantrell, W., Chandrakar, K., Ciochetto, D., Mazzoleni, C., Mazzoleni, L.R., Niedermeier, D., Shaw, R.A., 2016. A laboratory facility to study gas-aerosol-cloud interactions in a turbulent environment: The Π Chamber. Bull. Am. Meteorol. Soc. https://doi.org/10.1175/BAMS-D-15-00203.1

Chiu, S.N., Stoyan, D., Kendall, W.S., Mecke, J., 2013. Stochastic geometry and its applications, 3rd edition. ed. Chichester : Wiley.

Chun, J., Koch, D.L., Rani, S.L., Ahluwalia, A., Collins, L.R., 2005. Clustering of aerosol particles in isotropic turbulence. J. Fluid Mech. 536, 219–251. https://doi.org/10.1017/S0022112005004568

Cole, J.N.S., 2005. Assessing the importance of unresolved cloud-radiation interactions in atmospheric global climate models using the multiscale modelling framework (Doctoral Thesis). Department of Meteorology, The Pennsylvania State University.

Collins, D.G., Blättner, W.G., Wells, M.B., Horak, H.G., 1972. Backward Monte Carlo Calculations of the Polarization Characteristics of the Radiation Emerging from Spherical-Shell Atmospheres. Appl. Opt. 11, 2684–2696. https://doi.org/10.1364/AO.11.002684

Danielson, R.E., Moore, D.R., van de Hulst, H.C., 1969. The Transfer of Visible Radiation through Clouds. J. Atmospheric Sci. 26, 1078–1087. https://doi.org/10.1175/1520-0469(1969)026<1078:TTOVRT>2.0.CO;2

Davis, A.B., 2006. Effective Propagation Kernels in Structured Media with Broad Spatial Correlations, Illustration with Large-Scale Transport of Solar Photons Through Cloudy Atmospheres, in: Graziani, F. (Ed.), Computational Methods in Transport, Lecture Notes in Computational Science and Engineering. Springer Berlin Heidelberg, pp. 85–140.

Davis, A.B., Marshak, A., 2004. Photon propagation in heterogeneous optical media with spatial correlations: enhanced mean-free-paths and wider-than-exponential free-path distributions. J. Quant. Spectrosc. Radiat. Transf. 84, 3–34. https://doi.org/10.1016/S0022-4073(03)00114-6

Davis, A.B., Marshak, A., Gerber, H., Wiscombe, W.J., 1999. Horizontal structure of marine boundary layer clouds from centimeter to kilometer scales. J. Geophys. Res. Atmospheres 104, 6123–6144. https://doi.org/10.1029/1998JD200078

Deirmendjian, D., 1969. Electromagnetic scattering on spherical polydispersions. American Elsevier Pub. Co., New York.

Desai, N., Chandrakar, K.K., Chang, K., Cantrell, W., Shaw, R.A., 2017. Influence of microphysical variability on stochastic condensation in a turbulent laboratory cloud. J. Atmospheric Sci. 75, 189–201. https://doi.org/10.1175/JAS-D-17-0158.1

Donelli, P., Bruscaglioni, P., Ismaelli, A., Zaccanti, G., 1991. Experimental Validation of a Monte Carlo Procedure for the Evaluation of the Effect of a Turbid Medium on the Point Spread Function of an Optical System. J. Mod. Opt. 38, 2189–2201. https://doi.org/10.1080/09500349114552271

Dror, I., Kopeika, N.S., 1995. Experimental comparison of turbulence modulation transfer function and aerosol modulation transfer function through the open atmosphere. J. Opt. Soc. Am. A 12, 970. https://doi.org/10.1364/JOSAA.12.000970

Eismann, M.T., LeMaster, D.A., 2013. Aerosol modulation transfer function model for passive long-range imaging over a nonuniform atmospheric path. Opt. Eng. 52, 046201. https://doi.org/10.1117/1.OE.52.4.046201

Frankel, A., Iaccarino, G., Mani, A., 2017. Optical depth in particle-laden turbulent flows. J. Quant. Spectrosc. Radiat. Transf. 201, 10–16. https://doi.org/10.1016/j.jqsrt.2017.06.029

Frankel, A., Iaccarino, G., Mani, A., 2016. Convergence of the Bouguer–Beer law for radiation extinction in particulate media. J. Quant. Spectrosc. Radiat. Transf. 182, 45–54. https://doi.org/10.1016/j.jqsrt.2016.05.009

Goodman, J.W., 2005. Introduction to Fourier Optics, 3rd ed. ed. Roberts and Company Publishers, Englewood, CO.

Grainger, R.G., 2012. Some Useful Formulae for Aerosol Size Distributions and Optical Properties.

Hanafy, M.E., Roggemann, M.C., Guney, D.O., 2015. Reconstruction of images degraded by aerosol scattering and measurement noise. Opt. Eng. 54, 033101. https://doi.org/10.1117/1.OE.54.3.033101

Hanafy, M.E., Roggemann, M.C., Guney, D.O., 2014. Detailed effects of scattering and absorption by haze and aerosols in the atmosphere on the average point spread function of an imaging system. J. Opt. Soc. Am. A 31, 1312–1319. https://doi.org/10.1364/JOSAA.31.001312

Hecht, E., 2002. Optics, 4th ed. ed. Addison-Wesley, Reading, Mass.

Henyey, L.G., Greenstein, J.L., 1941. Diffuse radiation in the galaxy. Astrophys. J. 93, 70–83. https://doi.org/10.1086/144246

Holst, G.C., 2008. Electro-optical imaging system performance, 5th ed. ed. JCD Pub.; SPIE Optical Engineering Press, Winter Park, FL; Bellingham, Wash.

Holst, G.C., 1998. Testing and evaluation of infrared imaging systems. JCD Pub.; SPIE Optical Engineering Press, Winter Park, FL; Bellingham, WA.

Ishimaru, A., 1997. Wave propagation and scattering in random media. IEEE Press ; Oxford University Press, New York; Oxford; New York.

Ishimaru, A., 1978. Limitation on image resolution imposed by a random medium. Appl. Opt. 17, 348–352. https://doi.org/10.1364/AO.17.000348

Khain, A., Pokrovsky, A., Pinsky, M., Seifert, A., Phillips, V., 2004. Simulation of Effects of Atmospheric Aerosols on Deep Turbulent Convective Clouds Using a Spectral Microphysics Mixed-Phase Cumulus Cloud Model. Part I: Model Description and Possible Applications. J. Atmospheric Sci. 61, 2963–2982. https://doi.org/10.1175/JAS-3350.1

Khairoutdinov, M.F., Randall, D.A., 2003. Cloud Resolving Modeling of the ARM Summer 1997 IOP: Model Formulation, Results, Uncertainties, and Sensitivities. J. Atmospheric Sci. 60, 607–625. https://doi.org/10.1175/1520-0469(2003)060<0607:CRMOTA>2.0.CO;2

Khalighi, M.A., Uysal, M., 2014. Survey on Free Space Optical Communication: A Communication Theory Perspective. IEEE Commun. Surv. Tutor. 16, 2231–2258. https://doi.org/10.1109/comst.2014.2329501

Kim, A.D., Ishimaru, A., Kuga, Y., 1999. Polarimetric pulse propagation through discrete random media, in: Optical Pulse and Beam Propagation. Presented at the Optical Pulse and Beam Propagation, International Society for Optics and Photonics, pp. 101–110. https://doi.org/10.1117/12.351047

Kopeika, N.S., 1997. Aerosol modulation transfer function: an overview, in: SPIE Proc. pp. 214–225. https://doi.org/10.1117/12.283885

Kopeika, N.S., 1987. Imaging Through The Atmosphere For Airborne Reconnaissance. Opt. Eng. 26, 261146-261146-. https://doi.org/10.1117/12.7974208

Kopeika, N.S., 1985. Effects Of Aerosols On Imaging Through The Atmosphere: A Review Of Spatial Frequency And Wavelength Dependent Effects. Opt. Eng. 24, 244707. https://doi.org/10.1117/12.7973557

Kopeika, N.S., 1982. Spatial-frequency- and wavelength-dependent effects of aerosols on the atmospheric modulation transfer function. JOSA 72, 1092–1094. https://doi.org/10.1364/JOSA.72.001092

Kopeika, N.S., Arbel, D., 1999. Imaging through the atmosphere: an overview, in: SPIE Proc. pp. 78–89. https://doi.org/10.1117/12.351045

Kopeika, N.S., Dror, I., Sadot, D., 1998. Causes of atmospheric blur: comment on Atmospheric scattering effect on spatial resolution of imaging systems. J. Opt. Soc. Am. A 15, 3097. https://doi.org/10.1364/JOSAA.15.003097

Kopeika, N.S., Sadot, D., 1995. Imaging through the atmosphere: practical instrumentation-based theory and verification of aerosol modulation transfer function: reply to comment. J. Opt. Soc. Am. A 12, 1017. https://doi.org/10.1364/JOSAA.12.001017

Kopeika, N.S., Solomon, S., Gencay, Y., 1981. Wavelength variation of visible and near-infrared resolution through the atmosphere: dependence on aerosol and meteorological conditions. JOSA 71, 892–901. https://doi.org/10.1364/JOSA.71.000892

Kostinski, A.B., 2002. On the extinction of radiation by a homogeneous but spatially correlated random medium: reply to comment. JOSA A 19, 2521–2525. https://doi.org/10.1364/JOSAA.19.002521

Kostinski, A.B., 2001. On the extinction of radiation by a homogeneous but spatially correlated random medium. JOSA A 18, 1929–1933. https://doi.org/10.1364/JOSAA.18.001929

Kuga, Y., Ishimaru, A., 1986. Modulation transfer function of layered inhomogeneous random media using the small-angle approximation. Appl. Opt. 25, 4382. https://doi.org/10.1364/AO.25.004382

Kuga, Y., Ishimaru, A., 1985. Modulation transfer function and image transmission through randomly distributed spherical particles. J. Opt. Soc. Am. A 2, 2330. https://doi.org/10.1364/JOSAA.2.002330

Landau, L.D., Lifshitz, E.M., 1980. Statistical physics. Butterworth-Heinemann, Oxford, UK.

Larsen, E.W., Vasques, R., 2011. A generalized linear Boltzmann equation for non-classical particle transport. J. Quant. Spectrosc. Radiat. Transf., 2009 International Conference on Mathematics and Computational Methods (M&C 2009) 112, 619–631. https://doi.org/10.1016/j.jqsrt.2010.07.003

Larsen, M., Clark, A., 2014. On the link between particle size and deviations from the Beer–Lambert–Bouguer law for direct transmission. J. Quant. Spectrosc. Radiat. Transf. 133, 646–651. https://doi.org/10.1016/j.jqsrt.2013.10.001

Larsen, M.L., Briner, C.A., Boehner, P., 2014. On the Recovery of 3D Spatial Statistics of Particles from 1D Measurements: Implications for Airborne Instruments. J. Atmospheric Ocean. Technol. 31, 2078–2087. https://doi.org/10.1175/JTECH-D-14-00004.1

Larsen, M.L., Shaw, R.A., 2018. A method for computing the three-dimensional radial distribution function of cloud particles from holographic images. Atmospheric Meas. Tech. 11, 4261–4272. https://doi.org/10.5194/amt-11-4261-2018

Larsen, M.L., Shaw, R.A., Kostinski, A.B., Glienke, S., 2018. Fine-Scale Droplet Clustering in Atmospheric Clouds: 3D Radial Distribution Function from Airborne Digital Holography. Phys. Rev. Lett. 121, 204501. https://doi.org/10.1103/PhysRevLett.121.204501

Li, J., Barker, H., Yang, P., Yi, B., 2015. On the aerosol and cloud phase function expansion moments for radiative transfer simulations. J. Geophys. Res. Atmospheres 120, 12,128-12,142. https://doi.org/10.1002/2015JD023632

Liou, K.-N., 2002. An introduction to atmospheric radiation, 2nd ed. ed. Academic Press, Amsterdam; Boston.

Lu, J., Nordsiek, H., Saw, E.W., Shaw, R.A., 2010. Clustering of Charged Inertial Particles in Turbulence. Phys. Rev. Lett. 104, 184505. https://doi.org/10.1103/PhysRevLett.104.184505

Lutomirski, R.F., 1978. Atmospheric degradation of electrooptical system performance. Appl. Opt. 17, 3915. https://doi.org/10.1364/AO.17.003915

Marchuk, G.I., Mikhailov, G.A., Nazaraliev, M.A., Darbinjan, R.A., Kargin, B.A., Elepov, B.S., 1980. The Monte Carlo Methods in Atmospheric Optics. Springer. https://doi.org/10.1007/978-3-540-35237-2

Marshak, A., Davis, A.B., 2005. 3D Radiative Transfer in Cloudy Atmospheres. Springer, Berlin.

Martínez, V.J., Saar, E., 2002. Statistics of the Galaxy Distribution. CRC Press.

Matérn, B., 1986. Spatial Variation, 2nd ed, Lecture Notes in Statistics. Springer-Verlag, New York.

Matérn, B., 1972. Poisson processes in the plane and related models for clumping and heterogeneity, NATO Advanced Study Institute on Statistical Ecology. Pennsylvania State University.

Matsuda, K., Onishi, R., Kurose, R., Komori, S., 2012. Turbulence effect on cloud radiation. Phys. Rev. Lett. 108, 224502. https://doi.org/10.1103/PhysRevLett.108.224502

McDonald, C., Romero, G., Ortiz, C., Carbajal, J., 1992. Measurement of the aerosol component of the modulation transfer function in desert atmospheres, in: SPIE Proc. pp. 86–98. https://doi.org/10.1117/12.137945

Miles, N.L., Verlinde, J., Clothiaux, E.E., 2000. Cloud Droplet Size Distributions in Low-Level Stratiform Clouds. J. Atmospheric Sci. 57, 295–311. https://doi.org/10.1175/1520-0469(2000)057<0295:CDSDIL>2.0.CO;2

Mishchenko, M.I., 2008. Multiple scattering, radiative transfer, and weak localization in discrete random media: Unified microphysical approach. Rev. Geophys. 46. https://doi.org/10.1029/2007RG000230

Mishchenko, M.I., 2006. Radiative transfer in clouds with small-scale inhomogeneities: Microphysical approach. Geophys. Res. Lett. 33. https://doi.org/10.1029/2006GL026312

Mishchenko, M.I., Dlugach, J.M., Yurkin, M.A., Bi, L., Cairns, B., Liu, L., Panetta, R.L., Travis, L.D., Yang, P., Zakharova, N.T., 2016. First-principles modeling of electromagnetic scattering by discrete and discretely heterogeneous random media. Phys. Rep., First-principles modeling of electromagnetic scattering by discrete and discretely heterogeneous random media 632, 1–75. https://doi.org/10.1016/j.physrep.2016.04.002

Modest, M.F., 1993. Radiative Heat Transfer. McGraw-Hill.

Niedermeier, D., Chang, K., Cantrell, W., Chandrakar, K.K., Ciochetto, D., Shaw, R.A., 2018. Observation of a link between energy dissipation rate and oscillation frequency of the large-scale circulation in dry and moist Rayleigh-B\’enard turbulence. Phys. Rev. Fluids 3, 083501. https://doi.org/10.1103/PhysRevFluids.3.083501

Nugent, P.W., Shaw, J.A., Kehoe, M.R., Smith, C.W., Moon, T.S., Swanson, R.C., 2010. Measuring the modulation transfer function of an imaging spectrometer with rooflines of opportunity. Opt. Eng. 49, 103201. https://doi.org/10.1117/1.3497051

Packard, C.D., Ciochetto, D.S., Cantrell, W.H., Roggemann, M.C., Shaw, R.A., 2016. Measurement of optical blurring in a turbulent cloud chamber, in: Optics in Atmospheric Propagation and Adaptive Systems XIX. Presented at the Optics in Atmospheric Propagation and Adaptive Systems XIX, International Society for Optics and Photonics, p. 100020E. https://doi.org/10.1117/12.2241419

Packard, C.D., Larsen, M.L., Cantrell, W.H., Shaw, R.A., 2019. Light scattering in a spatially-correlated particle field: Role of the radial distribution function. J. Quant. Spectrosc. Radiat. Transf. 236, 106601. https://doi.org/10.1016/j.jqsrt.2019.106601

Packard, C.D., Shaw, R.A., Cantrell, W.H., Kinney, G.M., Roggemann, M.C., Valenzuela, J.R., 2018. Measuring the detector-observed impact of optical blurring due to aerosols in a laboratory cloud chamber. J. Appl. Remote Sens. 12, 042404. https://doi.org/10.1117/1.JRS.12.042404

Pawar, S.S., Arakeri, J.H., 2016. Intensity and angle-of-arrival spectra of laser light propagating through axially homogeneous buoyancy-driven turbulence. Appl. Opt. 55, 5945–5952. https://doi.org/10.1364/AO.55.005945

Petty, G.W., 2002. Area-Average Solar Radiative Transfer in Three-Dimensionally Inhomogeneous Clouds: The Independently Scattering Cloudlet Model. J. Atmospheric Sci. 59, 2910–2929. https://doi.org/10.1175/1520-0469(2002)059<2910:AASRTI>2.0.CO;2

Pharr, M., Humphreys, G., 2004. Physically Based Rendering: From Theory to Implementation. Morgan Kaufmann, San Francisco, CA.

Plass, G.N., Kattawar, G.W., 1968. Monte Carlo Calculations of Light Scattering from Clouds. Appl. Opt. 7, 415–419. https://doi.org/10.1364/AO.7.000415

Reade, W.C., Collins, L.R., 2000. Effect of preferential concentration on turbulent collision rates. Phys. Fluids 12, 2530–2540. https://doi.org/10.1063/1.1288515

Reichenbach, S.E., Park, S.K., Narayanswamy, R., 1991. Characterizing digital image acquisition devices. Opt. Eng. 30, 170–177. https://doi.org/10.1117/12.55783

Rodriguez-feo Bermudez, E., 2019. Light Propagation Through a Turbulent Cloud: Comparison of Measured and Computed Extinction (Open Access Master's Thesis). Michigan Technological University.

Roggemann, M.C., Welsh, B.M., 1996. Imaging through turbulence. CRC Press, Boca Raton, FL.

Sadot, D., Kopeika, N.S., 1993. Imaging through the atmosphere: practical instrumentation-based theory and verification of aerosol modulation transfer function. J. Opt. Soc. Am. A 10, 172. https://doi.org/10.1364/JOSAA.10.000172

Sadot, Dan, Kopeika, N.S., 1993. Aerosol scattering and absorption modulation transfer function, in: SPIE Proc. pp. 102–118. https://doi.org/10.1117/12.150986

Salby, M.L., 2012. Physics of the atmosphere and climate, 2nd ed. ed. Cambridge University Press, Cambridge; New York.

Saw, E.-W., Shaw, R.A., Salazar, J.P.L.C., Collins, L.R., 2012. Spatial clustering of polydisperse inertial particles in turbulence: II. Comparing simulation with experiment. New J. Phys. 14, 105031. https://doi.org/10.1088/1367-2630/14/10/105031

Seeber, B., 1998. Handbook of applied superconductivity. Institute of Physics Pub., Bristol.

Shaw, R.A., 2003. Particle-turbulence interactions in atmospheric clouds. Annu. Rev. Fluid Mech. 35, 183–227. https://doi.org/10.1146/annurev.fluid.35.101101.161125

Shaw, R.A., Kostinski, A.B., Lanterman, D.D., 2002a. Super-exponential extinction of radiation in a negatively correlated random medium. J. Quant. Spectrosc. Radiat. Transf. 75, 13–20. https://doi.org/10.1016/S0022-4073(01)00287-4

Shaw, R.A., Kostinski, A.B., Larsen, M.L., 2002b. Towards quantifying droplet clustering in clouds. Q. J. R. Meteorol. Soc. 128, 1043–1057. https://doi.org/10.1256/003590002320373193

Shettle, E.P., Fenn, R.W., 1979. Models for the aerosols of the lower atmosphere and the effects of humidity variations on their optical properties (No. AFGL-TR-79-0214).

Shin Hong, Sreenivashiah, I., Ishimaru, A., 1977. Plane wave pulse propagation through random media. IEEE Trans. Antennas Propag. 25, 822–828. https://doi.org/10.1109/TAP.1977.1141689

Shirkey, R.C., Tofsted, D.H., 2006. High Resolution Electro-Optical Aerosol Phase Function Database PFNDAT2006 (U.S. Army Research Laboratory No. ARL-TR-3877). White Sands Missile Range.

Sobol', I.M., Chicago Univ, Il, Department of Mathematics, 1974. The Monte Carlo Method. Popular Lectures in Mathematics. The University of Chicago Press.

Thomas, G.E., Stamnes, K., 1996. Radiative Transfer in the Atmosphere and Ocean. Cambridge University Press, Cambridge; New York.

Thomas, S., Ovchinnikov, M., Yang, F., Voort, D. van der, Cantrell, W., Krueger, S.K., Shaw, R.A., 2019. Scaling of an Atmospheric Model to Simulate Turbulence and Cloud Microphysics in the Pi Chamber. J. Adv. Model. Earth Syst. 11, 1981–1994. https://doi.org/10.1029/2019MS001670

Thomson, L.W., Krider, E.P., 1982. The Effects of Clouds on the Light Produced by Lightning. J. Atmospheric Sci. 39, 2051–2065. https://doi.org/10.1175/1520-0469(1982)039<2051:TEOCOT>2.0.CO;2

Tzannes, A.P., Mooney, J.M., 1995. Measurement of the modulation transfer function of infrared cameras. Opt. Eng. 34, 1808–1817. https://doi.org/10.1117/12.203133

van de Hulst, H.C., 1981. Light scattering by small particles. Dover Publications, New York.

Volnistova, L.P., Drofa, A.S., 1986. Quality of image transmission through light-scattering materials. Opt Spectrosc USSR 61, 76–96.

Warhaft, Z., 2000. Passive Scalars in Turbulent Flows. Annu. Rev. Fluid Mech. 32, 203–240. https://doi.org/10.1146/annurev.fluid.32.1.203

Williams, C.S., Becklund, O.A., 2010. Introduction to the optical transfer function. New Age International, New Delhi.

Wyatt, C.L., 1991. Electro-optical system design for information processing. McGraw-Hill, New York.

Wyngaard, J.C., 2010a. Turbulence in the Atmosphere. Cambridge University Press, Cambridge, UK; New York.

Wyngaard, J.C., 2010b. Turbulence in the Atmosphere. Cambridge University Press, Cambridge, UK; New York.

Wyngaard, J.C., 1992. Atmospheric Turbulence. Annu. Rev. Fluid Mech. 24, 205–234. https://doi.org/10.1146/annurev.fl.24.010192.001225

Yuan, R., Sun, J., Luo, T., Wu, X., Wang, C., Fu, Y., 2014. Simulation study on light propagation in an anisotropic turbulence field of entrainment zone. Opt. Express 22, 13427–13437. https://doi.org/10.1364/OE.22.013427

Zardecki, A., Gerstl, S. a. W., Tam, W.G., Embury, J.F., 1986. Image-quality degradation in a turbid medium under partially coherent illumination. JOSA A 3, 393–400. https://doi.org/10.1364/JOSAA.3.000393

Zardecki, A., Gerstl, S.A.W., Embury, J.F., 1984. Multiple scattering effects in spatial frequency filtering. Appl. Opt. 23, 4124–4131. https://doi.org/10.1364/AO.23.004124

Zege, E.P., Kokhanovsky, A.A., 1994. Analytical solution to the optical transfer function of a scattering medium with large particles. Appl. Opt. 33, 6547–6554. https://doi.org/10.1364/AO.33.006547

Zoller, C.J., Hohmann, A., Foschum, F., Geiger, S., Geiger, M., Ertl, T.P., Kienle, A., 2018. Parallelized Monte Carlo software to efficiently simulate the light propagation in arbitrarily shaped objects and aligned scattering media. J. Biomed. Opt. 23, 1–12. https://doi.org/10.1117/1.JBO.23.6.065004

A Copyright documentation

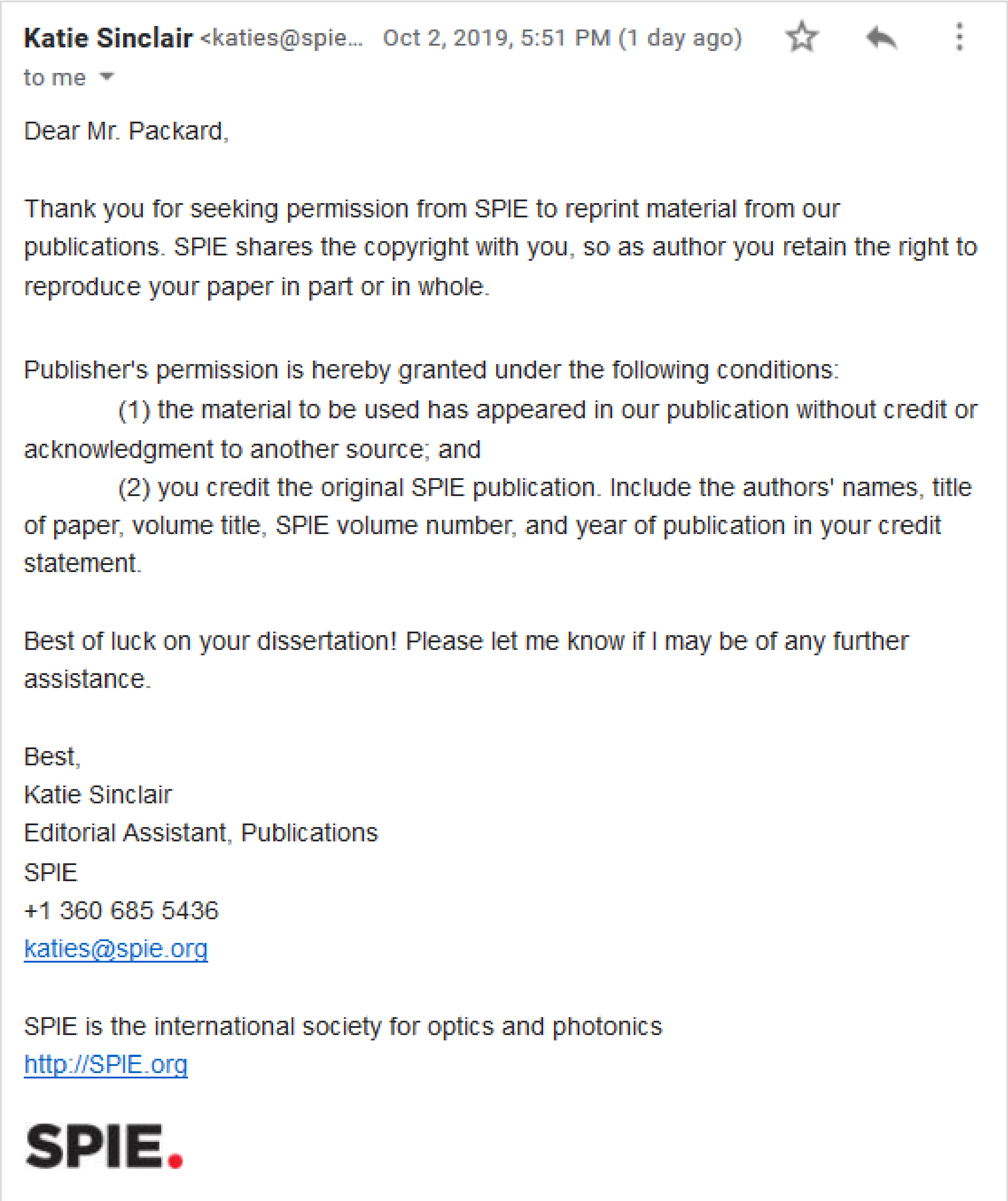

Katie Sinclair <katies@spie... Oct 2, 2019, 5:51 PM (1 day ago)

to me

Dear Mr. Packard,

Thank you for seeking permission from SPIE to reprint material from our publications. SPIE shares the copyright with you, so as author you retain the right to reproduce your paper in part or in whole.

Publisher's permission is hereby granted under the following conditions:

(1) the material to be used has appeared in our publication without credit or acknowledgment to another source; and

(2) you credit the original SPIE publication. Include the authors' names, title of paper, volume title, SPIE volume number, and year of publication in your credit statement.

Best of luck on your dissertation! Please let me know if I may be of any further assistance.

Best,
Katie Sinclair
Editorial Assistant, Publications
SPIE
+1 360 685 5436
katies@spie.org

SPIE is the international society for optics and photonics
http://SPIE.org

SPIE.

Figure A.1. Permission to use article published in the Journal of Applied Remote Sensing.

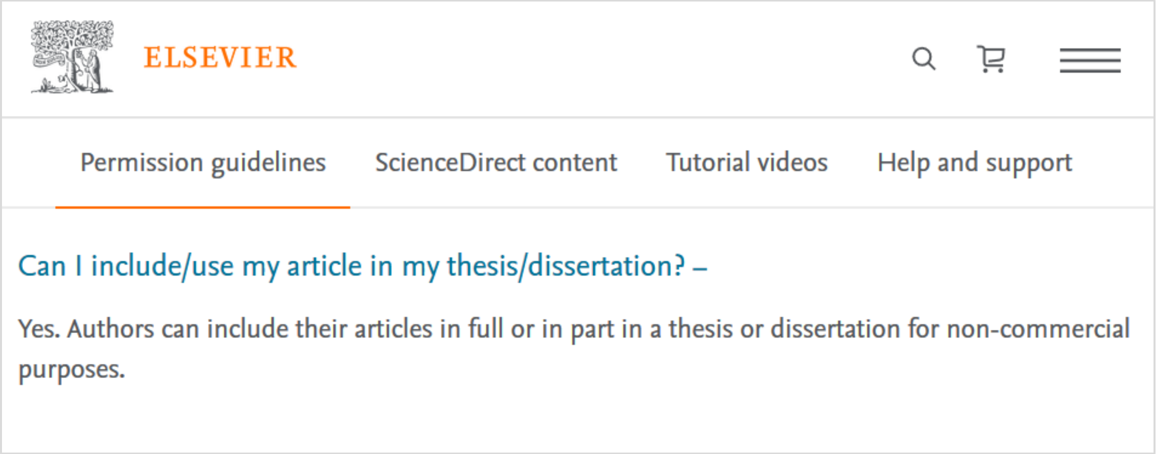

Can I include/use my article in my thesis/dissertation? –

Yes. Authors can include their articles in full or in part in a thesis or dissertation for non-commercial purposes.

Figure A.2. Permission to use article published in the Journal of Quantitative Spectroscopy and Radiative Transfer.